Universidade de Aveiro
2022

João Lucas Lessa Gomes

O Impacto dos Efeitos da Memória de Longo Termo na Linearizabilidade de Amplificadores de Potência baseados em AlGaN/GaN HEMT

The Impact of Long-Term Memory Effects on the Linearizability of AlGaN/GaN HEMT-based Power Amplifiers

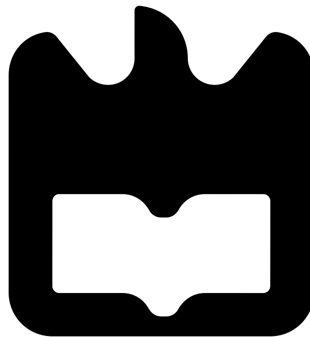

Universidade de Aveiro
2022

João Lucas
Lessa Gomes

O Impacto dos Efeitos da Memória de Longo Termo na Linearizabilidade de Amplificadores de Potência baseados em AlGaN/GaN HEMT

The Impact of Long-Term Memory Effects on the Linearizability of AlGaN/GaN HEMT-based Power Amplifiers

Tese apresentada à Universidade de Aveiro para o cumprimento dos requisitos necessários à obtenção do grau de Doutor em Engenharia Electrotécnica, realizada sob a orientação científica do Professor Doutor José Carlos Esteves Duarte Pedro, Professor Catedrático do Departamento de Electrónica, Telecomunicações e Informática e coorientação do Doutor Luís Carlos Cótimos Nunes, Investigador no Instituto de Telecomunicações, e do Professor Doutor Nikolai Andreevitch Sobolev, Professor Associado do Departamento de Física da Universidade de Aveiro.

Este trabalho foi financiado pela Fundação para a Ciência e a Tecnologia (FCT) e pelo Ministério da Educação e Ciência (MEC) pela bolsa de doutoramento com a referência SFRH/BD/135839/2018 atribuída pela Fundação para a Ciência e a Tecnologia (FCT) através do orçamento de estado e pela União europeia através do Fundo Social europeu (FSE) segundo o Programa Operacional Regional do Centro.

REPÚBLICA PORTUGUESA

CIÊNCIA, TECNOLOGIA E ENSINO SUPERIOR

FCT Fundação para a Ciência e a Tecnologia

CENTRO 2020

o júri / the jury

presidente / president	**Doutor Nelson Fernando Pacheco da Rocha** Professor Catedrático da Universidade de Aveiro
vogais / examiners committee	**Doutora Teresa María Martín-Guerrero** Professora Catedrática da Universidad de Málaga
	Doutor Mattias Thorsell Professor Auxiliar da Chalmers University of Technology
	Doutor Nuno Miguel Gonçalves Borges de Carvalho Professor Catedrático da Universidade de Aveiro
	Doutora Joana Catarina Martins Mendes Investigadora do Instituto de Telecomunicações de Aveiro
	Doutor José Carlos Esteves Duarte Pedro (Orientador) Professor Catedrático da Universidade de Aveiro

agradecimentos / acknowledgements

If this work is of any value then it was because of the invigorating diligence and dedication of my supervisors, Professor José Carlos Pedro and Doctor Luís Cótimos Nunes.

palavras-chave Amplificador, Defeitos de níveis profundos, GaN, HEMT, Linearizabilidade, Modelação

resumo AlGaN/GaN HEMTs estão entre as opções preferidas para amplificação de potência de radiofrequência em transmissores de estação base celular e aplicações de radar. No entanto, apesar de sua perspectiva promissora, a influência dos efeitos de defeitos com níveis profundos torna-os imunes aos esquemas convencionais de pré-distorção digital. Assim, esta tese de doutoramento visa desenvolver uma ligação significativa entre a física do dispositivo e a linearização de amplifificadores de potência baseados em AlGaN/GaN HEMTs. Por forma a preencher esta lacuna, esta tese começa com uma explicação clara dos mecanismos que governam a fonte dominante de efeitos de defeitos com níveis profundos em AlGaN/GaN HEMTs standard, especificamente defeitos no buffer. Com base neste conhecimento, são aprentadas as falhas dos modelos físicos mais conhecidos de defeitos de nível profundo usados para representar estes dispositivos, assim como uma possível melhoria suportada em simulações de TCAD. Isto é também corroborado por uma nova técnica de duplo-pulso capaz de descrever experimentalmente os transientes de captura e emissão num amplo intervalo temporal sob condições isotérmicas. Os transientes de captura medidos validam a nossa compreensão do processo, enquanto que a dependência da temperatura nos perfis de emissão confirmou os defeitos no buffer como a fonte dominante de efeitos de defeitos com níveis profundos. Por fim, através de simulações e resultados experimentais, elabora-se aqui a relação entre a constante de tempo de emissão e a linearizabilidade dos amplificadores baseados em AlGaN/GaN HEMT, mostrando que o pior cenário acontece quando a constante de tempo de emissão é da mesma ordem do tempo entre picos consecutivos da envolvente acima de um certo limiar de amplitude. Este é o caso para o qual se observa uma histerese mais pronunciada nas características de ganho e fase e, consequentemente, um impacto mais forte dos efeitos de memória. O resultado principal desta tese sugere que a maior preocupação na linearização de amplificadores baseados em AlGaN/GaN HEMTs standard está nas grandes constantes de tempo de emissão dos defeitos no buffer.

keywords Amplifier, Deep-level traps, GaN, HEMT, Linearizability, Modeling

abstract AlGaN/GaN High Electron Mobility Transistor (HEMT)s are among the preferred options for radio-frequency power amplification in cellular base station transmitters and radar applications. However, despite their promising outlook, the pervasiveness of trapping effects makes them resilient to conventional digital predistortion schemes, which not only decrease their current range of applications but could also preclude their integration in future small cells and multiple-input multiple-output architectures where simpler predistortion schemes are mandatory. So, this PhD thesis aims at developing a meaningful link between the device physics and the linearizability of the AlGaN/GaN HEMT-based Power Amplifier (PA). In order to bridge this gap, this thesis begins with a clear explanation for the mechanisms governing the dominant source of trapping effects in standard AlGaN/GaN HEMTs, namely buffer traps. Based on this knowledge, we explain why the best known physically-supported trapping models, used to represent these devices, are insufficient and present a possible improvement to what we consider to be the most accurate model, supported by Technology Computer-Aided Design (TCAD) simulations. This has also been corroborated through a novel double-pulse technique able to describe experimentally both the capture and emission transients in a wide temporal span under guaranteed isothermal conditions. The measured stretched capture transients validated our understanding of the process while the temperature dependence of the emission profiles confirmed buffer traps as the dominant source of trapping effects. Finally, through both simulations and experimental results, we elaborate here the relationship between the emission time constant and the achievable linearity of GaN HEMT-based PAs, showing that the worst-case scenario happens when the emission time constant is on the order of the time between consecutive envelope peaks above a certain amplitude threshold. This is the case in which we observed a more pronounced hysteresis on the gain and phase-shift characteristics, and so, a stronger impact of the memory effects. The main outcome of this thesis suggests that the biggest linearizability concern in standard AlGaN/GaN HEMT-based PAs lies on the large emission time constants of buffer traps.

Contents

Contents i

List of Figures iii

List of Tables vii

List of Acronyms ix

1 Introduction 1
1.1 Background and Motivation . . . 1
1.2 Problem Statement and Objectives . . . 4
1.3 Main Contributions . . . 5
1.4 Scientific Publications . . . 6
1.4.1 Journal Papers . . . 6
1.4.2 Conference Papers . . . 7
1.5 Outline . . . 7

2 The AlGaN/GaN HEMT 9
2.1 The Birth of the HEMT . . . 9
2.2 The 2DEG Formation . . . 10
2.3 Considerations on the HEMT Structure . . . 10
2.4 An HEMT's TCAD Template . . . 14
2.4.1 Buffer Traps . . . 14
2.4.2 Lateral Buffer Leakage . . . 15

3 Modeling Buffer Traps 21
3.1 Shockley-Read-Hall Model . . . 22
3.1.1 Additional Considerations on the Trap Mechanisms . . . 24
3.2 The Equivalent-Circuit Model of Buffer Traps . . . 25
3.2.1 Kunihiro and Ohno Model . . . 25
3.2.2 Rathmell and Parker Model . . . 26
3.2.3 Update on the Rathmell and Parker Model . . . 28

4 Drain-Lag Characterization 29
4.1 The Double Pulse Technique for Transient Analysis . . . 30
4.1.1 Deembedding the Static Nonlinearity . . . 32
4.1.2 The Double Pulse Technique as an I-DLTS Tool . . . 34

5 Impact of Deep-Level Traps on the Linearizability 37
5.1 Long-Term Memory in DPD Linearizability - Thermal and Trapping Effects . 39
5.1.1 Trapping Time Constants Impact on PA Linearizability 39
5.1.2 Thermal Time Constants Impact on PA Linearizability 43
5.2 Trapping and Thermal-Dependent Long-Term Memory Effects 45
5.2.1 Device Characterization 45
5.2.2 Impact on Linearizability 47
Other Signal Types 48
5.3 Validation 50

6 Conclusions and Future Work 57

Bibliography 61

List of Figures

1.1 Survey of published PAs from 2000 to 2021, extracted from [32]. (a) Power added efficiency and (b) saturated output power versus frequency of operation for the leading transistor technologies. The grey dashed line represents the 6 GHz. 4

2.1 TCAD simulations of the (a) band diagram of an AlGaN/GaN heterostructure for various AlGaN thicknesses and respective (b) free electron concentration in the AlGaN/GaN interface, for a surface state at 1.5 eV below the conduction band minimum. 11

2.2 (a) Conventional cross-section of an AlGaN/GaN based HEMT structure (not at scale) and (b) corresponding depiction of the band diagram and sheet charge concentrations. 12

2.3 Schematic cross-section of the simulated AlGaN/GaN HEMT TCAD template (not to scale). The width of the device was set to 1 mm. 14

2.4 Simulated IV characteristics of an AlGaN/GaN HEMT (a - b) with and (c - d) without buffer traps. The traps were placed solely on the buffer region with a single energy level 0.5 eV below the conduction band minimum (as typically extracted in Fe-doped buffer layer) with a density of 5×10^{17} cm^{-3} uniformly distributed. 15

2.5 Simulated drain-lag effect: (a) applied v_{GS} and v_{DS} and corresponding i_{DS}; (b) zoom-out of the previous profiles to highlight the slower recovery transient. 16

2.6 Simulated cross-section of the HEMT in different time frames, all when $v_{DS} = 70\tilde{V}$, i.e. when the capture process dominates. The horizontal and vertical axis correspond to x and y directions, respectively, with the drain terminal on the right hand side and the substrate on the top part of the plot. The vertical dashed white lines are the gate limits. Yellowish colors represent a higher concentration of (a) trapped electrons and (b) free electrons. 18

2.7 Simulated conduction band minimum (solid line) and quasi-Fermi potential (dashed line) profiles, obtained from a vertical cutline aligned with the drain side of the gate-edge, (a) right before (blue - represents the initial quiescent state) and immediately after the rise of v_{DS} (orange); (b) at the initial quiescent state (blue) and after 1 μs with $v_{DS} = 50$ V (orange); (c) at the initial quiescent state (blue) and immediately after pulsing down v_{DS} back to 5 V (orange). The vertical dash line, in the previous 3 plots, represents the AlGaN/GaN interface. From (d-f), we compare the same time frames as above, using the same color code, but now showing the free (solid line) and trapped (dashed line) electron concentration vertical profiles. 19
2.8 Simulated (a) total number of free electrons in the buffer and channel layers, and ionized trap centers in the buffer over time. (b) Spatial average of the conduction band minimum in the buffer layer (left axis) and sum of the all negative charge in the buffer layer (right axis). 20

3.1 Pulsed IV curves of a GaN HEMT for various drain quiescent voltages. 21
3.2 Schematic representation of the 4 basic processes involved in the SRH model for a single energy level. (a) Electron capture; (b) electron emission; (c) hole capture; (d) hole emission. Adapted from [106]. 22
3.3 Isothermal recovery transients measured, at $(v_{DS}, v_{GS} = (5, -1)$ V for various initial drain quiescent voltages and $V_{GSQ} = -5$ V, from two similar AlGaN/GaN HEMTs both with a Fe-doped buffer layer. 25
3.4 (a) Geometrical interpretation of the equivalent-circuit model and respective (b) equivalent-circuit model for the drain-lag effect conceived by Kunihiro and Ohno [122]. 26
3.5 Equivalent-circuit model of deep-level traps conceived by Rathmell and Parker [123]. 27
3.6 Simulated pulsed response on the TCAD template for an input v_{DS} signal and the corresponding percentage of trap centers that are ionized in the entire buffer over time, when (a) v_{DS} steps up to 70 V and (b) after when it steps down to 10 V respectively. The three profiles correspond to the data directly extracted from the TCAD simulations and the best fit obtained from the original and the improved Rathmell and Parker model. Note that v_{trap}/V_0 is the exactly the same as the percentage of ionized trap centers. 28

4.1 Measurement setup. A: dc Power Supplies; B: Tektronix DPO3052 500 MHz, 2-Ch Digital Phosphor Oscilloscope; C: AWG5012C Arbitrary Waveform Generator; E: Drain Pulser; F: Gate Pulser; G: TCP0030A Current Probe; H: CGH27015 GaN HEMT from Cree and test fixture; I: 11612A OPT 001 RF Keysight Bias Tee. 30
4.2 Test signals used to extract the (a) capture and the (b) emission dynamics. Note that in (a) everything is kept constant except the pre-pulse voltage amplitude, V_{Pre}, and its width, P_W. For the emission analysis, the pre-pulse width is kept constant and it is now the time between the pre-pulse end and the current measurement, T_{BP} that is varied. The horizontal dashline represents the threshold voltage. The vertical dashline represents the time instance where the drain current is measured. 31

4.3 Measured profiles of two different AlGaN/GaN HEMTs for various pre-pulse amplitudes, V_{Pre}. (a) and (c) sweep of the pre-pulse width, P_W; (b) and (d) sweep of the time between the pre-pulse end and the measurement pulse, T_{BP}. 32
4.4 (a) Capture and (b) emission current transients measured at different temperatures with $V_{Pre} = 90$ V and measured at $V_{DSP} = 28$ V. (c) and (d) correspond to the trapping state after an numerical inversion using (4.2). 35
4.5 Arrhenius plots drawn from the results of Fig. 4.4(d) for two different measurement biases. Note that the trap's cross-section should be extracted from the y-intercept however there is a bias dependence that remains to be addressed. 36

5.1 Hysteretic (a) AM/AM and (b) AM/PM characteristics of a GaN HEMT-based PA subjected to a 4-carriers GSM modulated signal. ACC stands for analog [long-term memory] compensation circuit. 38
5.2 (a) Simulated CW gain, efficiency, and AM/PM response of the designed PA. Each curve corresponds to a different center frequency from 2.4 GHz to 2.6 GHz with a 50 MHz step; (b) the simulated load-line at the current source plane, with the bias point $[I_{DS}, V_{DS}, V_{GS}] = [100\,\text{mA}, 50\,\text{V}, -2.7\,\text{V}]$, and for the center frequency (2.5 GHZ) on top of the pulsed I-V curves (for $V_{DQ} = 90$V); and (c) the impedance profile over frequency with the fundamental and harmonic impedances of the center frequency (2.5 GHz) marked. 40
5.3 Equivalent circuits that represent the dynamics associated with (a) trapping effects and (b) electrothermal effects, and their respective main impact on the transistor performance. ΔV_{th} and $\Delta\beta$ stand, respectively, for a shift of the threshold voltage [46, 127] and transistor's current gain [140]. The squares crossed by a broken line, represent a nonlinear mapping between the physical variables (the trap control voltage and the temperature) and the dc-IV model parameters in our formulation, $i_{DS} = f(v_{GS}, v_{DS}, v_{trap}, T)$. 41
5.4 Simulated (a) PA response under a two-tone excitation (for 200 kHz of frequency separation, Δf), considering a fixed capture time constant, τ_c, equal to 0.1 μs and different emission time constants, τ_e, and (b) the respective trapping control voltages on top of the two-tone envelope signal. No thermal effects were considered. 42
5.5 Simulated (a) PA response for a LTE signal with 2 MHz bandwidth and (b) the respective signal and trapping control voltage response when different trapping emission time constants are considered. The inset in (b) is a simple magnification of the peaks in the final portion of the signal. 42
5.6 Simulated ACPR levels before (dashed lines) and after (solid lines) DPD versus the trapping emission time constants for two different signal bandwidths. . . 43
5.7 (a) Example of a 2 MHz LTE signal with all peaks above 50% of the maximum signal amplitude highlighted and (b) the histogram of the time between peaks for different realizations of this signal type. 44
5.8 Simulated (a) PA response under a two-tone excitation (for 200 kHz of frequency separation, Δf), considering different thermal time constants and, (b), the respective normalized temperature variation on top of the normalized instantaneous power dissipation. No trapping effects were considered. 44
5.9 Simulated ACPR levels before (dashed lines) and after (solid lines) DPD versus the thermal time constants for two different signal bandwidths. 45

5.10 Measured drain current recovery from a pre-pulse of 90V to 50V for several different temperatures. 46
5.11 (a) Arrhenius plots drawn from the results of Fig. 5.10 and (b) the resulting emission time constant versus temperature. 46
5.12 Simulated temperature variation of the device's junction, package and case over time, when a constant power dissipation equal to 57 W is considered, and for a room temperature of 46°C. The solid lines are from a Multiphysics simulation and the dashed lines are the response of the extracted multi-RC network. . . 47
5.13 Simulated (a) junction temperature variation, (b) trapping control voltage variation and (c) the respective trapping emission time constant affected by the temperature variation. 49
5.14 Simulated (a) slotted signal and junction temperature variation, (b) trapping emission time constant affected by the temperature variation and (c) trapping control voltage variation. 50
5.15 100W GaN HEMT-based PA centered at 2 GHz. 51
5.16 (a) Simulated CW gain, efficiency, and AM/PM response of the designed PA. Each curve corresponds to a different center frequency from 1.95 GHz to 2.05 GHz with a 20 MHz step; (b) the simulated load-line at the current source plane, with the bias point $[I_{DS}, V_{DS}, V_{GS}] = [100\,\text{mA}, 50\,\text{V}, -2.7\,\text{V}]$, and for the center frequency (2 GHZ) on top of the pulsed IV curves (for $V_{DQ} = 90\text{V}$); and (c) the impedance profile over frequency with the fundamental and harmonic impedances of the center frequency (2 GHz) marked. 52
5.17 Diagram of the setup used to performed the measurements in this section. . . 53
5.18 Measured DPD residuals and the respective simulated trapping response considering the emission time constant varying accordingly to the Arrhenius plot linearization and the simulated device temperature. 53
5.19 Measured ACPR values for different DPD adaptation iterations, considering the 2 MHz LTE signal. 54
5.20 Measured spectrum of the reference signal and the output signal before (dashed lines) and after (solid lines) the DPD correction for both devices considering the 2 MHz LTE signal. 54
5.21 Measured (a) ACPR and (c) NMSE and simulated (b) ACPR and (d) NMSE levels after DPD versus signal bandwidth in both devices for LTE-type signals with two different PAPR levels. 55

List of Tables

5.1 Comparison of the Linearizability in Different Conditions 48

List of Acronyms

2DEG Two-Dimensional Electron Gas

4G Fourth-Generation

5G Fifth-Generation

ACPR Adjacent Channel Power Ratio

AlGaAs Aluminium Gallium Arsenide

AlGaN Aluminium Gallium Nitride

AlN Aluminium Nitride

C-DLTS Capacitance Deep-Level Transient Spectroscopy

CW Continuous Wave

DIBL Drain Induced Barrier Lowering

DLTS Deep-Level Transient Spectroscopy

DPD Digital Predistortion

FDD Frequency Division Multiplexing

FET Field-Effect Transistor

GaAs Gallium Arsenide

GaN Gallium Nitride

GSM Global System for Mobile Communications

GMP Generalized Memory Polynomial

HEMT High Electron Mobility Transistor

I-DLTS Current Deep-Level Transient Spectroscopy

IIR Infinite Impulse Response

InGaN Indium Gallium Nitride

ISBW Instantaneous Signal Bandwidth

LTE Long-Term Evolution

MP Memory Polynomial

MIMO Multiple-Input Multiple-Output

MIS Metal Insulator Semiconductor

MOCVD Metalorganic Vapour-Phase Epitaxy

PA Power Amplifier

PAPR Peak-to-Average Power Ratio

RF Radio-Frequency Power Amplifier

RFPA Radio-Frequency

SiC Silicon Carbide

Si_3N_4 Silicon Nitride

Si-LDMOS Silicon-Laterally Diffused Metal Oxide Semiconductor

SRH Shockley-Read-Hall

TCAD Technology Computer-Aided Design

TDD Time Division Multiplexing

Chapter 1

Introduction

1.1 Background and Motivation

Cellular mobile communications have been steadily evolving towards faster data rates, higher user density, lower latency, and ultra-reliable communications. Simultaneously, the available wireless spectrum has been getting scarcer and more expensive, so the constraints have inevitably kept growing. The adoption of wider bandwidths pushed the carrier signal to higher frequencies. The elimination of guard bands in the spectrum allocation and the pursuit for lower bit-error rates reinforced the demand for linearity in wireless circuitry. The transition to higher-order amplitude modulation methods and the use of multi-carrier aggregation to improve the spectral efficiency resulted in signals with higher Peak-to-Average Power Ratio (PAPR), setting additional limitations to the transmitters' power efficiency [1–4]. In a nutshell, bandwidth, linearity, and efficiency are key performance metrics in today's transmitter design. They are also three competing goals amongst themselves which makes their joint optimization a highly complex task.

The large PAPR in modern signals, for instance, is hugely detrimental to the wireless transmitters' efficiency because of how it impacts the Radio-Frequency Power Amplifier (RF) PA. Generally, the efficiency is highest when the PA is driven closer to its maximum power capabilities. However, with large PAPR signals, the PA operates at back-off most of the time, where its efficiency is normally lower. Increasing the signal's average power could ameliorate this issue, but not without inflicting some compression to the PA gain response. That is why the PA optimization towards higher efficiency is usually done at the expense of linearity [1].

Conventionally, the PA efficiency tends to be favored, even if that implies adding some distortion to the signal. PA power consumption can surpass 50% of the total available power in modern macro base stations [5–7], more than any other element. This is further aggravated by the necessity of cooling systems to dissipate the generated heat from wasted power [8]. Efficient PAs are therefore of paramount importance, both from a cost and an environmental point of view. So, to circumvent the impact of large PAPR signals, several PA architectures have been developed to ensure a reasonable degree of efficiency even at back-off. Doherty PAs, Envelop Tracking PAs, Load-Modulated Balanced Amplifiers and Outphasing PAs are among the most popular ones [9–12].

Despite the progress achieved by these topologies, they are still unable to guarantee the linearity requirements for wireless communications, and so additional compensation is still required [13, 14]. Several techniques have been proposed over the years, like feedback and

feedforward linearization, but Digital Predistortion (DPD) ended up conquering the market as the most cost-effective solution [3, 15]. DPD is essentially an attempt to compute the pre-inverse of the PA and then use it to distort the input signal in such a way that when this gets amplified, the nonlinearities of the PA will distort the signal to yield, in the end, linear amplification [3, 8]. Naturally, the more complex DPD schemes become, the better is the accuracy of their estimation of the PA pre-inverse. Unfortunately, this is mostly done at the cost of increasing the number of coefficients, requiring more memory storage and processing capability, which increases the power consumption, the computational time and, ultimately, the integration cost in a base station, beyond limiting the signal bandwidth [16].

The concern for simpler DPD schemes has become even more compelling with the transition from Fourth-Generation (4G) standards to Fifth-Generation (5G) new radio. Among the many expected technological updates, some will have profound consequences to the transmitter infrastructure. For instance, that is the case of the exploitation of new spectra - sub-6-GHz and Ka-band [17, 18]; the densification of small base stations; and the deployment of massive Multiple-Input Multiple-Output (MIMO) antenna arrays and digital beamforming technologies [16, 19]. These expected changes will force us to rethink conventional DPD schemes, as larger bandwidths impose enormous demands on the sampling rate of the digital-to-analog and analog-to-digital converters, plus the DPD algorithm. Mutual coupling and cross-antenna interactions will substantially increase the linearization complexity. Beyond that, while the power consumption of each individual PA in a MIMO transmitter is expected to decrease, the power baseline of each DPD scheme is not. All things considered, low-complexity and low-power linearization alternatives are expected to play a key role in 5G infrastructure [16, 20].

Much like linearization techniques are expected to lower their complexity and power consumption to meet the forthcoming cellular market, PAs should also get easier to linearize. Indeed, for the same DPD processing capability, some PA technologies achieve higher degrees of linearity than others (what can be called as a DPD friendliness [21] or a PA with better linearizability [22]). In fact, this is already a current concern for PA manufactures, as they may not know *a priori* what commercially available DPD is being implemented in a base station. Thus, not only are modern PAs designed for higher efficiency, but also to meet some linearizability criterium, so that simple standard linearization techniques are enough to achieve the desired linearity metrics.

Nonlinear memory effects are hugely detrimental to the PAs' linearizability as they hinder the correct compensation of the PA characteristic, resulting in leftover in-band and out-of-band distortions. Depending on their temporal span, relative to the envelope dynamics, some are more easily compensated by conventional predistortion techniques than others. From the envelope time scale perspective, memory effects can be divided into two main groups: short- and long-term memory effects [23]. Careful design of the PA bias and matching networks can help reduce short-term memory effects [24–26], so that they become possible to compensate using DPD models like the Generalized Memory Polynomial (GMP) [15]. Long-term memory is significantly more difficult to mitigate at the design level and so much of its compensation relies on intricate DPD schemes.

To understand why, consider a very simplistic model to represent the PA envelop response, $y(n)$, as a product of a simple memory polynomial expansion with the system's input, $x(n)$, as in

$$y(n) = \left[\sum_{p=0}^{P} \sum_{m=0}^{M} h_p(m) |x(n-m)^p| \right] x(n) \tag{1.1}$$

where $h_p(m)$ are complex entities that represent the observed envelop amplitude ($|x(n)|$) dependent amplitude (the so called AM-to-AM distortion) and phase-shift (usually known as the AM-to-PM distortion) and m constitutes the amount of memory taps. Because the DPD scheme must approximate the inverse of the PA dynamic gain characteristics, it could still be described by a polynomial expansion just like the one of (1.1). On one hand, (1.1) must be able to account for the bias networks-induced memory effects, caused by the dynamic fluctuations of bias voltages whenever the dc current drawn from the power supply faces a reactance in the bias lines. Unless, the bias, the input or the output matching networks present very sharp resonances (which correspond to slow variations in time), these are responsible for memory effects whose time constants are on the order of, or faster than, the envelope dynamics [23]. Nowadays, we typically see envelop bandwidths on the order of tens of MHz, which means hundred nanosecond-long sampling periods. The memory taps, m, must then account for time spans also on this order. On the other hand, long-term memory effects arise from a completely different set of phenomena, essentially electro-thermal and trapping effects, whose time constants can be several orders of magnitude longer than the time variations of the information envelop. This implies that a simple DPD scheme, like (1.1), could only simultaneously compensate both short and long-term memory using an unbearably large total amount of memory taps, M.

The advent of 5G will also affect other aspects of the PA design. The pursuit for a wider Instantaneous Signal Bandwidth (ISBW) will, on the one hand, excite more aggressively the memory effects of the PA, strengthening the linearizability requirements, and on the other hand, increase the demand for transistors capable of outputting the necessary power at higher frequencies. While efficiency, linearity, and ISBW are greatly conditioned by the PA topology and linearization scheme, guaranteeing the specified output power and baseline efficiency level at certain operating frequency ranges relies, primarily, on the transistor technology [27].

Figure 1.1 presents an in-depth survey of the saturated output power and power-added efficiency over frequency for the leading technologies in the cellular market for the past 21 years. There, one can see why PAs based on Silicon-Laterally Diffused Metal Oxide Semiconductor (Si-LDMOS) stand relevant for low-frequency applications up to approximately 2.3 GHz [28]. Despite the slightly better performance in output power and efficiency by Gallium Nitride (GaN) HEMT-based PAs, they remain the most cost-effective solution for that range. Up to 6 GHz, however, GaN emerges as the superior choice, achieving consistently the highest levels in several works by a considerable margin. Unsurprisingly, GaN HEMT-based PAs are now among the preferred options for RF power amplification in cellular base station transmitters, power-switching, satellite communications and radar [29, 30]. They are also being appointed as one of the most promising alternatives for sub-6-GHz applications in 5G [16, 31] and some even consider its possible integration in future applications targeting raw power at mm-wave [27].

The success of GaN HEMT-based PAs lies in the transistor's very large breakdown fields, coupled with high electron mobility and saturated velocity while maintaining favorable thermal conductivity [33–35]. The combination of these attributes makes them capable of larger power densities compared to competing technologies, as for instance Si-LDMOS transistors. With increased power densities, the same power level can be achieved with a lower gate periphery, which results in lower input/output capacitances [36] - the bottleneck for high-frequency and high bandwidth operation.

Despite its promising outlook, GaN HEMT-based PAs remain affected by effects like current collapse [37], dynamic on-resistance (or knee-walkout) [38] and dc-RF dispersion [39].

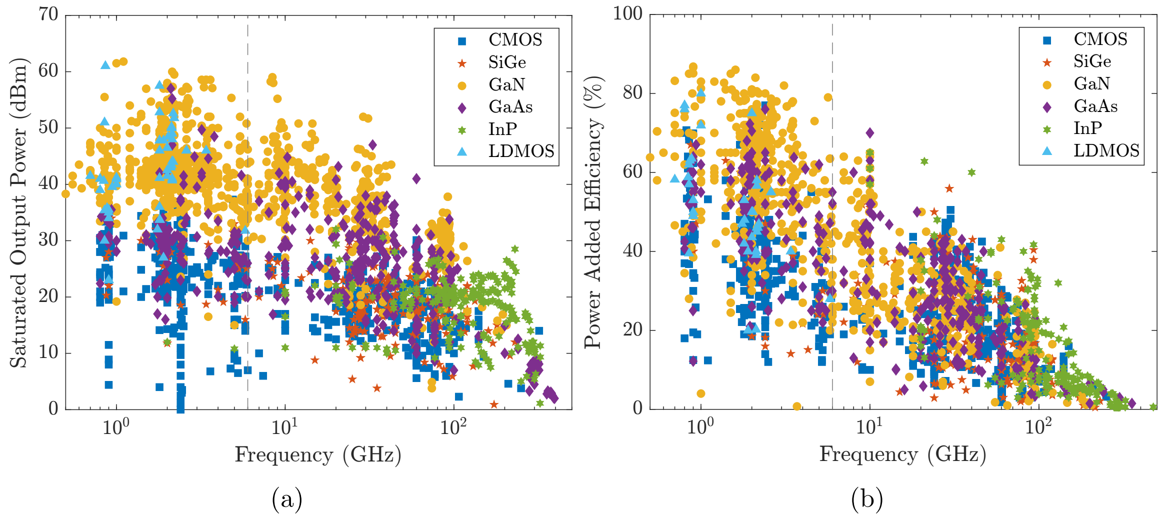

Figure 1.1: Survey of published PAs from 2000 to 2021, extracted from [32]. (a) Power added efficiency and (b) saturated output power versus frequency of operation for the leading transistor technologies. The grey dashed line represents the 6 GHz.

The root of these effects has long been linked to the presence of deep-level traps in the HEMT structure, but their comprehension remains an elusive topic. Throughout the years, they have been ascribed to contaminations during the growth process, dislocations due to lattice mismatch, varying material qualities, doping, surface and interface states [40,41]. Due to their large activation energy, these trap's dynamics can span from a few microseconds up to seconds, being, therefore, a source of long-term memory for the PA [42].

Trapping and electrothermal effects constitute the main reason for long-term memory and, consequently, linearizability concerns. Recent alternatives have managed to overcome this problem by taking advantage of the physical knowledge of the phenomenon at the transistor level and extrapolate it to the system level [42–44]. Unfortunately, these alternatives still rely on very complex schemes or lack validation in more useful PA architectures.

In conclusion, GaN HEMTs are, for the time being, one of the most promising technologies for future high power and high-frequency applications. They are also resilient to conventional DPD schemes, which not only decrease their current range of application but could also preclude their integration in future small cells and MIMO architectures where simpler predistortion is mandatory. Whether or not this present linearizability issue will play a decisive role in the future of GaN HEMT is still unclear. Solving it, nevertheless, will, in all likelihood, bring considerable progress to commercially available GaN-based products. Ultimately, such endeavor may prove useful to improve future DPD schemes and/or help guide certain device characteristics at the manufacture level to attain transistors with higher linearizability.

1.2 Problem Statement and Objectives

In order to address the topic described above, firstly a clear and general relationship between the transistor and the PA characteristics must be identified. Typically, this link is built by abstracting the device behavior to an equivalent circuit model. It is then easier to convey specific aspects of the model parameters, like the transistor transconductance and

capacitance profiles, to the PA performance [36]. Nowadays, equivalent circuit models of well-consolidated technologies can describe the transistor performance up to tens of GHz with very good accuracy. However, the lack of a deeper understanding regarding the mechanisms underlying deep-level traps and their impact on GaN HEMTs has prevented their description with a general and accurate equivalent-circuit model. This affects our ability to establish a meaningful link between the transistor operating mechanisms and the PA performance. The natural approach is then to work at a more conceptual level, trying to come up with hypotheses that explain the measurements and then use more general and accurate models to validate the data. The latter can be achieved by reducing the abstraction level and simulate at a more fundamental level, i.e., a distributed time- and space-dependent model.

Once these insights are properly incorporated into an equivalent circuit model, experimental characterization and validation are essential. Trapping phenomena is again an issue in this regard. For instance, trapping transients are typically quantified by analyzing their impact on the drain to source current, i_{DS}, so, because of power dissipation, what we actually see is often an interplay of trapping and electrothermal effects. Therefore, there is a need for a characterization methodology where these two effects are properly separated.

Based on the present scenario, this work aims to contribute to the development of a meaningful link between the device physics and the linearizability of AlGaN/GaN HEMT-based PAs. For that, both a theoretical and experimental approach are needed to develop our conceptual model and then validate it. To achieve this overall objective, the following targets were defined:

- **Improve our current understanding of the trapping effects affecting AlGaN/GaN HEMTs**

  The success of this target should be defined by the achievement of a conceptual explanation for the most relevant features linked to trapping effects in a conventional AlGaN/GaN HEMT that could be validated both by TCAD simulations and laboratory measurements.

- **Development of dedicated techniques for trapping effects characterization**

  This target focuses on the development of one or more experimental methodologies that allow us to thoroughly characterize trapping effects and discriminate the most relevant traps in a conventional AlGaN/GaN HEMT.

- **Development of a meaningful link between the device physics and the linearizability of AlGaN/GaN HEMT-based PAs**

  The final and most important target of this PhD thesis is to establish a link between the device physics and the linearizability of AlGaN/GaN HEMT-based PAs. This link should provide the necessary insight to predict the worst and best case scenarios both at the device and system level. This includes knowing what are the traps characteristics that compromise the linearizability, as well as the operating conditions, such as signal statistics or DPD schemes, that best suit AlGaN/GaN HEMT-based PAs when the purpose is linearity.

1.3 Main Contributions

The main contributions of this PhD work were the following:

- Development of a novel characterization procedure to extract the trapping dynamics in a wide span of time constants under isothermal conditions [45–47].

- Physical evidence and theoretical explanation for the existence of slow capture transients in GaN HEMTs affected by deep-level traps [45, 46].

- Demonstration and explanation of the long-term memory impact, caused by electrothermal effects, on the achievable linearity (linearizability) of GaN HEMT-based power amplifiers [23, 48, 49].

During the final stage of this PhD thesis, the focus shifted to the more fundamental aspects of the equivalent circuit model, particularly their capacitive elements. The main contributions to this field are listed below, however they will not be further addressed in the remaining document. For further information check the listed papers in the next section.

- Re-interpretation of the FET's equivalent circuit lumped topology as a gross simplification of the more accurate and physically-sustained distributed nonlinear RC network [50, 51].

- Conciliation of the non-reciprocal capacitance formulation in the equivalent circuit model of FETs with the energy conservation principle.

1.4 Scientific Publications

1.4.1 Journal Papers

- B. González et al., "A Simple Method to Extract the Thermal Resistance of GaN HEMTs from De-trapping Characteristics" submitted to the *Electron Device Letters.*

- J. L. Gomes, F. M. Barradas, L. C. Nunes and J. C. Pedro, "Energy Non-Conservation in the FET's Equivalent Circuit Capacitance Model," submitted to the *IEEE Transactions on Microwave Theory and Techniques.*

- [49] J. L. Gomes et al., "The Impact of Long-Term Memory Effects on the Linearizability of GaN HEMT-Based Power Amplifiers," *in IEEE Transactions on Microwave Theory and Techniques*, vol. 70, no. 2, pp. 1377-1390, Feb. 2022.

- [48] P. M. Tomé, F. M. Barradas, L. C. Nunes, J. L. Gomes, T. R. Cunha and J. C. Pedro, "Characterization, Modeling, and Compensation of the Dynamic Self-Biasing Behavior of GaN HEMT-Based Power Amplifiers," *in IEEE Transactions on Microwave Theory and Techniques*, vol. 69, no. 1, pp. 529-540, Jan. 2021.

- [46] J. L. Gomes, L. C. Nunes, C. F. Gonçalves and J. C. Pedro, "An Accurate Characterization of Capture Time Constants in GaN HEMTs," *in IEEE Transactions on Microwave Theory and Techniques*, vol. 67, no. 7, pp. 2465-2474, July 2019.

1.4.2 Conference Papers

- [51] J. L. Gomes, L. C. Nunes and J. C. Pedro, "On the Drain-to-Source Capacitance of Microwave FETs in Triode Region," *in 2022 IEEE/MTT-S International Microwave Symposium*, 2022.
- [50] J. L. Gomes, L. C. Nunes, F. M. Barradas and J. C. Pedro, "A Qualitative Explanation of the AlGaN/GaN HEMT Nonlinear Intrinsic Capacitances," *in 2022 International Workshop on Integrated Nonlinear Microwave and Millimetre-Wave Circuits* , 2022, pp. 1-3.
- [52] J. Pedro, J. Gomes and L. Nunes, "Electro-Thermal and Trapping Characterization of AlGaN/GaN RF Power HEMTs," *in 2021 IEEE BiCMOS and Compound Semiconductor Integrated Circuits and Technology Symposium*, 2021, pp. 1-6.
- [23] J. Pedro et al., "A Review of Memory Effects in AlGaN/GaN HEMT Based RF PAs," *in 2021 IEEE MTT-S International Wireless Symposium*, 2021, pp. 1-3.
- [53] P. M. Tomé, F. M. Barradas, L. C. Nunes, J. L. Gomes, T. R. Cunha and J. C. Pedro, "A Transient Two-Tone RF Method for the Characterization of Electron Trapping Capture and Emission Dynamics in GaN HEMTs," *in 2020 IEEE/MTT-S International Microwave Symposium*, 2020, pp. 428-431.
- [54] J. L. Gomes, L. C. Nunes and J. C. Pedro, "Explaining the Different Time Constants Extracted from Low Frequency Y_{22} and I_{DS}-DLTS on GaN HEMTs," *in 2020 IEEE/MTT-S International Microwave Symposium*, 2020, pp. 432-435.
- [47] J. L. Gomes, L. C. Nunes and J. C. Pedro, "Transient Pulsed S-Parameters for Trapping Characterization," *in 2020 International Workshop on Integrated Nonlinear Microwave and Millimetre-Wave Circuits*, 2020, pp. 1-3.

1.5 Outline

This document is divided into 6 chapters organized as follows

- **Chapter 1** lays out the main motivation behind this project and states the problem. It also provides the objectives and main contributions of this PhD work.
- **Chapter 2** describes the AlGaN/GaN principle of operation, starting from the very basics of the HEMT architecture up to the reason why buffer traps are essential to prevent short channel effects, and concluding with a thorough explanation of how these traps work. This chapter serves as a support for the drain-lag model and experimental characterization in the subsequent chapters.
- **Chapter 3** explains the Shockley-Read-Hall (SRH) model and highlights the two best known equivalent circuit models, supported on the SRH, for describing buffer-induced trapping effects on HEMTs.
- **Chapter 4** presents a novel characterization procedure used to extract the trapping dynamics in a wide temporal span under guaranteed isothermal conditions, which helped further consolidate the knowledge on the trapping mechanisms.

- **Chapter 5** explores the relationship between the detrapping time constant and the achievable linearity of GaN HEMT based PAs, showing that the worst-case scenario happens when the emission time constant is on the order of the time between consecutive envelope peaks above a certain amplitude threshold.

- **Chapter 6** concludes this thesis by giving a framework to the main achievements of this PhD work in the current paradigm of research on GaN HEMTs for Radio-Frequency (RFPA) and provides a possible direction to future work.

Chapter 2

The AlGaN/GaN HEMT

Finding a comprehensive answer to the question of how deep-level traps affect the linearizability of a GaN HEMT-based PA entails different abstraction levels, starting at the device level, passing through the PA up to a more system level where we look to the predistorted PA. At the device level, not only is worth understanding how traps work but also why are they there in the first place.

Based on the literature, some transistors are affected by drain-lag and others by both drain- and gate-lag, some reveal a kink effect, others pronounced knee-walkout, we find multiple time constants, "stretched" time constants, thermally activated traps or temperature invariant traps, among others. The plethora of different macro effects suggests the existence of different trapping sources. Naturally, this thesis is not meant as a survey of all the reported types of traps and their respective behavior, nor do we need to address all of them to: (i) identify the main root for long-term memory in standard AlGaN/GaN HEMTs; (ii) establish a link between the features inherent to most traps and linearizability.

With this in mind, this chapter intends to provide a sufficiently complete picture of the most reported AlGaN/GaN HEMT structure in the literature, and demonstrate how deep-level traps are essential for the HEMT's operation.

2.1 The Birth of the HEMT

In 1978, Dingle *et.al.* presented in their seminal paper [55] the notion of mobility enhancement through modulation doping. They found that a multilayer heterojunction arrangement of Aluminium Gallium Arsenide (AlGaAs) and Gallium Arsenide (GaAs) (AlGaAs - GaAs - AlGaAs - GaAs - ...), whose wide bandgap layers (AlGaAs) are doped, and the others (GaAs) are not, displayed much higher carrier mobility than the case where all layers are equally doped. Because the GaAs conduction band minimum lies lower in energy than the AlGaAs donor states, the electrons from these states will move into the GaAs regions, forming a pseudo Two-Dimensional Electron Gas (2DEG). Most of the mobile carriers (electrons confined in the GaAs) in a modulated-doped superlattice are spatially separated from their ionized parent donors (impurities in the AlGaAs). Electron density in the GaAs channel is then far superior to the local concentration of scattering centers, which reflects on a substantial improvement of the channel mobility.

Shortly after, in 1980, inspired by the work of Dingle, Mimura *et.al.* published the first demonstration of a new Field-Effect Transistor (FET) - the AlGaAs/GaAs HEMT [56]. Es-

sentially, they introduced a rectifying contact on top of Dingle's superlattice to control, by field effect, the 2DEG concentration [57, 58].

Later, following the breakthrough accomplished by Nakamura *et.al.*, growing high quality GaN films on top of a sapphire substrate by Metalorganic Vapour-Phase Epitaxy (MOCVD) became a possibility [59], which quickly prompted, in 1993, the first publication of an AlGaN/GaN HEMT [60]. Even though GaN has an electron's effective mass (≈ 0.22) about three times larger than GaAs, and therefore much lower electron drift mobility, it possesses other features that made it highly desirable [61]. At room temperature, $Al_xGa_{1-x}As$ has a tunable bandgap that spans from 1.4 eV ($x = 0$) to 2.1 eV ($x = 1$) [62], whereas $Al_xGa_{1-x}N$ varies from 3.4 eV ($x = 0$) up to 6.2 eV ($x = 1$). Wider bandgaps translate into higher operating temperatures and breakdown voltages. The ability to then operate at higher drain voltages allows for higher output impedance which lowers the matching losses in a PA. Moreover, GaN is capable of higher peak electron velocity and saturation velocity, which contributes to a higher maximum drain current [61, 63].

AlGaN/GaN HEMTs initial prototypes [60] were based on modulation doping, *i.e.*, a n-type AlGaN followed by an undoped GaN layer. But, as later demonstrated [61, 64], even with an unintentionally doped AlGaN layer, the 2DEG would still reach very high sheet concentrations (up to 10^{13} cm^{-2}). Such peculiar feature precludes the need for intentional doping, which has been linked to a reduction of the pn gate tunnel leakage current at pinch-off, lower 1/f noise and increased electron mobility [65].

2.2 The 2DEG Formation

The 2DEG formation in unintentionally doped AlGaN/GaN heterostructures is understood as a combination of two factors, the polarization of the AlGaN layer and the presence of surface states. Wurtzite $Al_xGa_{1-x}N$ possesses both spontaneous polarization (due to the noncentrosymmetry feature of wurtzite crystals) and piezoelectric polarization (due to the mechanical strain inherent to an heterostructure), that grow with the molar concentration of aluminum [61]. The polarization induced charge (σ) in the AlGaN is therefore larger than in GaN, which means that the net charge at the AlGaN($+\sigma_{AlGaN}$)/GaN($-\sigma_{GaN}$) interface is positive. Electrons are thus more attracted to this site. Since these electrons cannot come from the GaN, otherwise jeopardizing the 2DEG confinement by leaving a positive charge behind, they must then come from the surface. Surface states provide electrons to the local conduction band, which are then swept by the polarization induced field to the channel. This has been corroborated by the existence of a critical AlGaN layer thickness for which no channel is formed below a certain value, defined by the intersection of the Fermi level with the surface level in the bandgap [66], as illustrated in Fig. 2.1.

2.3 Considerations on the HEMT Structure

For the past 20 years, the evolution of the AlGaN/GaN HEMT structure has taken different routes, each shaped by the pursuit of a specific application. For instance, the AlGaN/GaN HEMT is normally-on (reason why it is called a depletion mode transistor), but from a power switching perspective, normally-off transistors are preferred due to static power consumption, circuit design simplification and safety concerns. Enhancement mode HEMTs are possible but require significant changes, such as the p-GaN gate, the p-AlGaN gate, the cascode con-

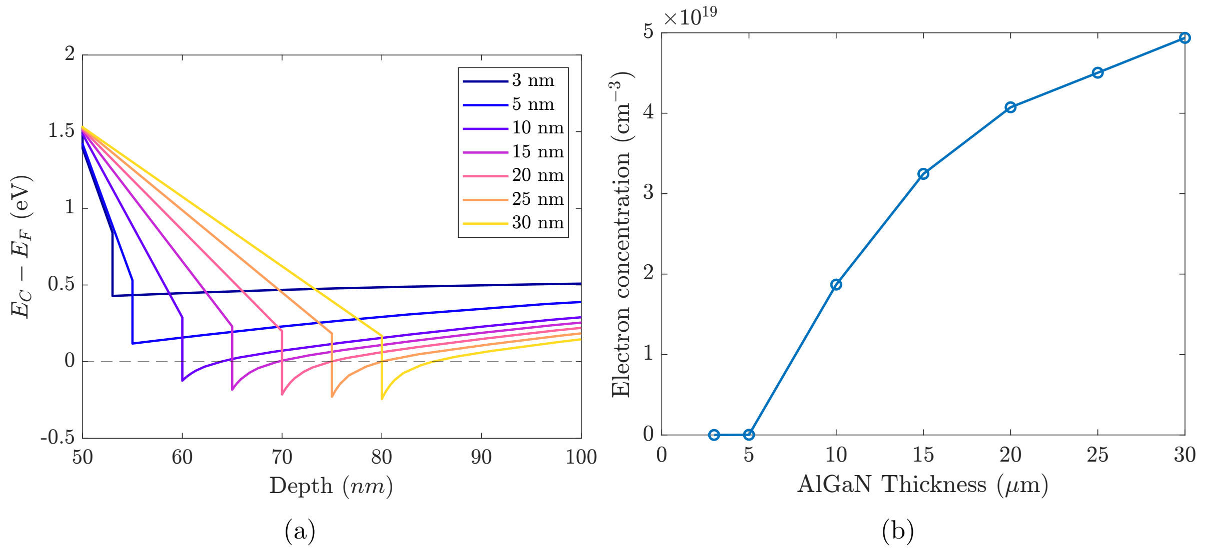

Figure 2.1: TCAD simulations of the (a) band diagram of an AlGaN/GaN heterostructure for various AlGaN thicknesses and respective (b) free electron concentration in the AlGaN/GaN interface, for a surface state at 1.5 eV below the conduction band minimum.

---

figuration or the recessed-gate [67]. Unfortunately, E-mode devices typically underperform comparatively to D-mode ones. The usual culprits are the lower transconductance, lower cut-off frequency, higher parasitic resistances, or lower breakdown voltage [68, 69]. Understandably, the conventional normally-on GaN HEMT is thus consistently treated as the best choice for RF amplification applications.

But even only within the specific group of depletion mode GaN HEMTs lies a world of many different variants, that depend on the device's specific purpose and/or their vendor's manufacturing practices. Besides the fact that most of todays' commercial GaN HEMTs internal structure is a trade secret, addressing the massive field of publications presenting different modifications goes well beyond the scope of this thesis. Here, we focus on what we infer to be the ubiquitous features of commercial off-the-shelf GaN HEMTs and how they will relate later on, based on this work's goal.

The cross-section of a conventional AlGaN/GaN HEMT structure and the corresponding band diagram below the gate is shown in Fig. 2.2.

Substrate: GaN HEMTs are typically grown on top of a crystalline substrate like sapphire, Silicon Carbide (SiC), silicon or diamond. SiC has been a strong option for high power and high-frequency applications, mostly due to its compatible crystal structure and good thermal management [70]. More recently, diamond has been gaining some momentum because of its much lower thermal resistance than any other substrate [71]. On the other hand, silicon is the most cost-competitive solution owing to its low cost and large wafer size [72].

Nucleation Layer: Growing high quality epitaxial GaN films, with smooth surfaces free of cracks, directly on top of the substrate is fairly difficult because of the lattice mismatch and the different thermal expansion coefficients [73]. Moreover, growing GaN on top of SiC substrates results in significant leakage current through the GaN/SiC interface. So, a thin nucleation layer, typically of Aluminium Nitride (AlN), is applied between the buffer layer and the substrate for strain accommodation and increased interface resistivity [74, 75].

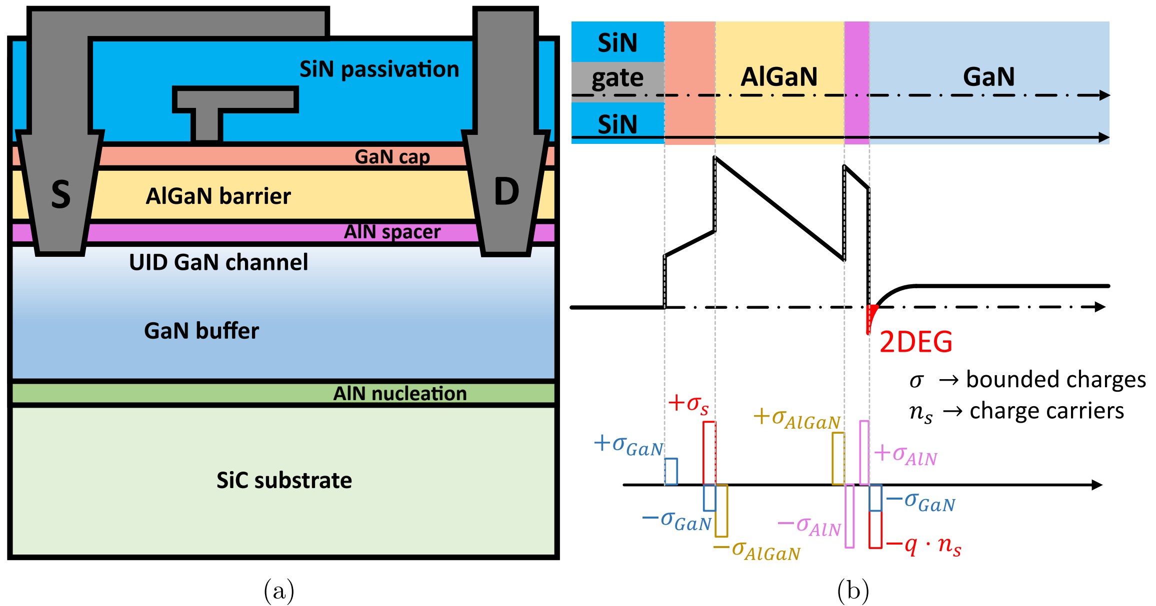

Figure 2.2: (a) Conventional cross-section of an AlGaN/GaN based HEMT structure (not at scale) and (b) corresponding depiction of the band diagram and sheet charge concentrations.

Buffer Layer: The buffer layer is then used to separate the channel region from the remaining threading dislocations and contaminants that might migrate from the substrate, with thicker buffer layers (few μm) effectively improving the 2DEG mobility [65]. The optimum buffer layer thickness depends on many other aspects like the desired breakdown voltage, thermal resistance, screening from defects and polarization induced fields [76].

The buffer layer is also the source for the dominant trapping effects, and so it is no surprise that there has been extensive research on finding alternatives to its present state. Typically, this layer is made of a thick film of semi-insulating GaN. As undoped GaN is intrinsically n-type, because of background contamination that occurs during the growth phase, the buffer layer is doped with deep level acceptors, such as iron (Fe) or carbon (C), to suppress potential leakage. However, even an intrinsically wide bandgap semiconductor can conduct current if charge is injected into it. Considering that the aggressive scaling of gate length, in the pursuit for higher operating frequencies, has intensified short-channel effects such as punch-through or Drain Induced Barrier Lowering (DIBL), the refinement of the buffer quality is no longer enough [77]. It has been shown, however, that the presence of ionized traps in the buffer also helps prevent these effects by improving the channel confinement [78, 79].

Buffer traps are, therefore, essential for the proper operation of most HEMTs. To deem them unnecessary requires a completely different approach to channel confinement. The most common alternatives are to substitute the GaN buffer or simply introduce an additional thin layer, using, for instance, Indium Gallium Nitride (InGaN) [80], AlGaN [81, 82], or AlN [83]. The wider bandgaps of AlGaN and AlN or the polarization induced fields by InGaN create what is typically called a back-barrier that confines the electrons to the channel region. Despite their potential to eradicate buffer doping, there have been some problems pointed out to these approaches. The additional interface layers often cause degradation to the 2DEG mobility and introduce further thermal boundary resistances that hinder the effectiveness of heat flow through the substrate [84]. Moreover, despite the absence of intentional deep-level accep-

tors, the difficulty in achieving high crystalline quality in these layers can also introduce their own trapping centers [85]. More innovative structures, like a buffer-free AlGaN/GaN HEMTs have been proposed, where it has been shown that this device preserves the 2DEG transport properties while simultaneously improving thermal management and potentially enhancing the channel confinement. However, at the current stage, the large concentration of active trap sites, possibly due to background contamination, threading dislocations and/or trap levels at the GaN/AlN interface, retains most of the trapping impact observed in conventional buffer-doped HEMTs [86, 87]. Although not meant for rf power amplification, further improvements have been reported with the application of this technique to a buffer-free GaN-on-SiC Metal Insulator Semiconductor (MIS)-HEMTs [88].

Spacer Layer: To ensure the highest 2DEG mobility, the channel region relies on a high quality unintentionally doped GaN layer. On top of that, a common method to further improve the 2DEG mobility is to add a thin AlN spacer layer (~1 nm) between the channel and the barrier layer. Ternary (like AlGaN) or higher order alloys induce alloy disorder scattering because of the random position of their constituent atoms. The large energy barrier introduced by the AlN spacer layer prevents the 2DEG electrons from penetrating the barrier, which reduces the additional alloy scattering [89, 90].

Barrier Layer: As we previously saw, the barrier layer embodies the wide bandgap semiconductor in Dingle's structure. It can be made of AlN [90] or InGaN [91], or other wide bandgap alloys, but the vast majority of published material tends to the conventional AlGaN. Based on the layer thickness and molar concentration of aluminum it is possible to have a precise control of various features of the transistor. For instance, the alloy composition sets a trade-off between a large enough conduction band offset relative to the GaN channel layer to ensure good electron confinement, and a low thermal and lattice mismatch to prevent high density of structural defects. Likewise, the barrier thickness also considerably impacts the concentration of the 2DEG and the threshold voltage [61].

Part of the large gate leakage current under high reverse gate bias conditions has been credited to a trap assisted tunneling mechanism in the barrier layer. The description of these traps has been somewhat erratic, with some pointing to a well defined activation energy around 0.5 eV [92, 93], others to a practically thermally independent trap (or very small activation energy) [40], and others to threading dislocations that manifest as a continuum of trap states [94].

Cap Layer: The incorporation of a thin GaN film (few nm), designated as the cap layer, on top of the barrier layer enhances the effective Schottky barrier height [95]. The presence of the cap layer has also been linked to a partial suppression of gate lag [96].

Passivation Layer: The passivation of the HEMT surface has been one of the most successful approaches to mitigate gate lag. Applying a thin layer of a dielectric material, usually Silicon Nitride (Si_3N_4), compensates for the deep surface/interface states, responsible for the slow current collapse observed in older devices, by introducing shallow donors [97–99]. The typical concern with this layer is the increase of the input capacitance, that limits the maximum frequency of operation, because of the large dielectric constants of these materials [100, 101].

Field Plate: Despite the success of the passivation layer to suppress gate lag, the continuous stress caused by the large electric fields near the gate terminal degrades the reliability of this layer. So, the use of source-connected and gate-connect field plates are usually employed to reduce the strength of these fields which, consequently, reduces the gate tunneling injection current responsible for charging the surface traps [102].

2.4 An HEMT's TCAD Template

Now that we have a comprehensive view of the HEMT epi-structure we can create our own TCAD template to develop a qualitative understanding of how the relevant trap centers work. Note that for the purpose of this section we will use a simpler TCAD template than the ones typically needed to accurately fit a real device. As we illustrated above, modern devices are composed by many layers that are not actually required to understand the HEMT. For instance, we do not need to add the spacer layer to guarantee a reasonable channel mobility if we simply opt to not account for the alloy scattering. Another simplification that should be made is respective to the theoretical treatment behind charge transport in a semiconductor. As far as the author knows, there is no strong evidence suggesting the need for a more complex model than the drift-diffusion to represent the important features of an HEMT. In fact, one of the physics-based compact models chosen as the HEMT standard by the Compact Model Coalition is the ASM-Model, built from the drift-diffusion model [103].

The HEMT cross-section selected for our TCAD template is illustrated in Fig. 2.3. The TCAD simulation details follow very closely to the ones described in [104]. The 2D numerical simulations were performed in Synopsys Sentaurus TCAD device simulator [105]. The physical model parameters were selected to approximately fit measured DC characteristics of commercial GaN-on-SiC HEMTs. The work function of the gate Schottky contact was set to 5 eV. Nonlocal electron tunneling was activated at the source and drain contacts with a work function of 4 eV, to mimic ohmic contacts. The surface donors were placed in a single energy level 1 eV below the conduction band minimum with a density of 10^{15} cm^{-2}. Equal fixed charge density, 10^{13} cm^{-2}, was placed on both interfaces of the barrier layer, but with opposite polarity to simulate the polarization-induced sheet charges. Several physical models of the TCAD library were incorporated, namely temperature and doping-dependent mobility, high-field velocity saturation (Canali Model), thermionic emission, Fermi statistics and SRH recombination. Self-heating effects were not considered in any of our TCAD simulations.

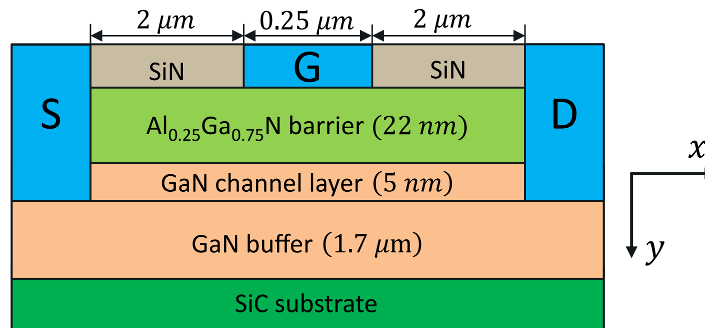

Figure 2.3: Schematic cross-section of the simulated AlGaN/GaN HEMT TCAD template (not to scale). The width of the device was set to 1 mm.

2.4.1 Buffer Traps

At this stage, the only deep-level traps included in the TCAD template were the surface donors which, as we saw, are necessary to supply the channel with free electrons. Note, however, that the same could be achieved through shallow donors. By looking to the IV characteristics of our model in Fig. 2.4 with and without acceptor-level traps in the buffer

layer, we can promptly see their importance to the standard HEMT performance. In the absence of these traps, the device would be unable to cut-off, leading to massive sub-threshold current leakage.

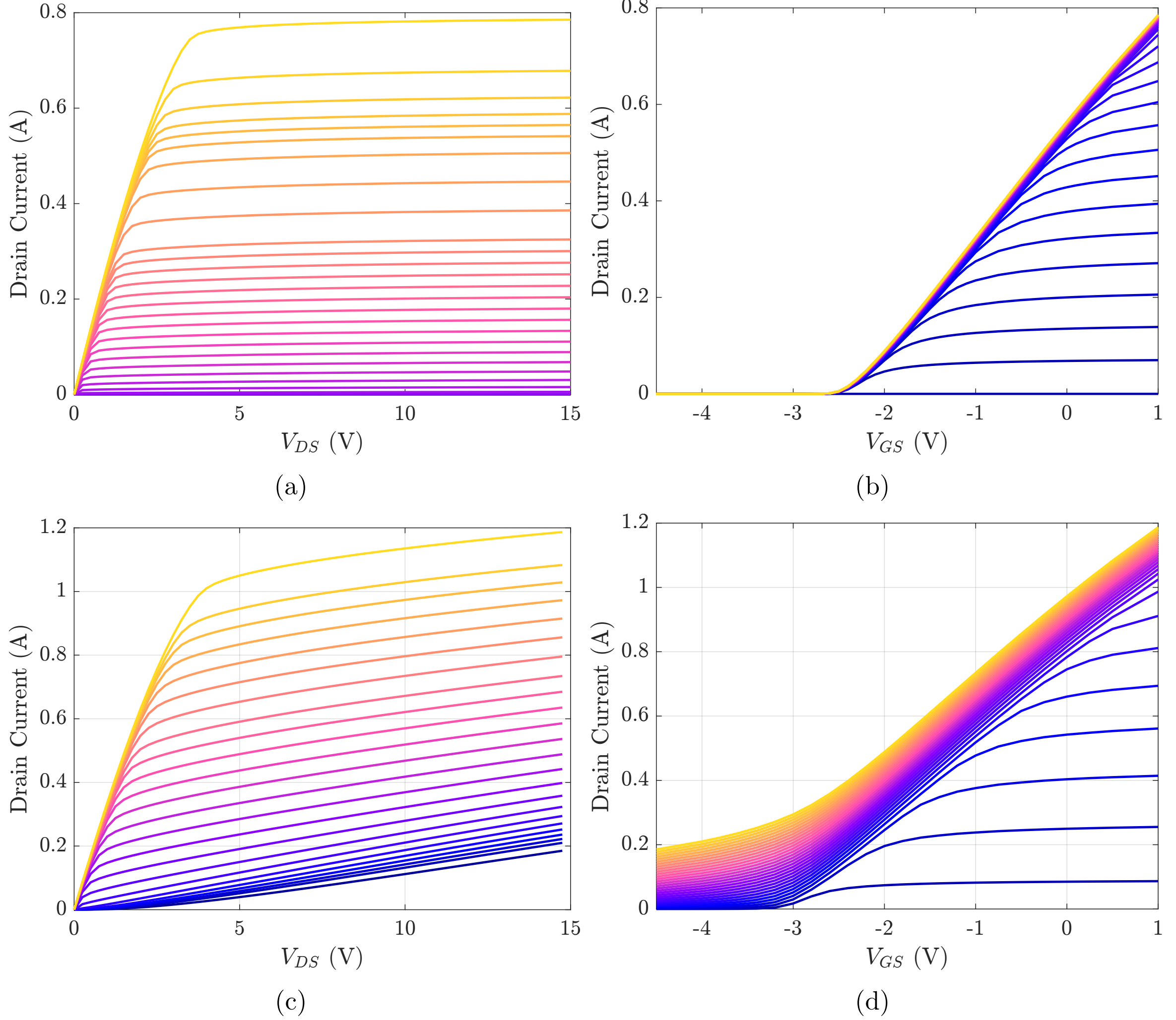

Figure 2.4: Simulated IV characteristics of an AlGaN/GaN HEMT (a - b) with and (c - d) without buffer traps. The traps were placed solely on the buffer region with a single energy level 0.5 eV below the conduction band minimum (as typically extracted in Fe-doped buffer layer) with a density of 5×10^{17} cm^{-3} uniformly distributed.

2.4.2 Lateral Buffer Leakage

To better understand how buffer traps produce their effects, particularly the mechanism behind the drain-lag phenomena, we designed the following pulsed experiment plotted in Fig. 2.5(a). For this test, v_{GS} was kept constant throughout the pulse and, again, no self-heating effects were considered. The surface donors were also probed and there was no significant changes on the concentration of ionized surface states throughout the pulse test. The drain current transients observed during constant v_{DS} segments are thus only due to trapping effects

caused by buffer traps. Fig. 2.5(b) shows the typical trapping-induced current recovery transient observed in most AlGaN/GaN HEMTs.

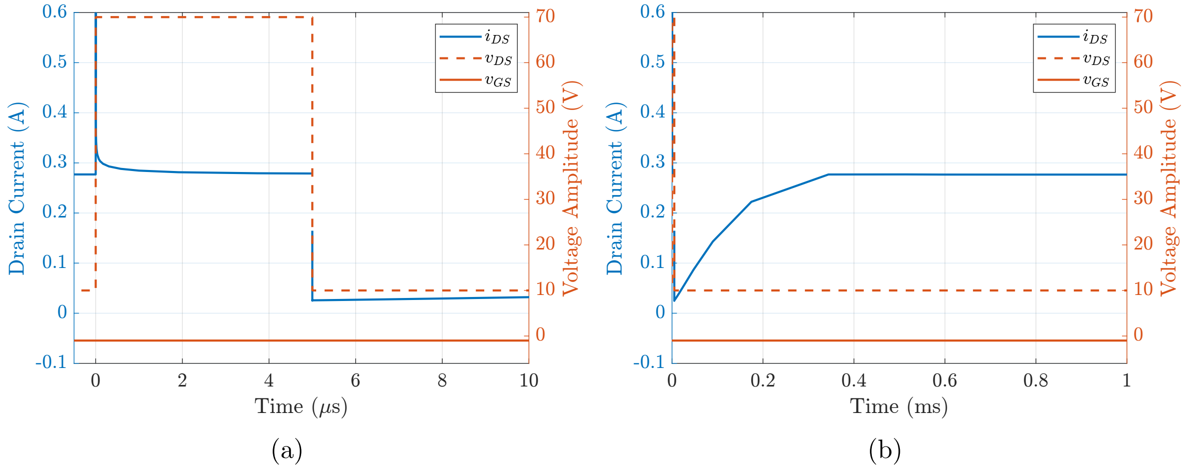

Figure 2.5: Simulated drain-lag effect: (a) applied v_{GS} and v_{DS} and corresponding i_{DS}; (b) zoom-out of the previous profiles to highlight the slower recovery transient.

Fig. 2.6(a) and (b) illustrate the simulated concentration of trapped and free electrons, respectively, over an area that covers the entire length of the HEMT, going from the SiN/AlGaN interface (bottom part, $y = 0$) up to $y = 0.4$ μm deep in the buffer, for different time frames. The top left side plot corresponds to the time immediately before the pulse rise and the remaining five plots are all respective to the pulse segment where $v_{DS} = 70$ V. As can be seen, the highest concentration of ionized trap centers cluster around the drain-side gate-edge. Moreover, it is worth noting that during the first instances, right after v_{DS} raises to 70 V, there is a significant concentration of free electrons in the buffer layer that fades away with time, while the opposite is seen for the trapped electrons.

To better understand these results, Fig. 2.7(a) and (d) shows how a completely formed channel, at time 0^- (blue lines), becomes completely unconfined, i.e. electrons are free to move also in the buffer layer, at time 0^+ (orange lines), when v_{DS} is quickly raised. This happens because the drop of the conduction band minimum, imposed by the large v_{DS}, forces a large injection of 2DEG electrons into the buffer. At this time, no capture is yet taking place, reason why we see the exact same spatial distribution of trapped electrons before and after the drain voltage rise. However, just after 5 μs, the conduction band minimum is up again, as shown in Fig. 2.8(b), although not to its initial value since we still have the 70 V applied, and the 2DEG appears confined again to the vicinity of the AlGaN/GaN interface. This is simply a consequence of the negative charge accumulation in the buffer region. Nevertheless, it is interesting to note that, from an electrostatic point of view, it does not matter if this charge accumulation comes from an increase of free or trapped electrons. Hence, besides the initial amount of free electrons injected into the buffer, at time 0^+, there must be further injection happening throughout the pulse to justify the rise of the conduction band minimum.

Since the transport mechanisms governing these TCAD simulations are based on the drift-diffusion model, a possible way to understand this continuous injection is by seeing it as a balance of drift and diffusion forces. At time 0^+, when v_{DS} reaches its maximum value

we already have a large amount of free electrons in the buffer region. Once these electrons start getting trapped, as they are now in close proximity with buffer traps, the free electron concentration imbalance between the channel and the buffer regions prompts more electrons to diffuse into the buffer. On average, the amount of negative charge in the buffer layer increases, pushing the conduction band minimum upwards, as depicted in Fig. 2.8, which in turn reinforces a better 2DEG confinement. Eventually, the amount of negative charge in the buffer is high enough so that the induced electrostatic potential compensates the concentration gradient, and an equilibrium condition is reached.

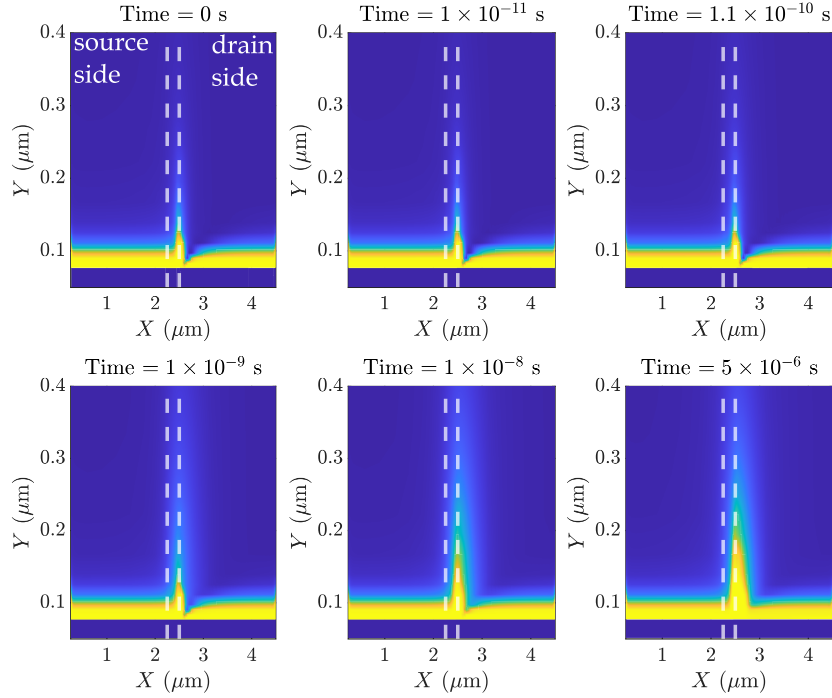

(a)

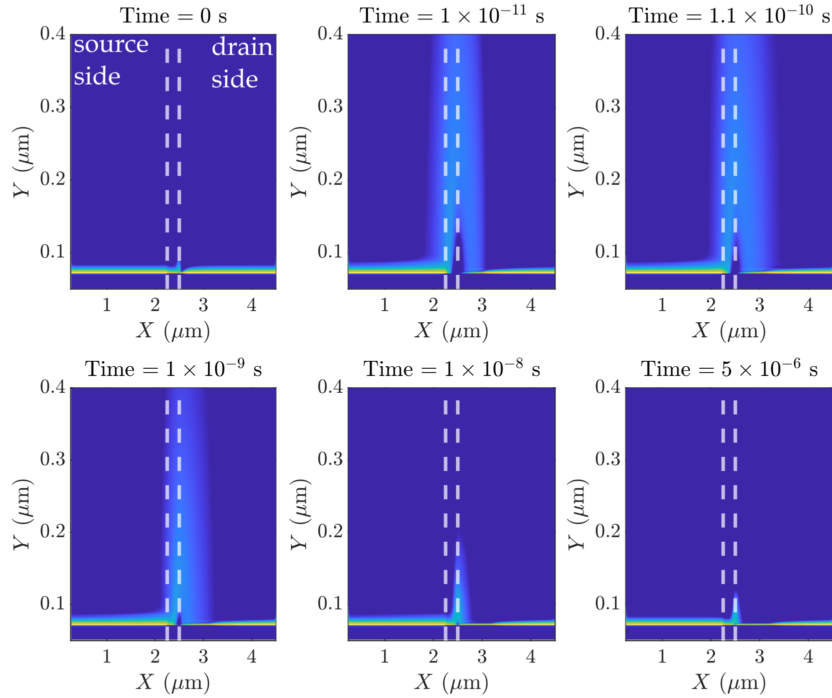

(b)

Figure 2.6: Simulated cross-section of the HEMT in different time frames, all when $v_{DS} = 70\tilde{V}$, i.e. when the capture process dominates. The horizontal and vertical axis correspond to x and y directions, respectively, with the drain terminal on the right hand side and the substrate on the top part of the plot. The vertical dashed white lines are the gate limits. Yellowish colors represent a higher concentration of (a) trapped electrons and (b) free electrons.

The outcome of this process, illustrated in Fig. 2.7(b) and (e), shows why buffer traps are essential at preventing lateral buffer leakage. Finally, when v_{DS} is pulsed down, the 2DEG concentration is lower than the initial condition even though the external bias is the same, as reported by Fig. 2.7(c) and (f) (although the peak concentration is higher near the interface the overall channel concentration is lower). The difference in concentration of the initially available electrons, at 0^{-}, and the current ones, at time $5^{+}\mu$s, lies trapped in the buffer region. During the recovery stage, trapped electrons are thermally excited to the conduction band and then diffuse back to the channel, just like an inverted capture process, up to the point where the initial conditions are met again.

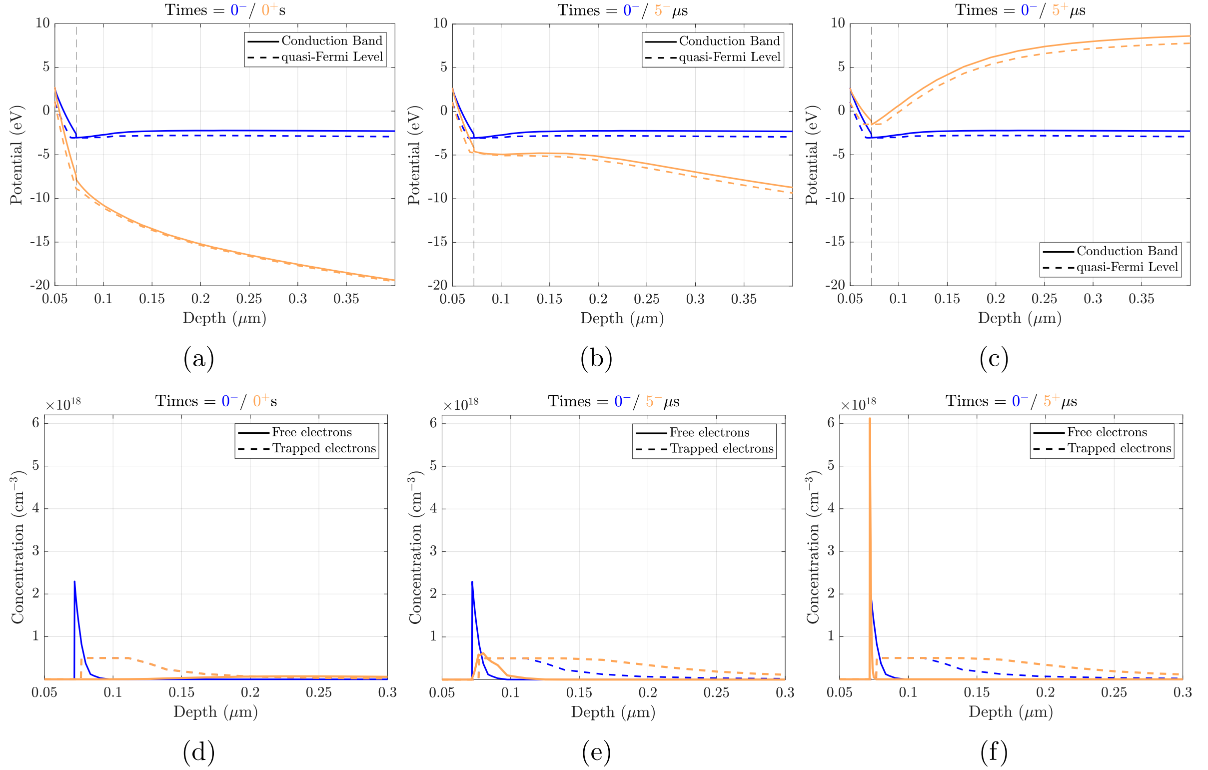

Figure 2.7: Simulated conduction band minimum (solid line) and quasi-Fermi potential (dashed line) profiles, obtained from a vertical cutline aligned with the drain side of the gate-edge, (a) right before (blue - represents the initial quiescent state) and immediately after the rise of v_{DS} (orange); (b) at the initial quiescent state (blue) and after 1 μs with $v_{DS} = 50$ V (orange); (c) at the initial quiescent state (blue) and immediately after pulsing down v_{DS} back to 5 V (orange). The vertical dash line, in the previous 3 plots, represents the AlGaN/GaN interface. From (d-f), we compare the same time frames as above, using the same color code, but now showing the free (solid line) and trapped (dashed line) electron concentration vertical profiles.

Since we are in a simulation environment, we have access to all the internal variables at all times. The previous narrative can then be corroborated by looking to the variation of the total number of free and trapped electrons in both the channel and buffer layers over time, as well as to an average of the conduction band minimum in those regions.

Fig. 2.8(a) tracks the total number of electrons in the GaN region of the HEMT over time

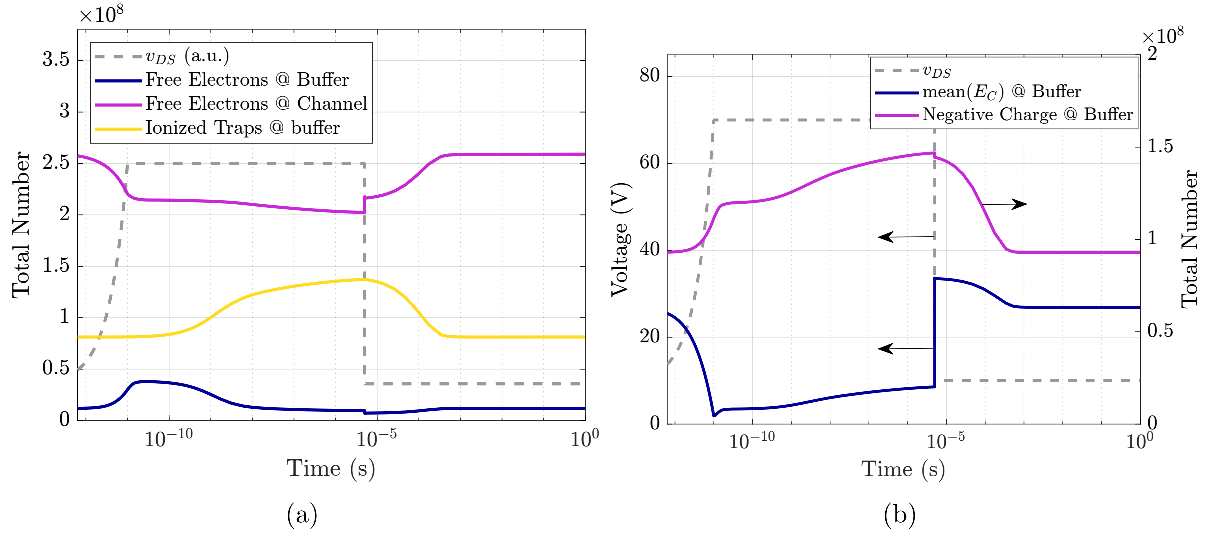

Figure 2.8: Simulated (a) total number of free electrons in the buffer and channel layers, and ionized trap centers in the buffer over time. (b) Spatial average of the conduction band minimum in the buffer layer (left axis) and sum of the all negative charge in the buffer layer (right axis).

---

superimposed to the drain voltage pulse. The initial rise of v_{DS} is accompanied by an equally fast injection of free electrons into the buffer. Please note that while v_{DS} is changing, not only we have a redistribution of charge between the channel and the buffer caused by drift currents, but also a redistribution between the channel and the gate metallization (in fact, this is what gives rise to the intrinsic C_{gd}). Once v_{DS} stabilizes, a substantial amount of trap centers become ionized just after a few hundreds of picoseconds, and with that a reduction of free electrons in the buffer. While this is happening, the total number of electrons in the channel layer keeps steadily dropping. Looking to Fig. 2.8(b), we can see that the total amount of negative charge (free and trapped electrons) in the buffer layer increases monotonically throughout all 5 μs, when $v_{DS} = 70$ V. This validates our previous explanation, where we explain the increase of the conduction band minimum as an iterative process animated by a charge imbalance between the channel and the buffer. Please note that, if the capture transient was described by a simple one-step process, i.e. a single initial injection of free electrons into the buffer followed by some dynamical process between neutral traps and the available free electrons, then we would not be able to see the conduction band minimum uprise from Fig. 2.7(a) to (b), since the initial injection would already set the total negative charge in the buffer. Instead, what we see is a monotonic increase of the conduction band minimum present over the entire width of the pulse.

Chapter 3

Modeling Buffer Traps

For modeling purposes, the static and dynamical characteristics of trapping effects are two different entities that require their own set of characterization methodologies and models. The static behavior represents the instantaneous relationship between the variable of interest, typically the drain current, i_{DS}, and the applied biases to the device, $(v_{DS}, v_{GS}, T, v_{trap})$, where v_{trap} is a conceptual variable that symbolizes the average concentration of trapped charge in the device (i.e. a lumped interpretation). Two additional links must then be considered: (i) the forcing function, that relates the excitation to the trapping state, $v_{trap} = f(v_{DS}, v_{GS}, T)$; (ii) the impact of the trapping state to the variable of interest, $i_{DS} = g(v_{trap})$. Fig. 3.1 illustrates these relationships by showing the impact of different drain quiescent voltages on the drain current. The use of a pulsed measurement system allows us to assume that the temperature is practically the same at all points, so the only change between the profiles at different colors is the trapping state.

The dynamical behavior is associated to the inherent dynamics of trap centers and will be the starting point for this chapter.

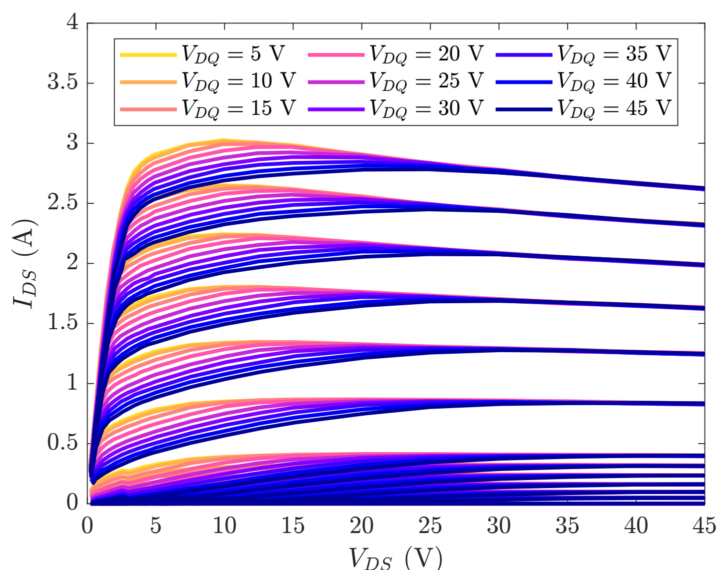

Figure 3.1: Pulsed IV curves of a GaN HEMT for various drain quiescent voltages.

3.1 Shockley-Read-Hall Model

There are many mechanisms by which electrons and holes can interact with an impurity. Concerning buffer traps in AlGaN/GaN HEMTs, the SRH generation-recombination model [106] is considered to be the dominant one. The basis of this model can be easily understood with a single energy level (or two charge condition) in the semiconductor bandgap [107], and then generalized to multiple levels [108] if needed. The trapping/recombination dynamics in a SRH center is described by two emission and two capture processes illustrated in Fig. 3.2. The net rate of change of electron and hole concentration in the conduction and valence band caused by these four processes are given by

$$\frac{dn}{dt} = (b) - (a) = e_n n_T - c_n n(N_T - n_T) \tag{3.1}$$

$$\frac{dp}{dt} = (d) - (c) = e_p(N_T - n_T) - c_p p n_T \tag{3.2}$$

where n and p are the concentration of free electrons and holes in the conduction and valence band respectively, N_T is the concentration of SRH centers and n_T is the concentration of occupied SRH centers. $e_{n,p}$ are the emission coefficients (s^{-1}) and $c_{n,p}$ are the capture coefficients ($cm^3\ s^{-1}$), defined as the product of the capture cross section (cm^2) and the thermal velocity of charge carriers ($cm\cdot\ s^{-1}$). It helps to visualize this product as if the charge carriers are immobile and the centers move randomly at the thermal velocity. The charges that have the highest probability of getting caught are the ones that are found inside the volume created by the moving centers. The value of the capture cross-sections can vary extensively if the center is either neutral or ionized. A negatively charged center, for instance, will have a smaller electron capture cross section than a neutral or positively charged one. Neutral centers have cross-sections on the order of 10^{-15} cm^2 [109, 110].

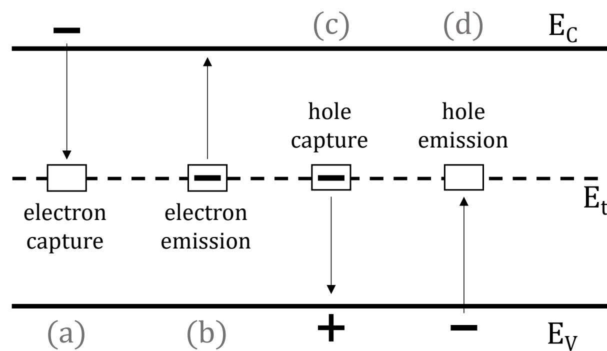

Figure 3.2: Schematic representation of the 4 basic processes involved in the SRH model for a single energy level. (a) Electron capture; (b) electron emission; (c) hole capture; (d) hole emission. Adapted from [106].

The typical approach to reach an analytical expression for the characteristic time constant of the SRH dynamics starts from two main assumptions: (i) a nondegenerate semiconductor, i.e., $n \ll N_C \approx 1 \times 10^{19}$ cm^{-3}, so that the concentration of free electrons follows a Maxwell-Boltzmann distribution; (ii) the relationship of the capture and emission coefficients derived from the principle of detailed balance in equilibrium extends to non-equilibrium conditions.

The domain of validity for these two assumptions is not well defined, as far as we know, and so it is difficult to pinpoint the exact situation in which they break. For the case of buffer traps in an AlGaN/GaN HEMT, for instance, there are two indications that might suggest a problem with these two assumptions. First, the channel region, where the 2DEG exists, is deeply degenerated. It is therefore possible that the adjacent site, populated by buffer traps, may not follow a Maxwell-Boltzmann distribution. Second, since we are dealing with a high-power device, it is only natural the presence of strong electric fields, which could compromise the latter assumption.

However, assuming these assumptions indeed hold, we can relate the capture and emission coefficients to reach the simplified final SRH form

$$\frac{dn}{dt} = c_n g_n N_C e^{\frac{E_T - E_C}{k_B T}} \left[n_T - (N_T - n_T) e^{\frac{F_n - E_T}{k_B T}} \right] \tag{3.3}$$

$$\frac{dp}{dt} = c_p g_p N_V e^{\frac{E_V - E_T}{k_B T}} \left[(N_T - n_T) - n_T e^{\frac{E_T - F_p}{k_B T}} \right] \tag{3.4}$$

where N_C and N_V are the effective density of states in the conduction and valence band, respectively, E_C and E_V are the minimum of the conduction band and the maximum of the valence band, respectively, E_T is the SRH center energy level, $g_{n,p}$ is the ground-state degeneracy that accounts for the charge carrier spin and the band degeneracy, and F_n and F_p are the quasi-Fermi levels for electrons and holes, respectively [111–113]. These two equations create a complete description of the possible processes in a single level SRH center. Under certain conditions some processes dominate, deeming the SRH center either a trap or a recombination-center. For instance, when the rate processes $a \to b \to a \to b \to ...$ dominates, the SRH center behaves as an electron trap. When the dominating sequence is $a \to c \to a \to c \to ...$ then it is a recombination event while generation events follow the sequence $b \to d \to b \to d \to ...$. Whether an SRH center acts as a trap or a R-G center depends on the trap energy level, the Fermi level, the temperature, and the capture cross-sections. A more complete depiction of the formal criteria is presented in [107]. Generally, defects with an energy level near the midgap behaves as a R-G center whereas near the band edges act as traps [109].

Since 3.3 and 3.4 are nonlinear differential equations, they do not possess defined emission and capture time constants. Despite that, we often see the equivalent time constant for an electron trap defined as

$$\tau^{-1} \approx \sigma_n \langle v_{th} \rangle g_n N_C e^{\frac{E_T - E_C}{k_B T}} \left(1 + e^{\frac{F_n(t) - E_T}{k_B T}} \right) \tag{3.5}$$

This expression is notoriously important because underlies most characterization techniques to extract the trap's fingerprints, namely the activation energy, $E_T - E_C$ or $E_T - E_V$, and the capture cross-section. To understand that we need to ascertain the temperature influence on the trapping time constant. The average thermal velocity is given by $\langle v_{th} \rangle = \sqrt{\frac{3k_B T}{m^*}}$, where m^* is the carrier effective mass. Assuming parabolic bands, the effective density of states in the conduction band is given by $N_C = 2g_v(\frac{2\pi m^* k_B T}{\hbar^2})^{3/2}$. So, $N_C \langle v_{th} \rangle \propto T^2$. According to first principle calculations, σ_n can also display some temperature dependence. However, it seems that this is only noticeable at very high temperatures (thousands of Kelvin) which clearly falls out of a typical PA operating condition [113, 114].

When the emission process dominates, the exponential term inside the brackets in 3.5 gets very small. The emission is then described by an exponential decay whose time constant is approximately determined by

$$\tau_e^{-1} \approx AT^2 e^{\frac{E_T - E_C}{k_B T}} \tag{3.6}$$

where A incorporates the remaining temperature independent parameters and constants. From 3.6, we can now obtain the standard modified Arrhenius equation that allow us to extract the trap activation energy and capture cross-section from the slope and the y-intercept, respectively [114]. Bias-dependent effects, like the Poole-Frenkel effect, might alter the emission time constant described in 3.6 by changing the apparent activation energy. Supposedly this effect is only noticeable in traps that are neutral when charged (donor-like), and indeed this effect has been reported absent in Fe-doped buffers (thought to act as acceptor-like traps) [115]. This, however, may be different in a C-doped buffer.

When the capture process dominates, the exponential term inside the brackets in 3.5 becomes much larger than 1, which allow us to obtain the fastest rate reached during a capture transient as

$$\tau_c^{-1} \approx c_n g_n n \tag{3.7}$$

Naturally, as the capture process progresses and n continues to decrease, the capture rate tends to the emission rate up to the point in which they equal each other, and so steady-state is reached. A curios aspect of 3.7 is that the capture rate is independent of the trap's energy level and depends only on the local concentration of free electrons.

The notion of a clearly separated and fixed capture and emission time constants is therefore not supported by the SRH model. In fact, as we will show later on, even the measurements contradict this common belief. Nevertheless, the simplicity associated to this assumption has led to a widespread adoption of the so-called Jardel model [116].

3.1.1 Additional Considerations on the Trap Mechanisms

The SRH model for a single trap level under isothermal conditions predicts an emission transient that is practically described by a pure exponential profile (whose time constant depends on the trap cross-section and activation energy). However, experimental results often display more complex phenomena. Fig. 3.3 shows the emission transients extracted from two similar (i.e. same epitaxial structure) AlGaN/GaN HEMTs, both with a Fe-doped buffer layer. Although both devices share the same dominant time constant, the device on the left has two distinct inflection points, whereas the one on the right has only a single inflection point with, what can only be described as, a compressed transient. The absence of a pure single time constant detrapping behavior has been linked to different phenomena such as: a capture/emission process based on hopping or trap assisted tunneling; the presence of trap states in alloys, like the AlGaN, that may cause band splitting; the influence of a spatially varying electric field; among others [40, 117]. A more recent work has demonstrated quantitatively how a continuum of trap levels, even in the case of a non-uniform energetic probability density function, leads to a stretched detrapping transient as seen in the measurements [118]. Furthermore, the presence of 1/f noise, something that has been well reported on GaN HEMTs [119], has been explained through the existence of multiple traps with distinct time constants [120].

For the purpose of this work, namely connecting trapping effects to the PA linearizability, we found no significant need to model trapping effects to that extent. Furthermore, despite

the lack of a pure exponential emission profile in the measurements, we still (and this will be shown in the next chapter) achieve an highly linear Arrhenius plot with the collected dominant time constant and an activation energy consistent with the literature. In other words, the SRH model for a single trap level seems a reasonable approximation for a non-pure exponential emission profile. On the other hand, as we mentioned in section 2.3, part of the gate leakage under high reverse gate bias has been credited to a trap-assisted tunneling mechanism. Such phenomena falls outside the domain of applicability of the SRH model, and requires different modeling approaches [94, 121]. According to our own experience, these non-SRH phenomena are not as meaningful as drain-lag is to the PA performance, hence these secondary effects will be out of this work's scope.

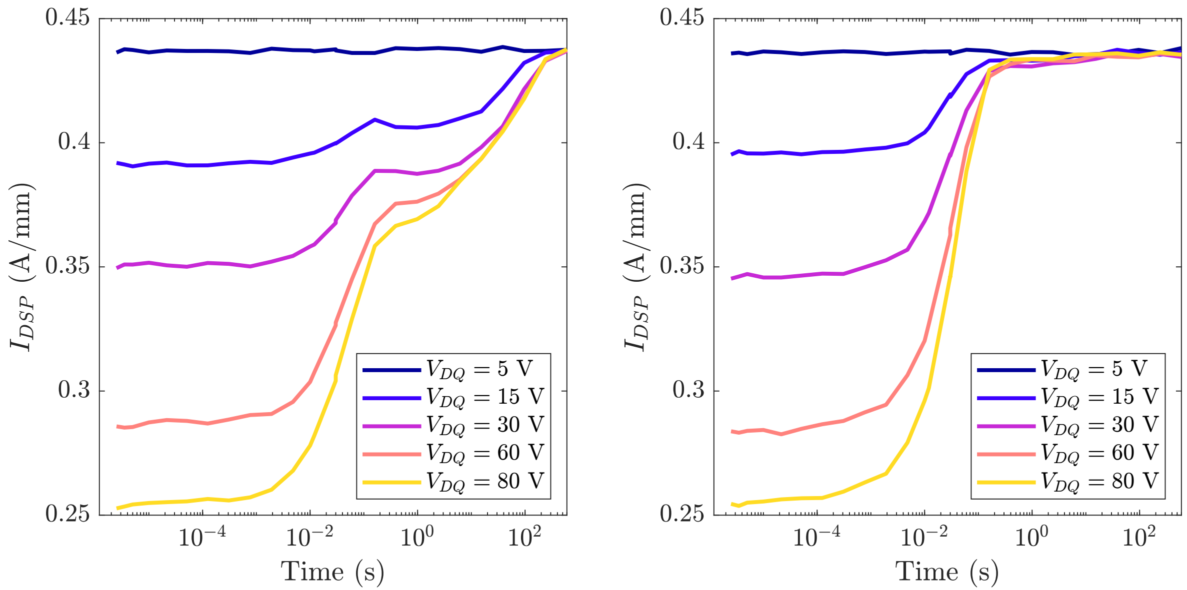

Figure 3.3: Isothermal recovery transients measured, at $(v_{DS}, v_{GS} = (5, -1)$ V for various initial drain quiescent voltages and $V_{GSQ} = -5$ V, from two similar AlGaN/GaN HEMTs both with a Fe-doped buffer layer.

3.2 The Equivalent-Circuit Model of Buffer Traps

3.2.1 Kunihiro and Ohno Model

One of the first large-signal equivalent circuit description of drain-lag in GaN HEMTs, if not the first, was published in 1996 by Kunihiro and Ohno [122]. The novelty of their work lies in that they took the self-backgating effect, in which the traps below the 2DEG act as a pseudo-backgate terminal, typically modeled by a simple RC circuit with a single time constant and made it more physically supported by incorporating the SRH model. The notion of a backgate terminal is particularly useful from a modeling perspective because trapping effects can then be incorporated in the drain current model simply as a threshold voltage shift, $v_{trap} \propto \Delta V_{th}$. Fig. 3.4(a) illustrates the idea behind the Kunihiro and Ohno equivalent circuit model, where the traps are presumed to be in the epitaxial interface between the buffer and the substrate.

In their work, they assume that the backgate potential variation, Δv_{trap}, is proportional to the deviation of the trapped sheet charge density (here assumed $[n_T] = cm^{-2}$) by the following equation

$$\Delta v_{trap} = -\frac{q\Delta n_T}{C_B} \tag{3.8}$$

where $C_B = \frac{\epsilon_B}{y_B} = C_{SB} + C_{BD}$, ϵ_B is the dielectric permittivity of the buffer layer and y_B is the distance from the 2DEG to the traps. Note that v_{trap} will also be proportional to the applied v_{DS} according to the resistive dividers that are either defined by the capacitances at high frequencies or by the resistors at low frequencies, as illustrated in Fig. 3.4(b). The relationship between v_{DS} and v_{trap} defines the system's forcing function.

The electron capture and emission are represented by the parallel circuit consisting of a diode, D_B, and a resistor, R_B, that arises naturally from a first-order approximation of the SRH model. For that, they considered a small-signal excitation,

$$n = n_0 + \Delta n = n_0 e^{\frac{F_n - E_0}{k_B T}} \tag{3.9}$$

where n_0 and E_0 are the intrinsic carrier density and the intrinsic Fermi energy, respectively. They then proceed to assume that the argument of the exponential equals the backgate voltage deviation, $F_n - E_0 = q\Delta v_{trap}$.

Substituting (3.8) and (3.9) in (3.1) and neglecting second order terms, results in the expression that motivated the diode for the capture (first term of the right side) and the resistance for the emission (second term of the right side), as illustrated here

$$\frac{d\Delta n_T}{dt} = \frac{n_{T_0}}{R_B C_B}\left(1 - \frac{n_{T_0}}{N_T}\right)\left(e^{-\frac{q^2 \Delta n_T}{C_B k_B T}} - 1\right) - \frac{\Delta n_T}{R_B C_B} \tag{3.10}$$

where $(R_B C_B)^{-1} = e_n + c_n n_0$, is the characteristic frequency of the system in equilibrium and $n_{T_0} = \frac{c_n n_0 N_T}{e_n + c_n n_0}$, is the steady-state trapped charge concentration obtained from $\frac{dn_T}{dt} = 0$.

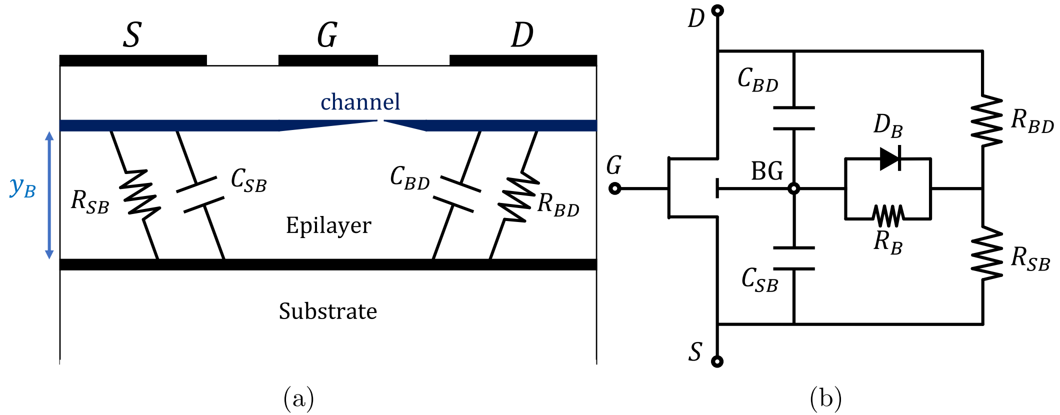

(a) (b)

Figure 3.4: (a) Geometrical interpretation of the equivalent-circuit model and respective (b) equivalent-circuit model for the drain-lag effect conceived by Kunihiro and Ohno [122].

3.2.2 Rathmell and Parker Model

Later, in 2007, Rathmell and Parker published an alternative equivalent circuit model description [123] that did not required the first-order approximation described in the Kunihiro

and Ohno derivation. Following the variables' definitions of [123], knowing that $v_{trap}(t) = \frac{qn_T(t)}{C_T}$, (3.3) can be recast in terms of an effective trap potential, $v_{trap}(t)$, and effective energy $qV_I(t)$,

$$\frac{dv_{trap}(t)}{dt} = \omega_0 \left[V_0 e^{\frac{qV_I(t)}{k_B T}} - v_{trap}(t) \left(1 + e^{\frac{qV_I(t)}{k_B T}} \right) \right] \tag{3.11}$$

where ω_0 is the system's characteristic frequency, equal to τ_e^{-1}, and $V_I(t)$, acting as the forcing function, is assumed to be the result of a linear combination of v_{DS} and v_{GS}, defined as

$$V_I(t) = k_0 + k_1 v_{DS}(t) + k_2 v_{GS}(t) \tag{3.12}$$

in which k_0, k_1 and k_2 are fitting constants. This equation sets a theoretical maximum on the effective trap potential as V_0 and an equilibrium effective trap potential of

$$V_{trap} = \frac{V_0}{1 + e^{-\frac{qV_I}{k_B T}}} \tag{3.13}$$

According to the state equation (3.11), the implementation of the SRH statistics as an equivalent-circuit model can then be described by two voltage-controlled current sources, one for the capture, $i_c(t)$, and another for the emission, $i_e(t)$, as

$$i_S[V_I(t)] \equiv C_T \frac{dv_{trap}(t)}{dt} = C_T \omega_0 \left[V_0 e^{\frac{qV_I(t)}{k_B T}} - v_{trap}(t) \left(1 + e^{\frac{qV_I(t)}{k_B T}} \right) \right] = i_c(t) - i_e(t) \tag{3.14}$$

feeding a conceptual capacitor, C_T, whose voltage, $v_{trap}(t)$ - the state-variable - can modify the transistor characteristics again mainly as a shift in the threshold voltage. Fig. 3.5 illustrates the equivalent circuit model that represents (3.14).

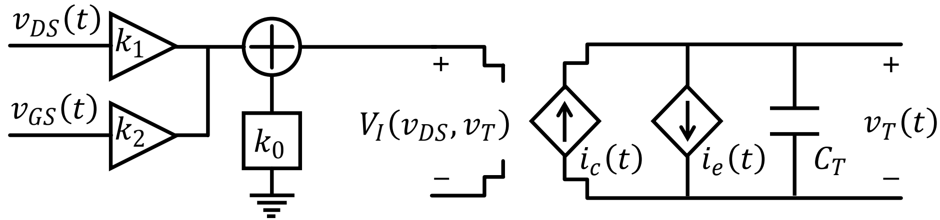

Figure 3.5: Equivalent-circuit model of deep-level traps conceived by Rathmell and Parker [123].

It is interesting to note that, contrary to the Kunihiro and Ohno derivation (where $F_n(t) - E_T \propto \Delta n_T$), here Rathmell and Parker remove the relationship between the state variable, v_{trap}, and the quasi-Fermi level ($F_n(t) - E_T = qV_I$). This apparent small detail can have noticeable implications on the model's response during a capture process. The quasi-Fermi level depends both on the local concentration (chemical potential) and charge (eletrical potential). So, when free electrons turn into trapped charge or vice-versa, we should expect a change to the quasi-Fermi level. However, this dependence is absent in the Rathmell and Parker model. When we pulse v_{DS} to a certain value and remain there, V_I does not change, which implies a fixed F_n, and consequently also a fixed n. Yet, as we previously saw in Fig. 2.7, this is not supported by TCAD simulations. Consequently, the Rathmell and Parker model predicts a constant capture rate, whereas in the Kunihiro and Ohno model, that allows for feedback, as the concentration of free electrons fades, the capture rate becomes steadily slower.

3.2.3 Update on the Rathmell and Parker Model

Based on the flaws highlighted in the previous two models, we developed a simple correction to the Rathmell and Parker model that accounts for the missing feedback element. Everything remains the same except for the forcing function (3.12), which is now defined as

$$V_I(t) = k_0 + k_1 v_{DS}(t) + k_2 v_{GS}(t) + k_3 v_{trap}(t) \tag{3.15}$$

To understand the relevance of this term we performed a transient pulsed simulation on TCAD using the exact same conditions plotted in Fig. 2.5, except now the pulse width is 10 μs. Fig. 3.6(a) and (b) shows the percentage of trap centers that are ionized in the entire buffer over time, when v_{DS} steps up to 70 V and after when it steps down to 10 V respectively, and the best fit obtained (using a nonlinear least-squares algorithm) from the original and the improved Rathmell and Parker model. Although the original model has a slightly better predictive capability for the emission transient, it is clear that the presence of the v_{trap} term in (3.15) adds a major improvement to the accuracy of the trap model during the capture transient.

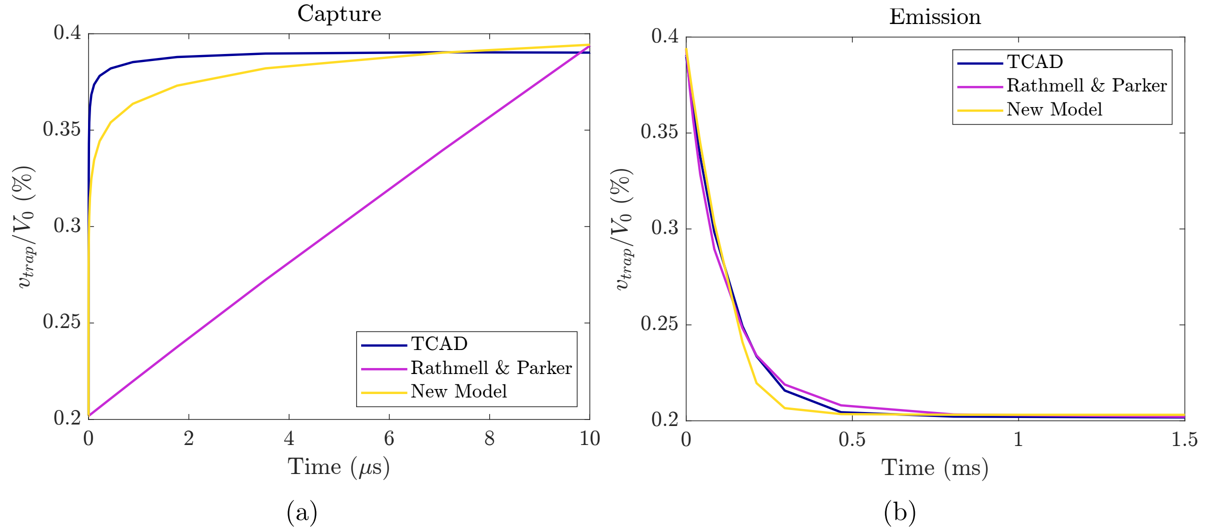

Figure 3.6: Simulated pulsed response on the TCAD template for an input v_{DS} signal and the corresponding percentage of trap centers that are ionized in the entire buffer over time, when (a) v_{DS} steps up to 70 V and (b) after when it steps down to 10 V respectively. The three profiles correspond to the data directly extracted from the TCAD simulations and the best fit obtained from the original and the improved Rathmell and Parker model. Note that v_{trap}/V_0 is the exactly the same as the percentage of ionized trap centers.

Despite the improvement demonstrated in Fig. 3.6, (3.15) remains a crude approximation of the reality presented by TCAD simulations. For instance, this model does not account for the continuous free electron injection into the buffer caused by the charge imbalance between this layer and the channel, as we described in the previous chapter. As far as the authors know, an accurate representation of the trapping dynamics that is physically consistent is still an unresolved subject in the literature.

Chapter 4

Drain-Lag Characterization

Dedicated pulsed I-V measurement techniques have been widely adopted in the study of trapping effects [35]. Despite the many variants of this method (e.g. [40, 124, 125]), the basic idea consists in setting the trapping state with some carefully chosen bias pulse and then measure its influence on the drain or gate current. The main challenge to methods like this, where the trapping is analyzed through the current, is to ensure that electrothermal effects are not perceived as trapping effects. This can be done in multiple ways: by de-embedding the temperature impact on the drain current according to the thermal resistance of the device [40]; by setting the trapping state with some bias pulse while the transistor is off and then measure the current immediately after it is turned on [45]; by varying the bias voltage to maintain the same power dissipation [126]; among others.

After testing many commercial and laboratory pulsed I-V measurement systems and studying many measurement results, the device modeling community became convinced of the following two essential features of the trapping behavior in GaN HEMTs: (i) emission transients can span from several microseconds to several seconds or minutes and (ii) capture transients are much shorter than the minimum duration of even the state-of-the-art pulsed I-V measurement powerheads. Consequently, the capture time constants were normally assumed infinitesimally short, and thus neglected. So, the focus was directed to accurately measure the emission time constants [116, 127, 128]. In fact, it is this large asymmetry between the capture and emission time constants that constitutes the underlying assumption of the double-pulse I-V testers [124]. Also, the idea that one can extract an emission time constant directly from Y_{22} measurements stems again from the assumption that the capture process dynamics are too fast to be observable under excitations at low frequencies.

As we demonstrated in Chapter 3, the SRH model does predict an initial very fast capture transient, but, if we wait enough time, the capture rate should eventually slowdown to the emission rate as more and more traps become ionized. There has been already some experimental evidence that suggests the existence of slow capture time constants [121, 129, 130]. Furthermore, although some claim to have extracted the emission time constant directly from low-frequency Y_{22} measurements, the SRH prediction at small-signal conditions is substantially different than at large-signal conditions [54]. Indeed, when we compare low-frequency Y_{22} with the drain current transients (using pulsed I-V for instance), the reported values display a large disparity between them, with Y_{22} yielding a much lower emission time constant [104, 131]. These issues seem to indicate that more careful should be given to the characterization of the capture transient, not only as a modeling concern but also as a way

to validate the theory.

4.1 The Double Pulse Technique for Transient Analysis

To extract both the capture and emission transients under isothermal conditions, we conceived a double-pulse based experiment whose setup is shown in Fig. 4.1. The core of the present setup is an arbitrary waveform generator to generate the required voltage waveform. Due to the limited output power of this instrument, a fast and high voltage amplifier (pulser) is needed to pulse the device. The drain pulser is able to provide up to 220 W of dc-rated power. Depending on the transistor's region of operation, the pulser head circuit shows settling times ranging from 300 up to 800 ns. A second low-power version of this pulser head is used on the gate. More details on the pulser heads and the measurement setup can be found in [130].

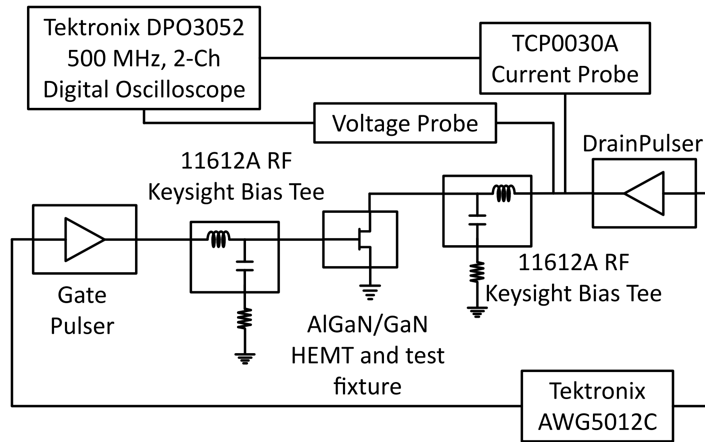

Figure 4.1: Measurement setup. A: dc Power Supplies; B: Tektronix DPO3052 500 MHz, 2-Ch Digital Phosphor Oscilloscope; C: AWG5012C Arbitrary Waveform Generator; E: Drain Pulser; F: Gate Pulser; G: TCP0030A Current Probe; H: CGH27015 GaN HEMT from Cree and test fixture; I: 11612A OPT 001 RF Keysight Bias Tee.

Fig. 4.2 exemplifies a typical $v_{GS}(t)$ and $v_{DS}(t)$ input signals. The selected quiescent conditions in this example are set to $v_{GSQ} = -5$ V and $v_{DSQ} = 5$ V. As shown, first a high-voltage v_{DS} pre-pulse, of variable amplitude V_{Pre}, and variable duration, P_W, is applied to the HEMT, while v_{GS} (-5V) remains below the threshold voltage. This is then followed by v_{DS} stepping down to its initial quiescent state (5 V) and staying there for a few μs, hereafter designated as the test pulse part of the waveform, where the current will be effectively measured. v_{GS} rises immediately after the pre-pulse end, from its quiescent state to some bias well above the threshold voltage, allowing the current to start flowing through the channel. Note that v_{GS} only returns to the off-state after v_{DS} has been first forced to 0 V to avoid any voltage spikes at the bias tee's RF choke.

This procedure is essential to ensure isothermal conditions, since only this way are we able to guarantee that at the beginning of each measurement (following the pre-pulse end) the device's temperature is always the same. This is possible under the assumption that the room temperature is constant and there is no significant temperature variation within the time it takes for the drain current to stabilize once we raise v_{GS}. The reduction of this

stabilization time is mostly limited by the pulser rise times and the bias tee inductance. Therefore, assuming a constant room temperature and the absence of very small thermal time constants (less than the rise times of the pulser heads), any current variations measured at the onset of the second pulse (the test pulse) cannot be attributed to any other effect than a different trapping state. Currently, state of the art pulser heads are already capable of pulse widths as small as 200 ns [132, 133], however at our lab we were limited to 1 μs widths.

Between each measurement, it is required a long waiting period, with v_{DS} and v_{GS} equal to their initial quiescent values to ensure the complete restoration of the trapping state to its initial state.

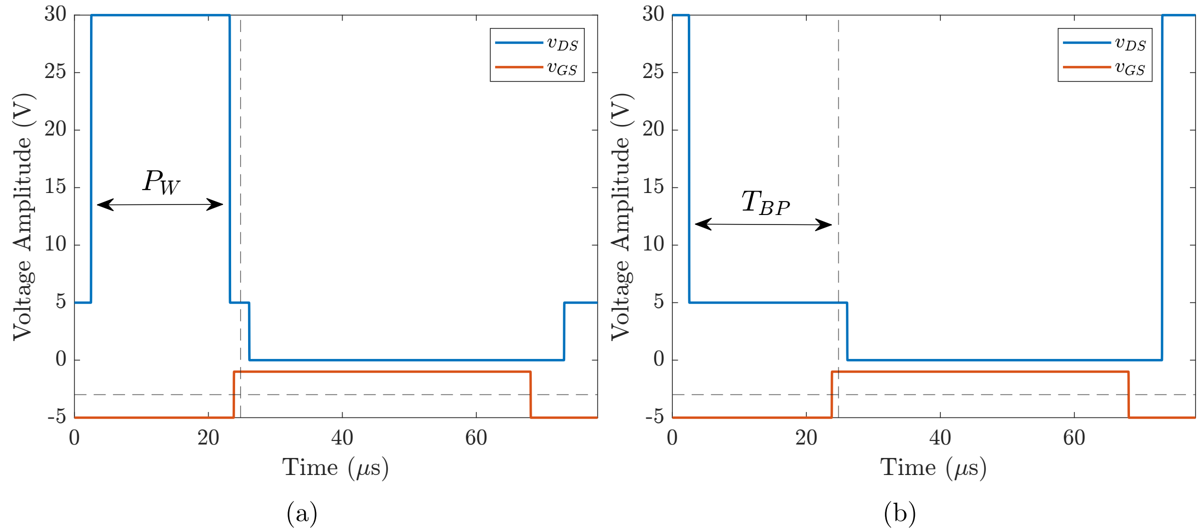

Figure 4.2: Test signals used to extract the (a) capture and the (b) emission dynamics. Note that in (a) everything is kept constant except the pre-pulse voltage amplitude, V_{Pre}, and its width, P_W. For the emission analysis, the pre-pulse width is kept constant and it is now the time between the pre-pulse end and the current measurement, T_{BP} that is varied. The horizontal dashline represents the threshold voltage. The vertical dashline represents the time instance where the drain current is measured.

Fig. 4.3 shows the measured drain current transient profiles associated to the capture and emission processes using the double-pulse technique for two different AlGaN/GaN HEMTs. The first feature of the measured $I_{DSP}(P_W, V_{Pre})$ profiles, in Fig. 4.3(a) and (c), that we would like to point out is the monotonic decrease of I_{DSP} with P_W. This means that the traps keep charging for a longer duration than what is typically assumed in the literature.

The second feature we would like to emphasize is the fact that a zero-width pre-pulse is effectively the same as applying $V_{Pre} = V_{DSQ}$. Hence, $I_{DSP}(0, V_{Pre})$ should be equal to the current level of the uppermost curve ($V_{DSQ} = 5$ V) (see that this profile is constant for all P_W), regardless of V_{Pre}. So, although we are constrained to $P_W > 1$ μs due the rise times of our pulser heads, we can still see a clear manifestation of the extremely fast capture transients (< 1 μs), which are increasingly more pronounced with higher V_{Pre} values.

The third feature to point out is the influence of the pre-pulse amplitude on the amount of current collapse observed. Higher amplitudes result in significantly larger variations of I_{DSP}. This effect can be understood as the result of more charge trapping, as a consequence of larger potential gradients.

Finally, Fig. 4.3(b) and (d) shows the measured current transients when the emission dominates, i.e. for a varying time interval between the end of the pre-pulse and the test pulse measurement, for various pre-pulse amplitudes, $I_{DSP}(T_{BP}, V_{Pre})$. Note how the beginning of each recovery transients starts at the same current level as the one achieved during the capture characterization for the widest pre-pulse width, an indication that steady-state has been reached.

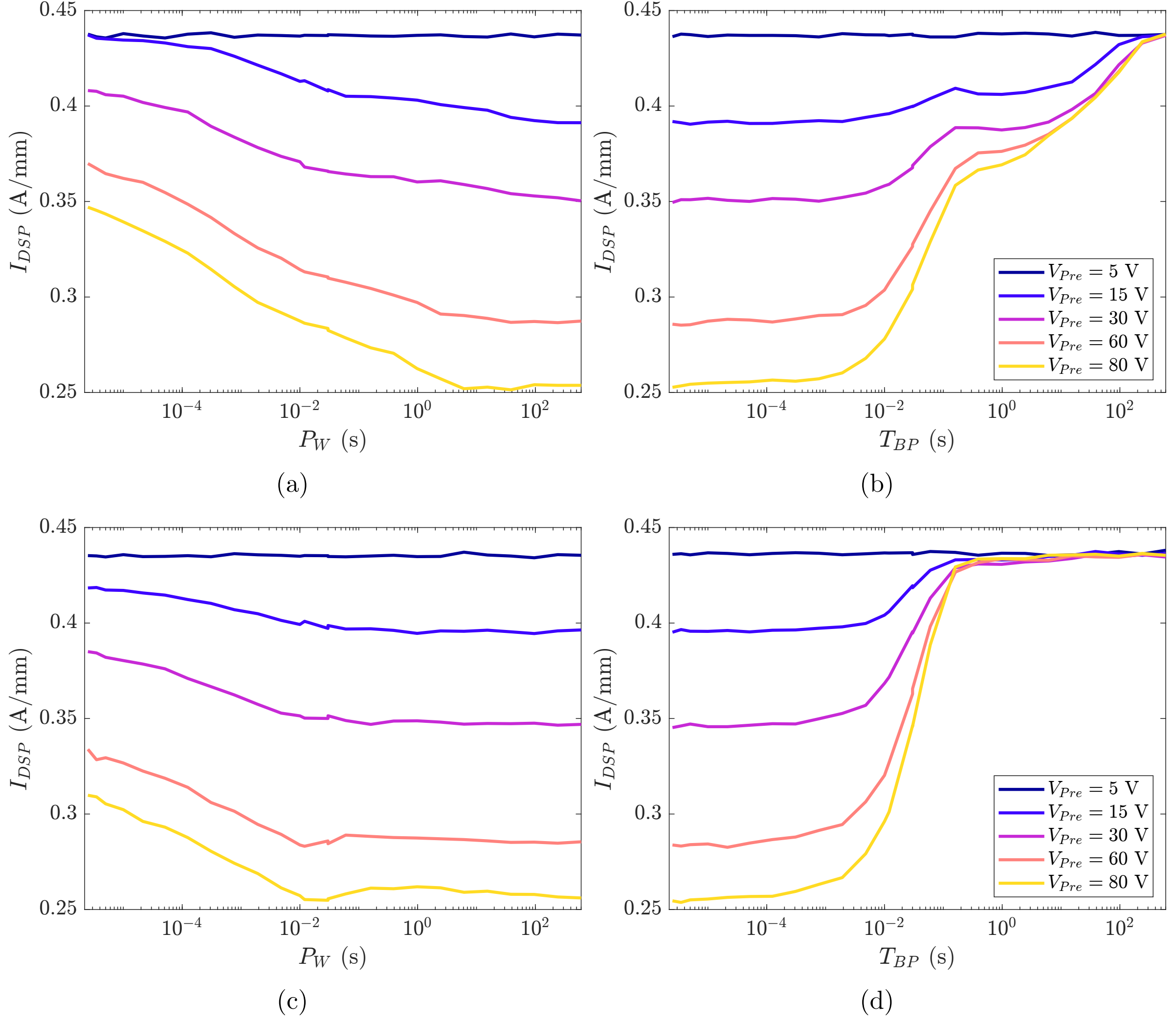

Figure 4.3: Measured profiles of two different AlGaN/GaN HEMTs for various pre-pulse amplitudes, V_{Pre}. (a) and (c) sweep of the pre-pulse width, P_W; (b) and (d) sweep of the time between the pre-pulse end and the measurement pulse, T_{BP}.

4.1.1 Deembedding the Static Nonlinearity

The dependence of i_{DS} on v_{trap}, although monotonic, is nonlinear, which affects our perception of the trapping time constants. From a PA design perspective, this issue is not so relevant since the concern is mostly directed to the dynamics manifested through the drain current. However, for a proper extraction of the SRH model, either for the purpose of

identifying the traps' nature from the Arrhenius plot or to accurately implement a physically supported model, the static nonlinearity between i_{DS} and v_{trap} should be deembedded.

Suppose our static current model is implemented as $I_{DS}(V_{DS}, V_{GS}, V_{Ctr}, T)$ where V_{Ctr} corresponds to the steady-state trapping state imposed by V_{DS}. For the purpose of this demonstration we will define

$$V_{Ctr} = V_{DSQ} \tag{4.1}$$

Naturally, (4.1) is a very crude approximation of the steady-state trapping state derived from the SRH model, (3.13). Nevertheless, for small V_{DSQ}, (3.13) becomes approximately linearly dependent on V_{DSQ}. For higher V_{DSQ} values, the trapping state should saturate (there is only a fixed number of available trap centers), but this can be easily emulated by an hyperbolic tangent (see first equation in (4.2)). The goal of this approximation is to substitute the implicit function, (3.13), by an explicit one.

The adopted constitutive relation for i_{DS} can be understood as a parametric function of the instantaneous values of v_{GS} and v_{DS} [134],

$$\begin{aligned}
V_{T0_{var}}(v_{Ctr}, T) &= V_{T0} + \frac{A_{VT}}{2}\left[\tanh(K_{VT}(v_{Ctr} - V_{VT})) + 1\right] - V_{TH}T \\
\alpha_{var}(v_{Ctr}, T) &= \alpha_0 + \frac{A_\alpha}{2}\left[\tanh(K_\alpha(v_{Ctr} - V_\alpha)) + 1\right] - \alpha_{TH}T \\
\beta_{var}(v_{Ctr}, T) &= \beta_0 + \frac{A_\beta}{2}\left[\tanh(K_\beta(v_{Ctr} - V_\beta)) + 1\right] - \beta_{TH}T \\
V_{T_{eff}}(v_{DS}, v_{Ctr}, T) &= V_{T0_{var}} - a_{VT}\tanh(K_{VT}v_{DS}) \\
V_{GS1}(v_{GS}, v_{DS}, v_{Ctr}, T) &= v_{GS} - V_{T_{eff}} \\
V_{GS2}(v_{GS}, v_{DS}, v_{Ctr}, T) &= V_{GS1} - \frac{1}{2}\left(V_{GS1} + \sqrt{(V_{GS1} - V_K)^2 + \Delta^2} - \sqrt{V_K^2 + \Delta^2}\right) \\
V_{GS3}(v_{GS}, v_{DS}, v_{Ctr}, T) &= V_{ST}\ln\left(1 + e^{\frac{V_{GS2}}{V_{ST}}}\right) \\
F_{GS}(v_{GS}, v_{DS}, v_{Ctr}, T) &= \frac{V_{GS3}^2}{1 + \frac{V_{GS3}^{plin}}{V_L}} \\
F_{DS}(v_{GS}, v_{DS}, v_{Ctr}, T) &= (1 + \lambda v_{DS})\tanh\left(\alpha_{var}\frac{v_{DS}}{V_{GS3}^{psat}}\right) \\
i_{DS}(v_{GS}, v_{DS}, v_{Ctr}, T) &= \beta_{var}F_{GS}F_{DS}
\end{aligned} \tag{4.2}$$

where all coefficients are kept constant for different trapping states, except the parameters that impact the effective threshold voltage, $V_{T0_{var}}$, the knee voltage, α_{var}, and the voltage gain, β_{var} which are all functions of v_{Ctr} and T. Thus, for each trapping state, imposed by the pre-pulse amplitude, V_{Pre}, the $i_{DS}(\cdot)$ function is static but with different $V_{T0_{var}}$, α_{var} and β_{var} values. Note that, besides what we defended in Chapter 3, our experience with these devices have shown us that fine tuning the knee voltage and voltage gain contribute to a better overall fitting to the measured drain current. The physical reason why this happens remains an open problem.

Using the double pulse technique with large pre-pulse widths, we measured isodynamic I-V data for different pre-pulse amplitudes, obtaining different sets of static I-V curves parameterized by V_{Ctr}.The utility of this is that we can then numerically invert the $i_{DS}(\cdot)$ function and find the respective equivalent v_{Ctr} throughout the entire current transients. With this we are avoiding any corruption of the extracted time constant due to the nonlinear relationship between i_{DS} and v_{Ctr}. Fig. 4.4 illustrates this process by showing both the measured capture and emission transients from the drain current perspective (Fig. 4.4(a) and (b)) and the corresponding trapping state after a numerical inversion (Fig. 4.4(c) and (d)).

Note how in Fig. 4.4(d), we clearly see the trapping state change from its quiescent state, fixed at $V_{DSQ} = 90$ V, down to the measurement bias $V_{DSP} = 28$ V. The reason why all the recovery curves do not exactly overlap at 28V for large T_{BP}, as they should, is because we only measured the static response at $V_{DSQ} = 28$ V for $T = 20°$C. To guarantee a more complete and consistent extraction of our model parameters, we should have measures the complete HEMT's I-V characteristics for various pre-pulse amplitudes for each temperature. Unfortunately, the amount of time required to obtain a full set of measurements ends up becoming to big for a community laboratory.

4.1.2 The Double Pulse Technique as an I-DLTS Tool

Deep-Level Transient Spectroscopy (DLTS) has been used extensively to characterize the electronic features of defects in semiconductors with activation energies up to ~ 1 eV [135]. It does that by measuring the emission time constant from either capacitance (C-DLTS) or current transients (I-DLTS) at different temperatures, which according to the Arrhenius equation can then be used to extract the trap's fingerprints. The results obtained in Fig. 4.4(d), specifically the dominant emission time constants, are thus extremely useful to find more about the trap's nature, as shown in Fig. 4.5.

The results of Fig. 4.5 highlight three very important points:(i) the error produced by the linearization is practically negligible, which validates the temperature dependence derived from the SRH model; (ii) the resulting activation energy is compatible to what is typically associated to Fe-doped buffers [40]; (iii) because of point (ii) and our *a priori* knowledge of a Fe-doped buffer layer in these devices, then these results are in line with the current explanation for drain-lag, i.e. memory effects induced by buffer traps.

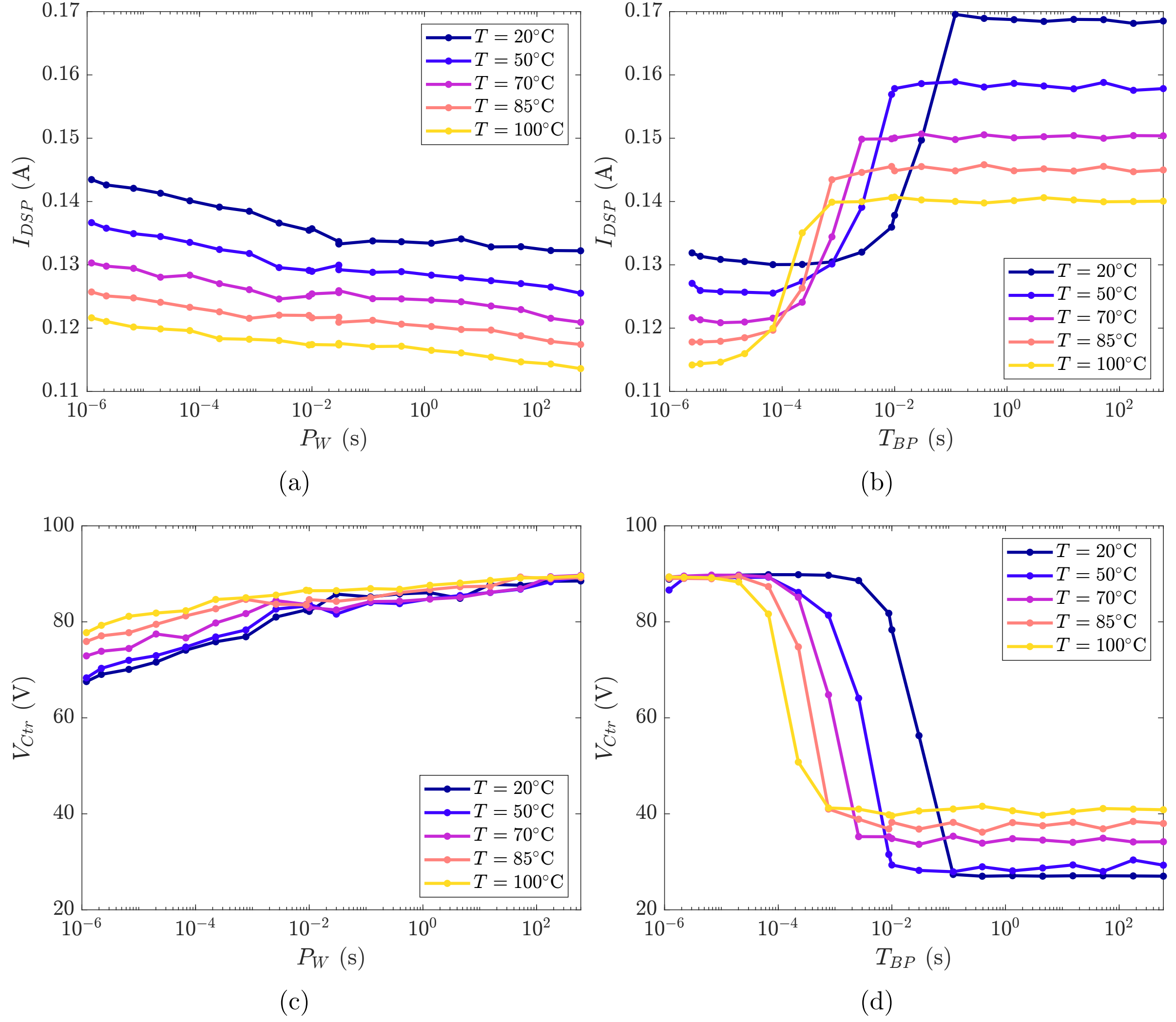

Figure 4.4: (a) Capture and (b) emission current transients measured at different temperatures with $V_{Pre} = 90$ V and measured at $V_{DSP} = 28$ V. (c) and (d) correspond to the trapping state after an numerical inversion using (4.2).

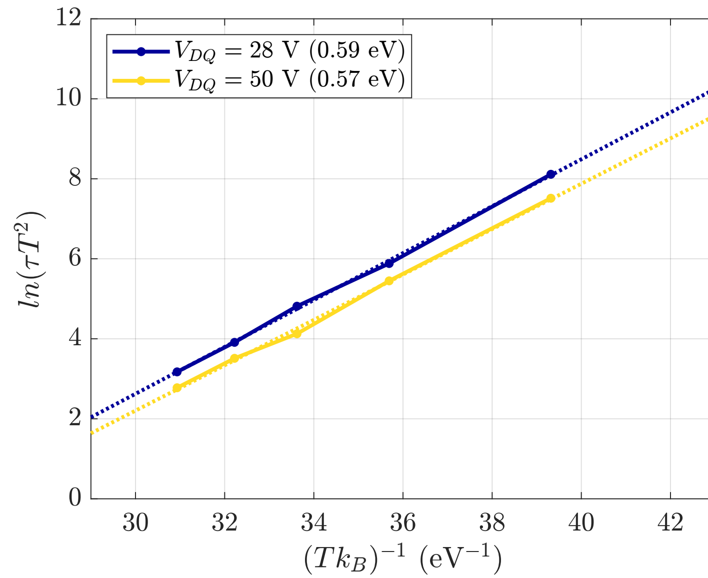

Figure 4.5: Arrhenius plots drawn from the results of Fig. 4.4(d) for two different measurement biases. Note that the trap's cross-section should be extracted from the y-intercept however there is a bias dependence that remains to be addressed.

Chapter 5

Impact of Deep-Level Traps on the Linearizability

Trapping and electrothermal effects constitute the main reason for long-term memory. Previous reports on Si-LDMOS-based PAs demonstrated that temperature fluctuations only showed repercussions on narrow-band signals; this is because of their large thermal time constants, owing to their low thermal conductivity. With low thermal conductivity, the temperature is unable to track the fast variations of wider band signals and, therefore, remains closer to its average value. The PA behaves as static within the signal time (or the predistorter update time), and so the device's temperature variations produce little to no impact on the linearizability [24, 70]. GaN HEMTs, on the other hand, are a challenge in terms of linearizability for modern signals, not only because of their higher thermal conductivity, but most importantly because they depend on the introduction of traps to properly operate [136].

More recent alternatives have managed to advance on this problem by taking advantage of the physical knowledge of the phenomenon at the transistor level and extrapolate it to the system level. The authors of [42] proposed a DPD structure that consists of the typical GMP model whose parameters are controlled by two auxiliary physics-based models implemented as Infinite Impulse Response (IIR) filters. These are the Jardel model [116] and the typical RC electrothermal model interpretation of self-heating to emulate, respectively, the trapping and electrothermal effects. With this novel approach, they were able to successfully compensate the long-term memory to levels that meet the stringent constraints of multi-carrier signals in the global system for mobile communications. In [44], the authors took a step further and developed a hybrid analog/digital linearization scheme, where the DPD load is relieved by ensuring the long-term memory compensation through an analog circuit that mimics a variable time constant that is added to the V_{GS} bias. The purpose was to accommodate the stretched behavior often seen in the detrapping transient profile of GaN HEMTs. This comes as an improvement to a previous work of them where they relied on a fixed time constant [43]. So, not only did they show that it is possible to reduce the operational cost of complex predistortion models such as [42], but they reinforced the notion that a better understanding of the physical phenomena improves the linearization.

Fig. 5.1 shows an example, taken from [43], in which the measured AM/AM and AM/PM of a GaN HEMT-based PA subjected to a 4-carriers Global System for Mobile Communications (GSM) modulated signal were obtained (i) without any nonlinear compensation (green dots), (ii) with a DPD linearizer conceived for short-term memory correction only (black dots)

and (iii) with the same DPD, but now assisted by an analog long-term memory compensation circuit (ACC) (yellow dots). Note the [linear] constant gain and phase as well as a reduction of the dispersion of points (reduction of hysteresis) when the PA nonlinear memory is corrected.

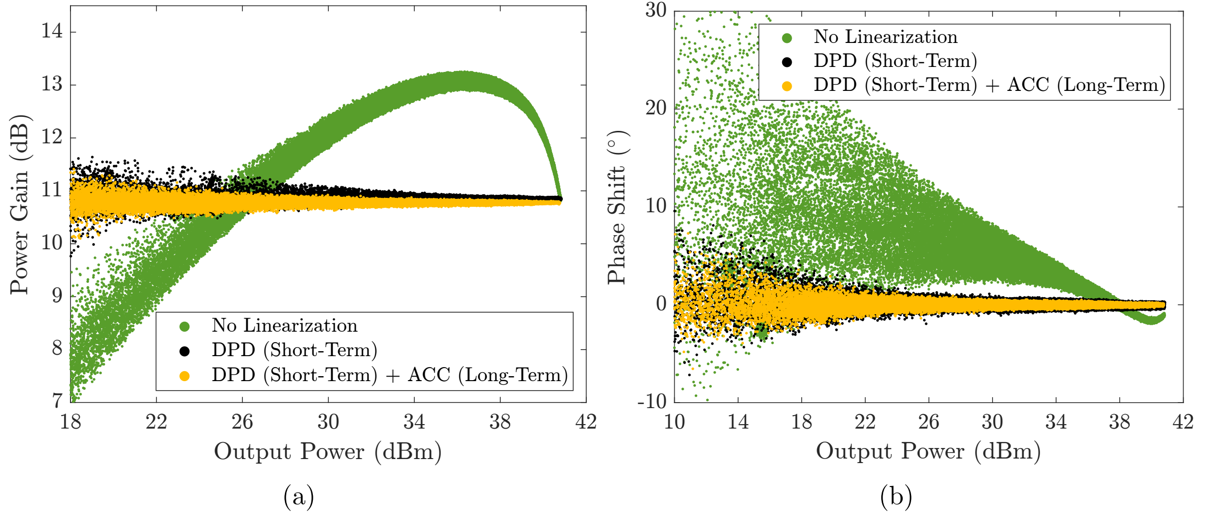

Figure 5.1: Hysteretic (a) AM/AM and (b) AM/PM characteristics of a GaN HEMT-based PA subjected to a 4-carriers GSM modulated signal. ACC stands for analog [long-term memory] compensation circuit.

In this regard, it is worth noting a recent work [137], in which the physical link between the deep-level traps characteristics and the linearizability of a GaN HEMT-based PA is explored. There, the authors assess the impact of the concentration and activation energy of the traps on the Adjacent Channel Power Ratio (ACPR) for a Frequency Division Multiplexing (FDD) and a Time Division Multiplexing (TDD) signal, after using DPD to minimize the static nonlinearities. Signals whose envelopes vary on time scales closer to the trap's emission rates, for the PA operating temperature, are shown to be less linearizable. The explanation provided is that the envelop signal modulates the concentration of trapped charge, which in turn changes the transistor's threshold voltage. Indeed, this view matches with the explanation for the soft-compression observed in GaN HEMT based PAs reported on [138]. The instabilities caused to the dc operating point of the PA will consequently affect its linearity. This work is very much in line with what we wish to accomplish in this thesis, and so it comes as an important contribution to our work. In this chapter, we intend to deepen this correlation between the trapping time constants and the performance of the PA, as well as the impact of the thermal time constants. The coupling between the PA self-heating and the trapping kinetics, as far as we know, remains a poorly explored topic in the linearization field. Yet, it is well known that the trapping time constants are deeply dependent on the device temperature. So, here, we try to provide a meaningful contribution to this subject. Ultimately, this work may prove useful to improve future DPD schemes and help guide certain device characteristics at the manufacturer's level to attain transistors with higher linearizability.

5.1 Long-Term Memory in DPD Linearizability - Thermal and Trapping Effects

As known, the trapping state is normally imposed by the drain peak voltage [116, 127]. In practical PAs these voltage peaks are at least two times higher than V_{DD}, resulting in a significant unwanted gain variation. Earlier works [8, 43, 127] have shown that, in operation, the long-term behavior of a PA can be tracked by simplified models using only the dominant time constant of the phenomena. Accurate estimation of these dominant time constants thus plays an important role on the PA linearization. Moreover, their impact is dependent on certain temporal characteristics of the signals. For instance, if it is TDD or FDD, due to the different excitation of the device. However, it is unclear how different time constants will reflect on the PA linearity after DPD, and/or what is the worst-case scenario.

To study how the magnitude of the time constants impact the PA linearizability, we designed a PA centered at 2.5 GHz with 200 MHz bandwidth using ideal lumped elements. We used an AlGaN/GaN HEMT model where we can modify the thermal and trapping dynamic behaviors for these specific tests. The static impact of both thermal and trapping effects was extracted from static isothermal I-V measurements of an AlGaN/GaN HEMT under different ambient temperatures and quiescent biases, respectively, following the double-pulse procedure [46, 130]. We have also taken into account the PA's instantaneous bandwidth to reduce the memory introduced by the bias network. The tested PA performance is illustrated by its Continuous Wave (CW) characteristics, the simulated load-line for the center frequency on top of the pulsed IV curves (for $V_{DQ} = 90$V) and the impedance profile over frequency in Fig. 5.2. As expected and mentioned above, the drain voltage excursion exceeds twice the V_{DD} bias voltage (Fig. 5.2(b)).

5.1.1 Trapping Time Constants Impact on PA Linearizability

Trapping effects are a consequence of a built-in voltage caused by the accumulation of charge. So, they are typically modeled as a trapping control voltage, v_{trap}, formed at a capacitor's terminals. Here, we account only for drain lag, which is representative of most commercial GaN HEMTs' technology. Thus, the control voltage, v_{trap}, changes with the applied drain voltage, v_{DS}, which, in turn, is controlled by the input signal. Though distorted, the envelope of the v_{DS} mostly preserves the same signal dynamics as the PA's RF input signal. As a simplification, the trapping dynamics are modeled according to the Jardel model [116], shown in Fig. 5.3(a), where the diode is considered ideal. Please note that the important features derived from the SRH model (that were not present in the original Jardel model), namely the emission time constant dependence with temperature, will be incorporated in this model's version. The voltage at the capacitor's terminals, v_{trap}, acts as our state variable. This voltage will then control the transistor's characteristics, according to the static measurements. This is mainly a threshold voltage shift, resulting in the so-called back-gate effect [139]. Since the diode is ideal, the Jardel model is a switched model, where we either charge or discharge the capacitor through two linear systems, depending on whether v_{DS} is higher or lower than v_{trap}, respectively [46,116,127]. Thus, in the Jardel model we simply set the capture (charge), τ_c, and emission (discharge), τ_e, time constants. Please note that the incorporation of the SRH model would likely improve the accuracy of our PA model but would also increase its complexity and, consequently, degrade our ability to extract insight from the simulations.

Fig. 5.4(a) shows an envelope simulation of the PA steady-state response under a two-

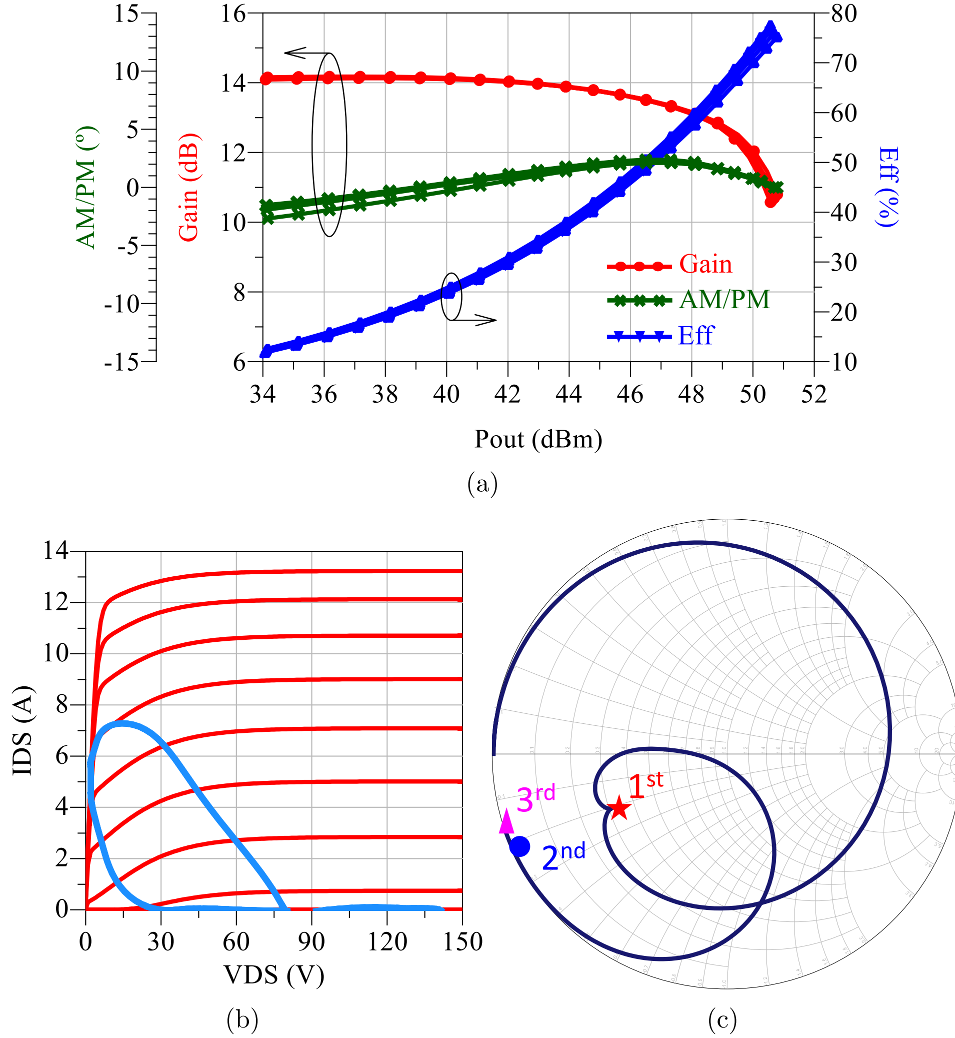

Figure 5.2: (a) Simulated CW gain, efficiency, and AM/PM response of the designed PA. Each curve corresponds to a different center frequency from 2.4 GHz to 2.6 GHz with a 50 MHz step; (b) the simulated load-line at the current source plane, with the bias point $[I_{DS}, V_{DS}, V_{GS}] = [100\,\text{mA}, 50\,\text{V}, -2.7\,\text{V}]$, and for the center frequency (2.5 GHZ) on top of the pulsed I-V curves (for $V_{DQ} = 90$V); and (c) the impedance profile over frequency with the fundamental and harmonic impedances of the center frequency (2.5 GHz) marked.

---

tone signal excitation with the electrothermal model disabled. In this test, the considered trapping model has a fixed capture time constant, τ_c, equal to 10 ns and different emission time constants, τ_e, from 50 ns to 1 ms.

For the remaining of this work, the complex behavior of the capture time constant predicted by SRH will be simplified to a very small and fixed value. Pulsed IV measurements show that most of the capture indeed happens much below the μs scale, for large v_{DS} swings, with only a small portion extending for longer time constants (around ms) [46] (see Fig. 4.3). However, for the typical communication signals, these slow transients are not excited, as this would require an unlikely succession of closely packed very high peaks for a long time. The dominant capture time constant can then be safely assumed to be lower than a few ns. Fur-

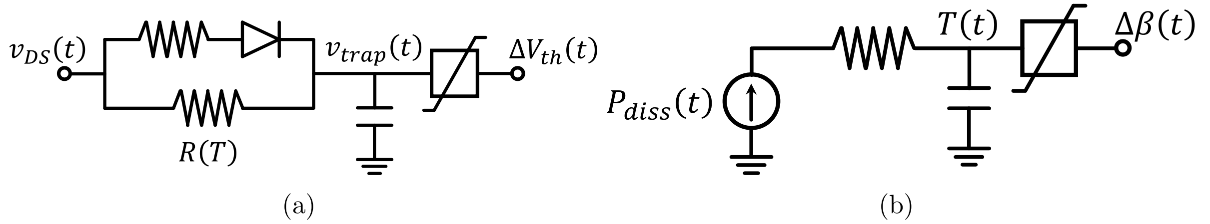

Figure 5.3: Equivalent circuits that represent the dynamics associated with (a) trapping effects and (b) electrothermal effects, and their respective main impact on the transistor performance. ΔV_{th} and $\Delta\beta$ stand, respectively, for a shift of the threshold voltage [46, 127] and transistor's current gain [140]. The squares crossed by a broken line, represent a nonlinear mapping between the physical variables (the trap control voltage and the temperature) and the dc-IV model parameters in our formulation, $i_{DS} = f(v_{GS}, v_{DS}, v_{trap}, T)$.

---

thermore, it has been demonstrated that DPD techniques supported by an auxiliary trapping model with only a fixed capture time constant are capable of good linearity metrics [8, 53]. All these suggests that the capture transient likely does not play a role as important as the emission dynamics for the PA linearizability.

The emission time constant is always considered higher than the capture one and, so, the trapping circuit rectifies the signal, operating as a peak or envelope detector. For low τ_e values, v_{trap} changes at the same rate of the envelope signal because both the emission and capture are faster than the envelope rate. In this condition, the trapping state is mostly dependent on the instantaneous envelope amplitude, which results in very little memory depth. Therefore, we see almost no hysteresis behavior when $\tau_e = 50$ ns in Fig. 5.4(a). In the other extreme case, when the emission is much slower than the envelope rate ($\tau_e = 1$ ms), each peak of the signal charges the capacitor, and virtually nothing gets discharged before the next peak. The capacitor thus remains fully charged once it reaches steady-state. In this scenario, there is also no memory manifestation because the transistor maintains the same static characteristics and, again, we do not observe any hysteresis behavior in Fig. 5.4(a).

It is in the intermediate cases, where the emission is slow enough not to be completely correlated with the envelope signal, but fast enough to generate significant v_{trap} excursion, that the trapping control voltage changes substantially when the envelope increases or decreases. This will then generate a fluctuation of the PA gain along the signal envelope, which results in the large hysteresis plotted in Fig. 5.4(a).

In the cases where minor hysteresis is observed, conventional DPD can compensate the PA as long as the memory span is sufficient to tackle the residual memory. The problem happens when a large hysteresis is observed, which corresponds to a significant shift of the PA nonlinear behavior along time, according to its dependence on the trapping state, creating the nonlinear long-term memory that is so detrimental for linearizability. Therefore, we can already glimpse the fundamental role that the trap emission time constant of GaN HEMT devices will have on the linearizability of the PAs they integrate.

To quantify the impact of the emission time constant on the linearizability, we considered two standard Long-Term Evolution (LTE) signals, with different bandwidths (2 MHz and 0.2 MHz) and equal PAPR (7.5 dB). Fig. 5.5(a) illustrates the gain dispersion obtained by the PA envelope simulation when excited with the 2 MHz signal. The simulated trapping control voltage responses for different time constants are shown in Fig. 5.5(b) for this signal.

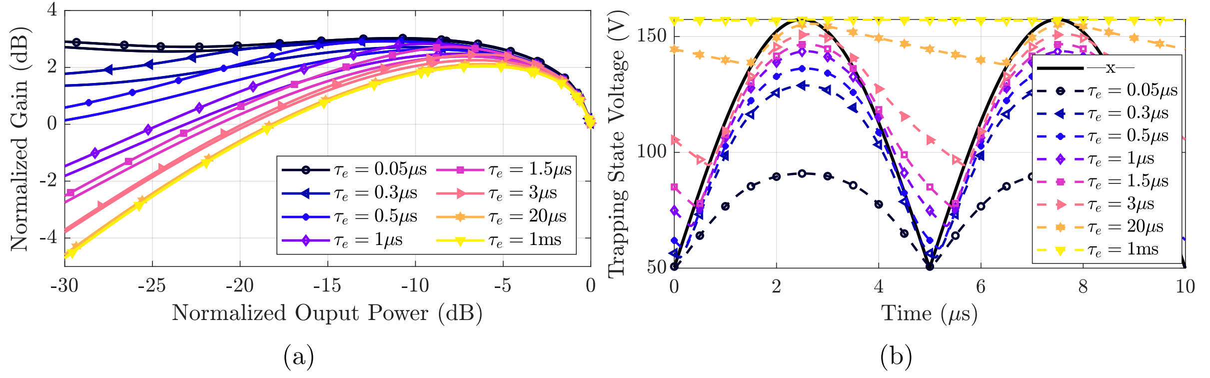

Figure 5.4: Simulated (a) PA response under a two-tone excitation (for 200 kHz of frequency separation, Δf), considering a fixed capture time constant, τ_c, equal to 0.1 μs and different emission time constants, τ_e, and (b) the respective trapping control voltages on top of the two-tone envelope signal. No thermal effects were considered.

Please note that, for the 0.2 MHz signal we would observe the same behavior, but with the time scales (and time-constants) scaled up by 10. Similarly to what happens in the two-tone signal, there are intermediate emission time constants where the discharge behavior of the trapping control voltage is in a time scale that is not caught by the DPD, but is fast enough to considerably vary throughout the signal.

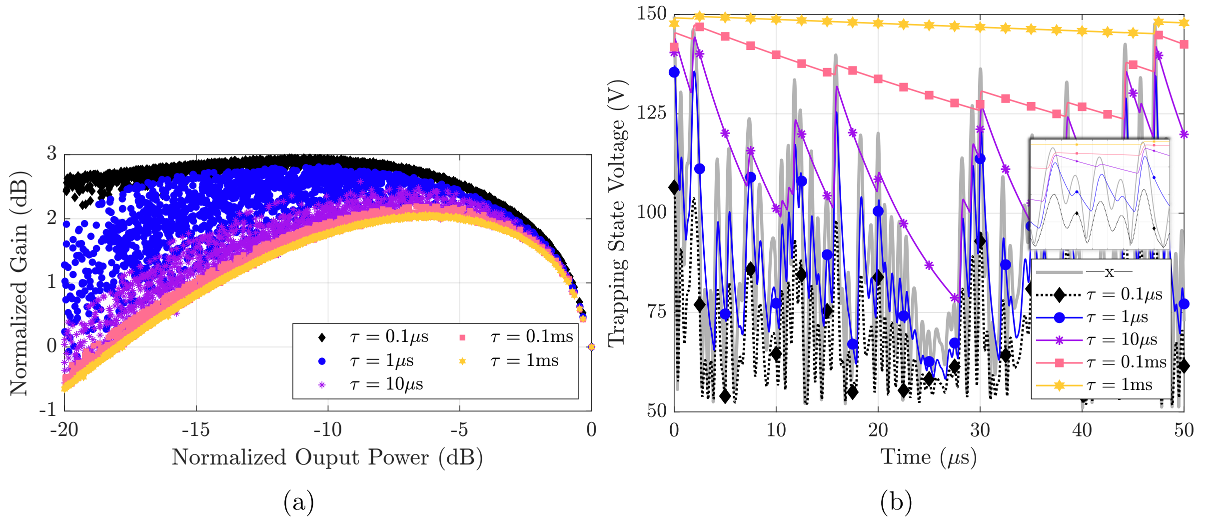

Figure 5.5: Simulated (a) PA response for a LTE signal with 2 MHz bandwidth and (b) the respective signal and trapping control voltage response when different trapping emission time constants are considered. The inset in (b) is a simple magnification of the peaks in the final portion of the signal.

It is interesting to note that, as we move into higher emission time constants the PA moves from a shallow class B (with a small τ_e) to an evident "class-C gain characteristic" (with a large τ_e) as shown in Fig. 5.5(a). As this static nonlinearity is more pronounced, it would require a higher polynomial order DPD to reach the same ACPR level.

We then run a simple DPD, using envelope simulation, based on a Memory Polynomial

(MP) with order 11, sufficient to compensate the static nonlinearity of this PA, and a memory span of 4 samples. Please note that our idealized PA was designed to have the gain (AM/AM) and phase-shift (AM/PM) characteristics very confined in frequency and special care was taken to avoid bias network induced memory effects. It is thus expected that a simple DPD should be enough to compensate the PA in the absence of long-term memory effects. Fig. 5.6 shows the achieved linearity metric (ACPR) versus the emission time constant.

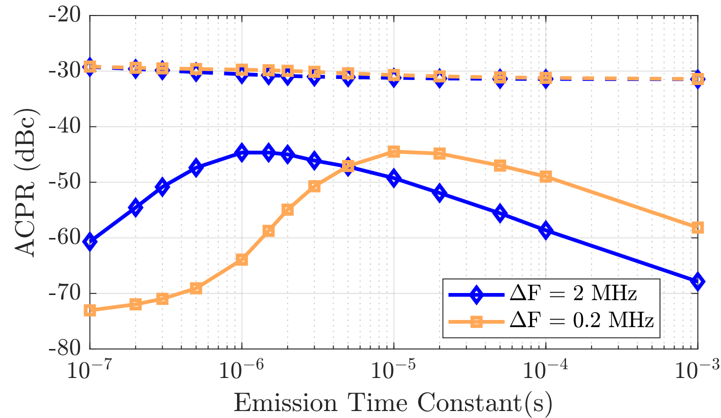

Figure 5.6: Simulated ACPR levels before (dashed lines) and after (solid lines) DPD versus the trapping emission time constants for two different signal bandwidths.

As can be seen, the worst ACPR level for the signal with 2 MHz bandwidth happens when $\tau_e \approx 1\mu s$. This worst-case scenario corresponds to the PA gain profile with the widest hysteresis as depicted in Fig. 5.5(a).

This worst-case happens when the emission time constant equals the average time between consecutive high amplitude peaks (in this case, peaks that are above 50% of the maximum envelope amplitude). This 50% amplitude threshold was empirically found as the best for the LTE signals considered in this work. We have done it for different realizations of signals of this type and this process has offered a consistent estimation. Fig. 5.7(a) illustrates the obtained "peaks signal" for the 2 MHz signal considering the 50% amplitude threshold, and in Fig. 5.7(b) we have the respective histogram and the average time between consecutive peaks.

Therefore, this method help us estimate the emission time constant that will most impact the linearizability for a particular signal. In this example, most peaks are spaced between 0.5 and 2.5 μs (see Fig. 5.7(b)). Naturally, for the 0.2 MHz signal, the time between peaks will increase, which pushes the worst case scenario to a ten times higher emission time constant (Fig. 5.6).

Please note that, if we consider the time between two maximum amplitude peaks as suggested in [141], the average time would be overestimated (for our 2MHz signal we would get higher than 50 μs instead of the 2 μs).

5.1.2 Thermal Time Constants Impact on PA Linearizability

Thermal effects are excited by the instantaneous power dissipation, and their dynamics are guided by a linear process of heat flow that affects the current gain [140], β, as shown in Fig. 5.3(b). For the purpose of this analysis, we can simplify the filtering to a single dominating

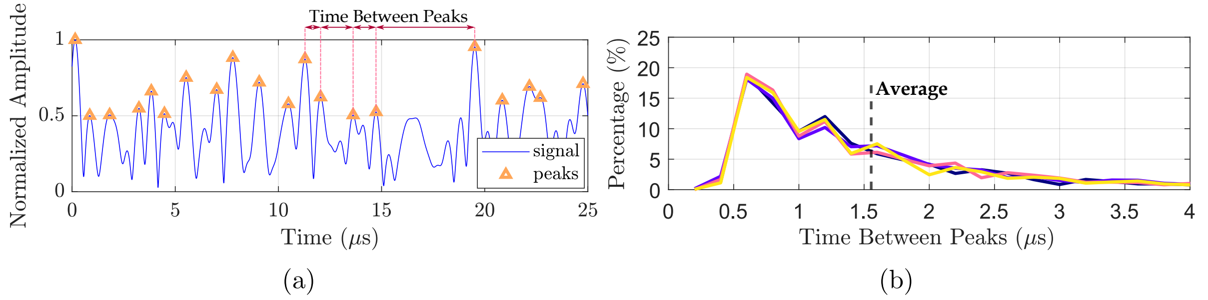

Figure 5.7: (a) Example of a 2 MHz LTE signal with all peaks above 50% of the maximum signal amplitude highlighted and (b) the histogram of the time between peaks for different realizations of this signal type.

---

time-constant. Generally, the remaining time constants are either much slower than the signal dynamics, or the associated temperature variation is too small to be noticeable.

Fig. 5.8(a) shows the PA response under the same previous two-tone excitation when different thermal time constants are considered, and the trapping model is deactivated. For very small thermal time constants, the temperature varies at the same rate of the instantaneous power dissipation. With very large time constants, the temperature stabilizes to a value imposed by the product of the average power dissipation and the equivalent thermal resistance [see Fig. 5.8(b)]. In both of these cases, we see no hysteresis in Fig. 5.8(a). Memory manifests when we move to the intermediate time constants, which can be explained exactly by the same reasoning as before.

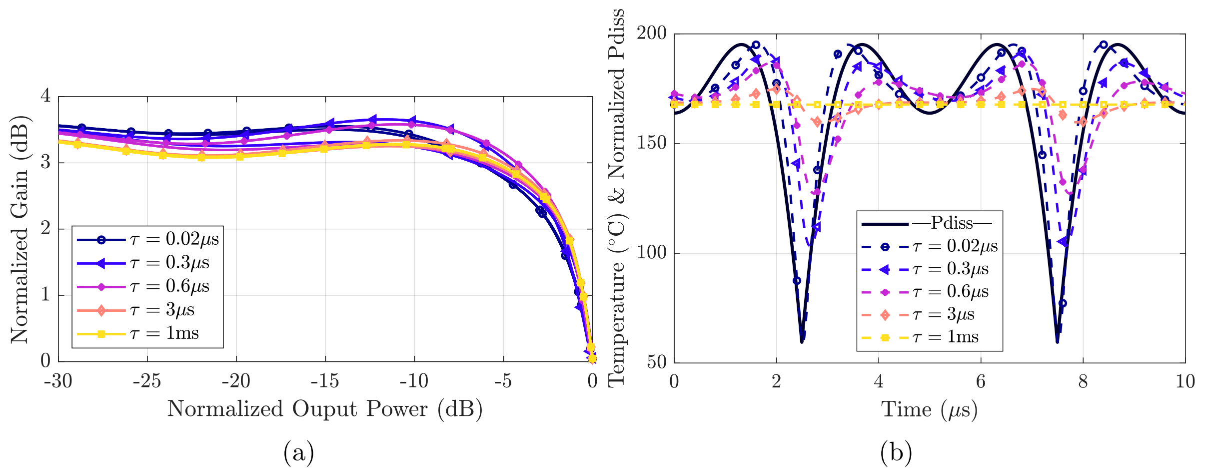

Figure 5.8: Simulated (a) PA response under a two-tone excitation (for 200 kHz of frequency separation, Δf), considering different thermal time constants and, (b), the respective normalized temperature variation on top of the normalized instantaneous power dissipation. No trapping effects were considered.

To quantify the impact of the thermal time constants on the linearizability, we have also run DPD, again relying on envelope simulation, on the same PA with the same LTE signal, but now considering only the electrothermal effects. The obtained linearity metric is shown in Fig. 5.9. For the considered signal bandwidths, when we compare the influence of thermal

and trapping, we can see the worst case scenario around −53 dB (Fig. 5.9) and −45 dB (Fig. 5.6), respectively. Naturally, this comparison is based on the thermal and trapping models extracted for this particular device, however this is already suggestive that trapping will have a stronger impact on the linearizability than self-heating. Nevertheless, the worst thermal-induced ACPR levels occur for time constants, which besides being smaller than of trapping effects, are not what we usually observe in practice. Self-heating tends to happen at lower rates, which indicate that thermal effects are particularly nefarious for much smaller bandwidths than the ones selected for this test.

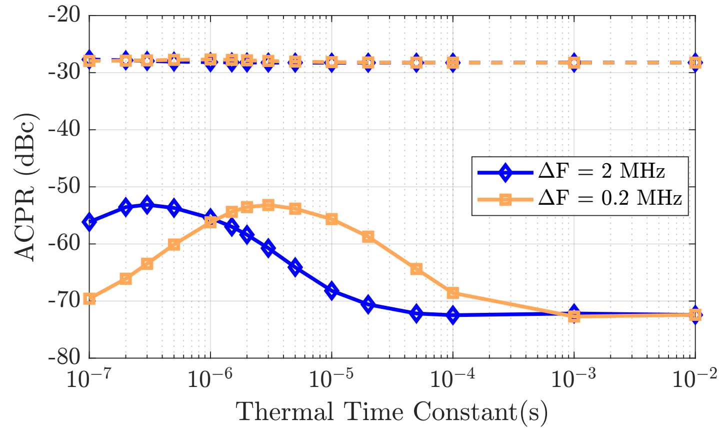

Figure 5.9: Simulated ACPR levels before (dashed lines) and after (solid lines) DPD versus the thermal time constants for two different signal bandwidths.

5.2 Trapping and Thermal-Dependent Long-Term Memory Effects

In the previous section, we have shown how trapping and thermal effects independently impact the PA linearizability when considered separately. However, in a real device we always get a mixture of the two. Moreover, trapping effects are known to be highly dependent on the temperature, which is continuously changing as the PA operates under a modulated signal excitation.

5.2.1 Device Characterization

According to (3.6), by knowing A and the trap's activation energy we know how the emission time constant changes with temperature. To illustrate the importance of the thermal-trapping coupling, we compared two devices with similar nominal structure (i.e., same materials, stacking, spatial dimensions, and doping), but using different processing conditions. We performed Current Deep-Level Transient Spectroscopy (I-DLTS) using the double-pulse methodology, as described in Chapter 4, to characterize the recovery profiles for various temperature. Fig. 5.10 gives the obtained recovery profiles measured at 50 V after applying a 90 V pre-pulse for 200 s. The horizontal scale represents the time elapsed between the pre-pulse end and the beginning of the measurement.

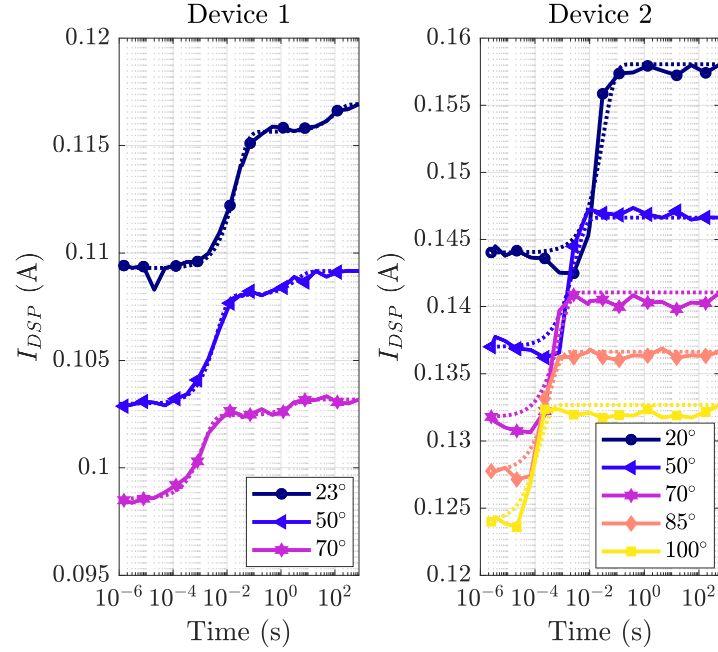

Figure 5.10: Measured drain current recovery from a pre-pulse of 90V to 50V for several different temperatures.

From these recovery profiles, the dominant emission time constant is extracted and used to build the Arrhenius plot shown in Fig. 5.11. As you can see, these devices have similar activation energies that differ only by approximately 0.1 eV but very different apparent cross-sections. More importantly, their emission time constants are expected to get substantially different from one another as we move towards higher temperatures.

Bias-dependent effects that could alter the apparent emission time constant, like the Poole-Frenkel effect, are most likely absent in Fe-doped buffers [115]. Therefore, we restricted our characterization to just one bias.

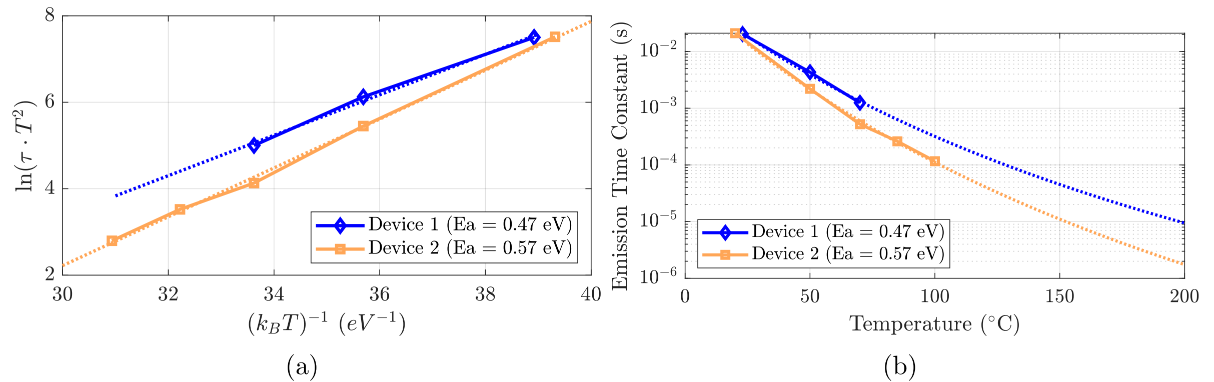

Figure 5.11: (a) Arrhenius plots drawn from the results of Fig. 5.10 and (b) the resulting emission time constant versus temperature.

The trapping characterization was performed on small unpackaged transistors, and for each we have a high-power device with a 16 mm gate periphery that will be used to perform

the PA measurements. As we previously mentioned, as long as the capture time constant is very small, its impact on the device's linearizability will be very small, so we will use the simplified SRH model with a fixed capture time constant and an emission time constant dependent on the device temperature according to (3.6).

The thermal model was extracted from a Multiphysics simulation of one of the 16 mm packaged devices (with the fixture in which we will mount the PA already accounted for). Since both devices share the same structure, the thermal model is assumed equal. Fig. 5.12 shows the temperature variation at the device's junction, package, and case over time, when a step of power dissipation equal to 57 W and room temperature of 46°C are considered.

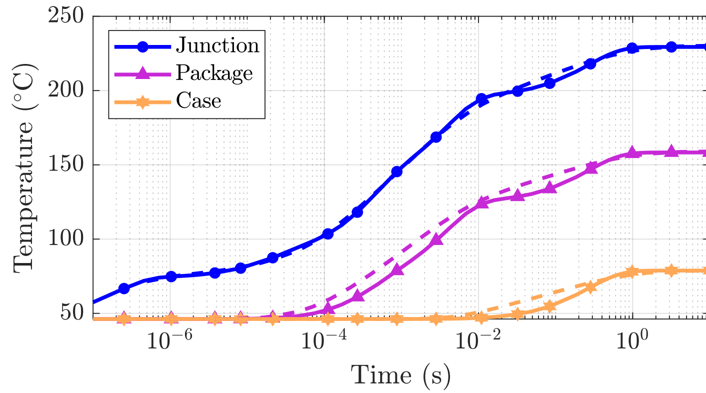

Figure 5.12: Simulated temperature variation of the device's junction, package and case over time, when a constant power dissipation equal to 57 W is considered, and for a room temperature of 46°C. The solid lines are from a Multiphysics simulation and the dashed lines are the response of the extracted multi-RC network.

5.2.2 Impact on Linearizability

After characterizing the trapping and thermal effects in both devices, we extracted the respective model parameters and implemented it in our PA model. We then compared the performance of both devices after DPD using a 2 MHz LTE signal with a PAPR of 7.5 dB, under five different scenarios:

1. no long-term memory effects are considered, this scenario will serve as a reference;
2. only thermal effects are activated (using the extracted model for both devices);
3. only trapping effects are activated with the emission time constant at room temperature;
4. only trapping effects are activated with the emission time constant at 155°C, which is the average temperature in scenario 5;
5. both thermal and trapping models are activated.

Table 5.1 compares the linearity of both devices, in the above scenarios, after running DPD in envelope simulation, considering again a memory polynomial with order 11 and memory span of 4. As we can see, the thermal effects alone do not play any fundamental role on the linearizability degradation. This is expected since the dominant thermal time constant,

approximately 1 ms (see Fig. 5.12), is too large to produce significant memory effects on a 2 MHz bandwidth signal, according to Fig. 5.5(a).

The results for the cases where only the trapping effects are considered (room temperature and average PA operating temperature), highlight the importance of a correct adjustment of the trapping time constants with temperature. For room temperature both devices present the same long emission time constant (around 20 ms), resulting in reasonably good ACPR levels. However, at a higher temperature, the difference, encoded in the Arrhenius equation, becomes more pronounced, with device 1 presenting $\tau_e \approx 40\mu$s and device 2 $\tau_e \approx 10\mu$s. This corresponds to a 7 dB difference in the ACPR levels as shown in Table 5.1, and in accordance to what is illustrated in Fig. 5.6. The significant drop in the NMSE levels when we compare step (2) with (3), observed in both devices, is due to the difficulty to completely compensate the strong class-C gain characteristic, as previously mentioned.

Table 5.1: Comparison of the Linearizability in Different Conditions

	Device 1		Device 2	
	ACPR (dB)	NMSE (dB)	ACPR (dB)	NMSE (dB)
(1) No long-term effects	-72.3	-59.3	-72.3	-59.3
(2) Only thermal effects	-69.5	-58.3	-69.5	-58.3
(3) Only trapping effects at room temperature	-67.9	-49.9	-67.9	-49.9
(4) Only trapping effects at high temperature (155°C)	-61.3	-46	-53.9	-40.3
(5) Trapping and thermal effects	-61.9	-46.4	-55.2	-41.1

Finally, the last test shows that the coupling between the temperature fluctuation and the trapping is negligible, only the average temperature offset has a significant impact. Figures 5.13(a) and 5.13(b) depict the obtained temperature and trapping control voltage for the considered envelope signal, respectively. Because the v_{trap} excursion is wider in device 2 than in 1, the PA hysteresis will be larger, which degrades the linearizability.

Fig. 5.13(c) shows that the influence of the temperature deviation from its mean value on the emission time constant is not that significant. Indeed, we can compare this variation with Fig. 5.6 and see that it is consistent with the results of Table 5.1. On the other hand, the difference between the two device's average emission time constant appears to be the biggest cause for the linearizability difference between them.

Other Signal Types

Please note that, in scenarios where the average dissipated power changes considerably over time, such as when the PA is excited with TDD or slotted signals, a high temperature variation could be observed over a long period of time. Therefore, the impact of thermal effects may be revealed, either due to a direct impact on the AM/AM and AM/PM curves or due to the modulation of the trapping emission time constant, which can further compromise

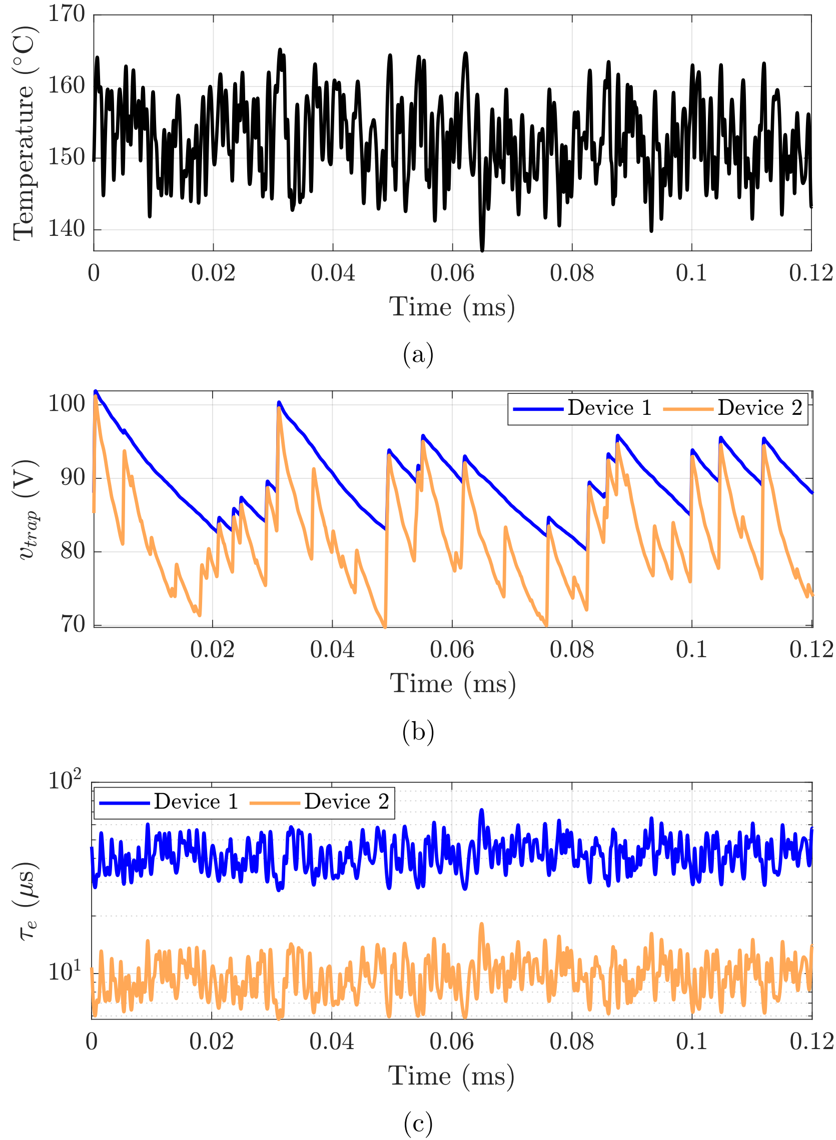

Figure 5.13: Simulated (a) junction temperature variation, (b) trapping control voltage variation and (c) the respective trapping emission time constant affected by the temperature variation.

---

the PA linearizability. For that, we considered a slotted signal with a duty cycle of 50% and a 1 ms period, as shown in Fig. 5.14(a). During the off-period, the PA has time to cool down and so, during the actual signal (the on-period) we observe a slow increase of temperature [Fig. 5.14(a)]. This will have a direct impact on the PA linearizability, because of the slow shift of the AM/AM and AM/PM characteristics, as was already shown in [142] for Si-LDMOS devices, and solved using more specialized and complex DPD architectures.

However, this will also affect the emission time constant, as we can see by the significant modulation of its value as the temperature rises, varying almost an order of magnitude as depicted in Fig. 5.14(b). Naturally, this will further contribute to an increase of complexity in the PA linearization, as the DPD now needs to handle with stretched time constants. In fact,

looking at the trapping control voltage on Fig. 5.14(c), specifically to the recovery during the off-period, this stretched behavior effect is well visible.

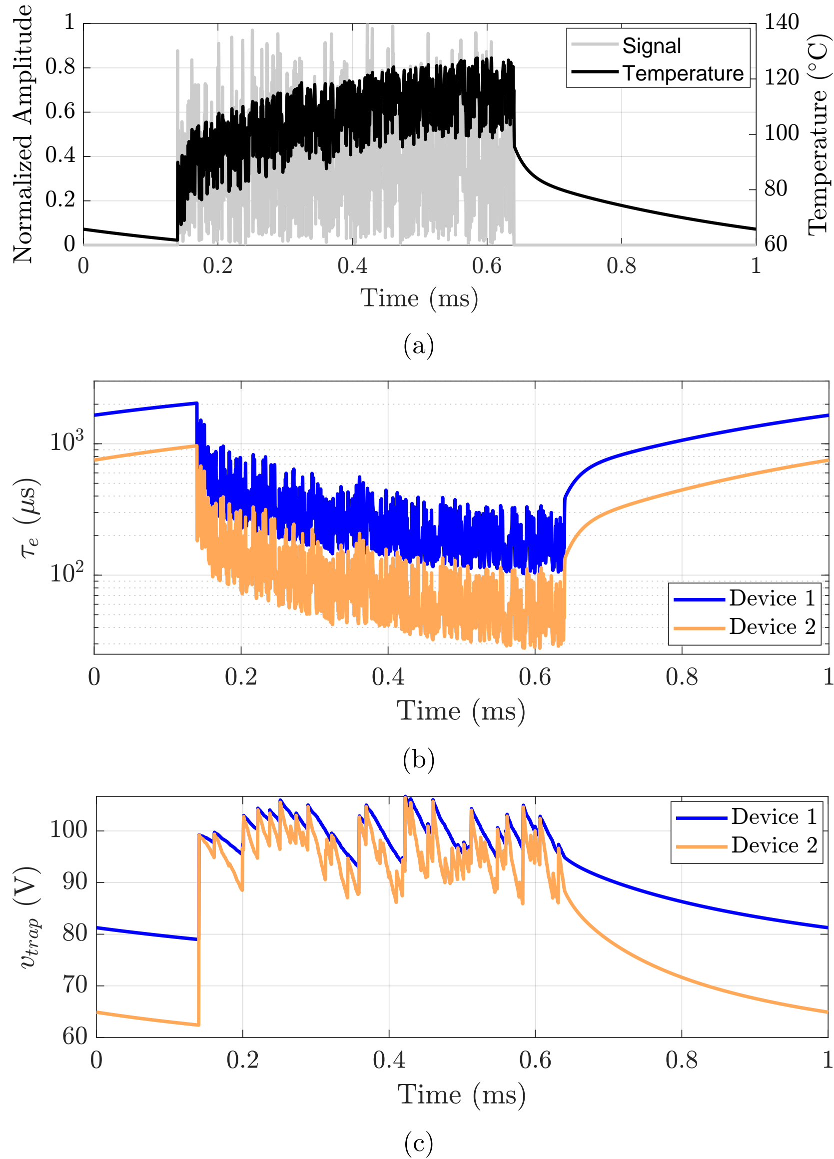

Figure 5.14: Simulated (a) slotted signal and junction temperature variation, (b) trapping emission time constant affected by the temperature variation and (c) trapping control voltage variation.

5.3 Validation

So, regarding the connection between long-term memory and the linearizability of a typical GaN HEMT-based PA, the great deterrent appears to be the modulation of the transistor's characteristics by deep-level traps whose emission time constant are closely related to the variation rate of the envelope. Self-heating, on its own, has not that much relevance to the

linearizability of the transistor. However, when considered in a device affected by traps, it becomes essential given that the average temperature imposes the emission time constant.

In order to validate the conclusions taken from the previous section, we used a class-AB 100 W GaN HEMT-based PA centered at 2 GHz. Fig. 5.15 shows a picture of the implemented PA. The tested PA performance is illustrated by its CW characteristics, the simulated load-line for the center frequency on top of the pulsed IV curves (for $V_{DQ} = 90$V) and the impedance profile over frequency in Fig. 5.16. As mentioned, we have two devices (with a total gate periphery of 16 mm) with the same nominal layer structure, but different trapping fingerprints. Since both devices have similar static performances, we can use the same PA to perform our tests, guaranteeing that the only thing that changes is the dynamic behavior.

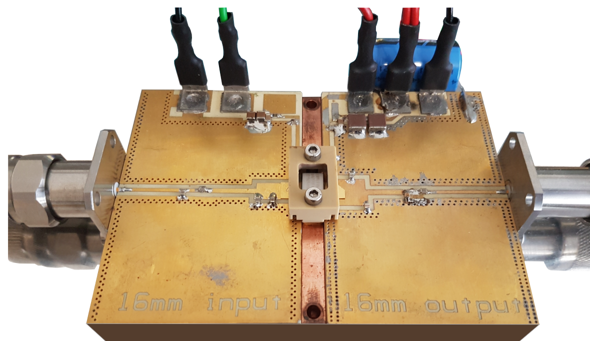

Figure 5.15: 100W GaN HEMT-based PA centered at 2 GHz.

To perform the measurements, we used the setup shown in Fig. 5.17. The setup is composed by a SMW200A vector signal generator and a FSW vector signal analyzer from Rohde & Schwarz; this equipment is operated via MATLAB. To adjust signal power to drive our PA under test, a ZHL-30W-252-S+ PA from Mini-circuits is used. This driver PA has a maximum output power of 30W. For the performed tests, the PA under test was excited until 1dB compression of the gain is observed (corresponding to a peak output power close to 100W), which is inline with the maximum PA output power.

Firstly, we want to confirm that what is being left uncompensated on these devices is indeed caused by the detrapping effect. It has been shown in [8], that we can indirectly observe the manifestation of long-term memory by the incapability of a standard DPD to compensate it. For that, we rely on a MP (with order 11 and a memory span of 4 samples) that accounts for both short and some of the medium-term memory. The remaining slower transients, which are not picked up by the predistorter, will thus be visible in the residuals. For the purpose of this work, we will only focus on the AM/AM dispersion where the trapping is more consequential. So, the amplitude residuals are defined as:

$$r = \frac{|x|}{max(|x|)} - \frac{|y|}{max(|y|)} \tag{5.1}$$

where x is the original signal and y is the output of the PA plus the DPD system.

Using a pulsed modulated signal, we can exacerbate the trapping capture and use it to highlight the long-term memory resulting from the subsequent emission. Fig. 5.18 compares the residues, calculated according to [8], of the measured output with the respective simulated trapping response, when the PA is excited with such a pulsed signal. The emission time

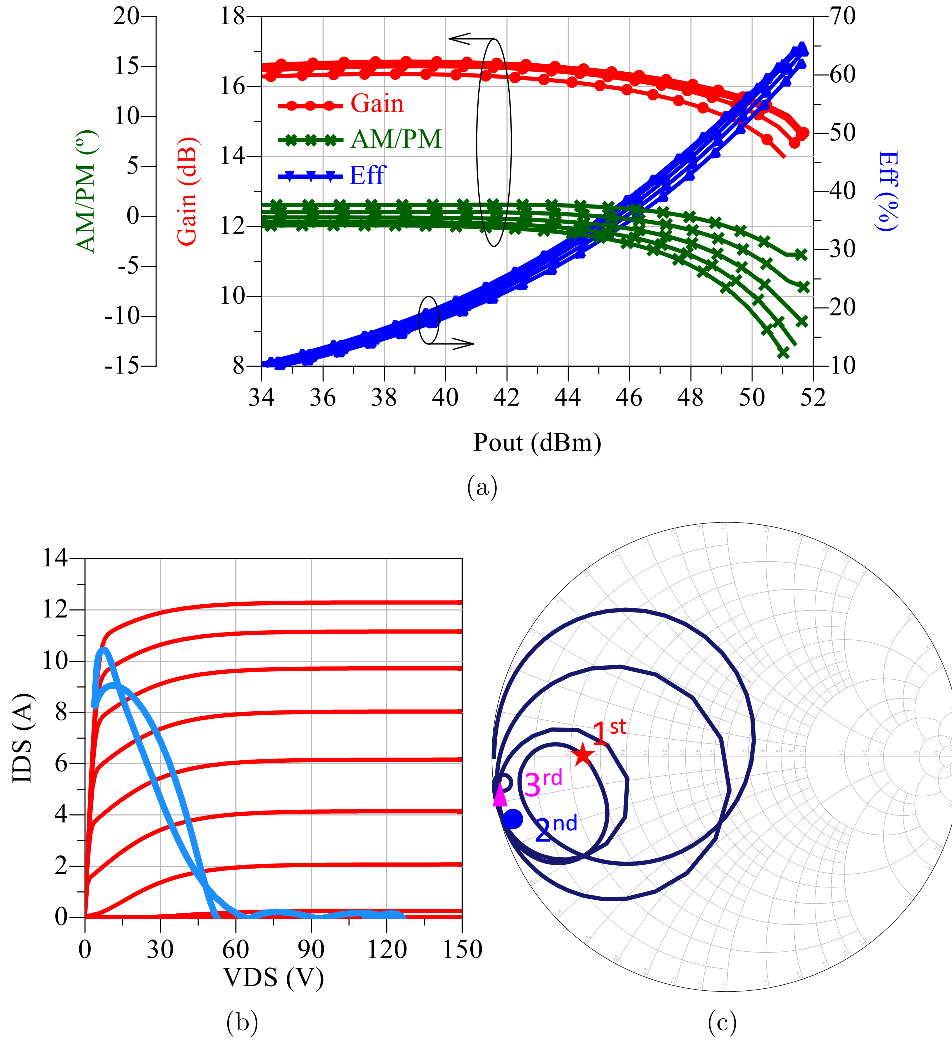

Figure 5.16: (a) Simulated CW gain, efficiency, and AM/PM response of the designed PA. Each curve corresponds to a different center frequency from 1.95 GHz to 2.05 GHz with a 20 MHz step; (b) the simulated load-line at the current source plane, with the bias point $[I_{DS}, V_{DS}, V_{GS}] = [100\,\text{mA}, 50\,\text{V}, -2.7\,\text{V}]$, and for the center frequency (2 GHZ) on top of the pulsed IV curves (for $V_{DQ} = 90\text{V}$); and (c) the impedance profile over frequency with the fundamental and harmonic impedances of the center frequency (2 GHz) marked.

---

constants are selected according to the Arrhenius plot linearization and the simulated device temperature.

The good agreement between the slow transients of the residuals indicates that they are indeed caused by the detrapping. The emission time constants obtained for both devices are in accordance with what was extracted from the Arrhenius equation, showing that device 2 has an apparent emission time constant smaller than the one of device 1 when the PA is operating (due to self-heating). Please remember that both devices have practically the same static response and were measured in the same conditions so the temperature variation should be very similar for the two. The fact that we see such distinct long-term time constants is a clear indication that the main effect bypassing the DPD is the slow emission transient of

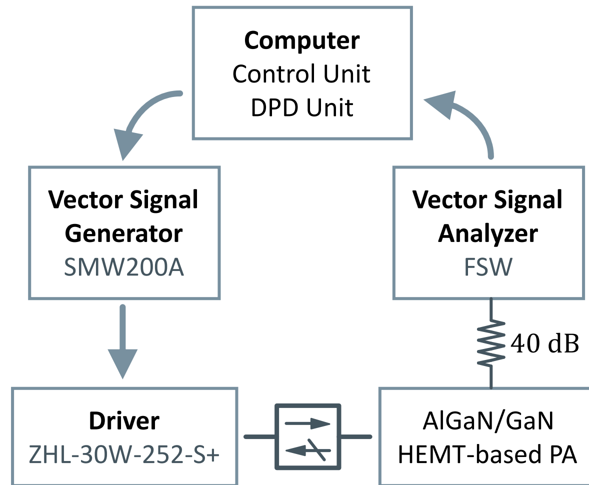

Figure 5.17: Diagram of the setup used to performed the measurements in this section.

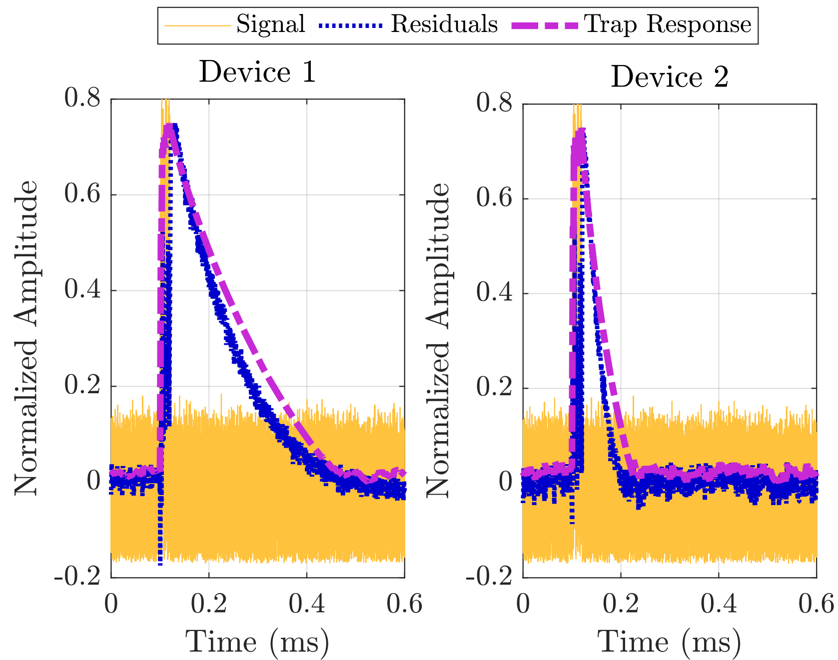

Figure 5.18: Measured DPD residuals and the respective simulated trapping response considering the emission time constant varying accordingly to the Arrhenius plot linearization and the simulated device temperature.

---

deep-level traps.

Secondly, to confirm the lower linearizability of device 2 with respect to device 1, Fig. 5.19 shows the ACPR of the PA after DPD. Both devices begin with similar linearity metrics but then become more distinct as the DPD iterations progress. Fig. 5.20 presents the spectrum for the last iteration on top of the reference signal.

Finally, as we demonstrated before, the maximum linearity degradation happens when the long-term time constant is closer to the variation rate of the envelope. We could thus vary

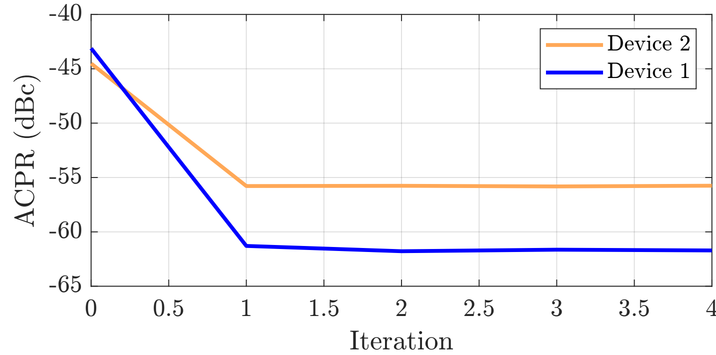

Figure 5.19: Measured ACPR values for different DPD adaptation iterations, considering the 2 MHz LTE signal.

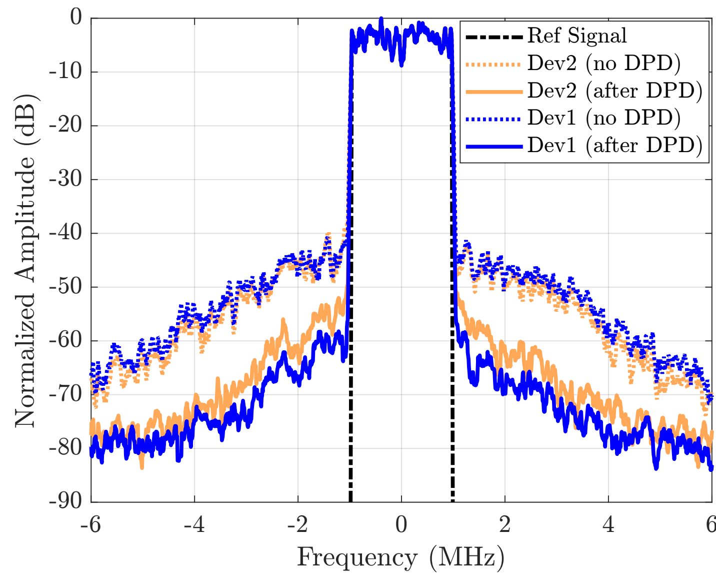

Figure 5.20: Measured spectrum of the reference signal and the output signal before (dashed lines) and after (solid lines) the DPD correction for both devices considering the 2 MHz LTE signal.

---

either the emission time constant (by changing the temperature) or the signal bandwidth, since what matters is the ratio between the two, and confirm if, indeed, we observe the expected variation of the linearity metrics.

Fig. 5.21 presents measured and simulated results for this experiment when we sweep the signal bandwidth and keep the normal PA operating temperature fixed. Note that we maintain the same probability distribution between signals of different bandwidths to allow a fair comparison. From the analysis developed in the first part of this Chapter, we can interpret these results in the following manner: increasing the signal bandwidth for a fixed emission time constant works as if we fixed the former and decreased the latter. In other words, when the signal varies faster, the traps seem slower and, consequently, the amplitude of the trapping state changes less, which reduces the impact of the memory on the device. That is why we observe very good linearity metrics for the highest bandwidth in Fig. 5.21.

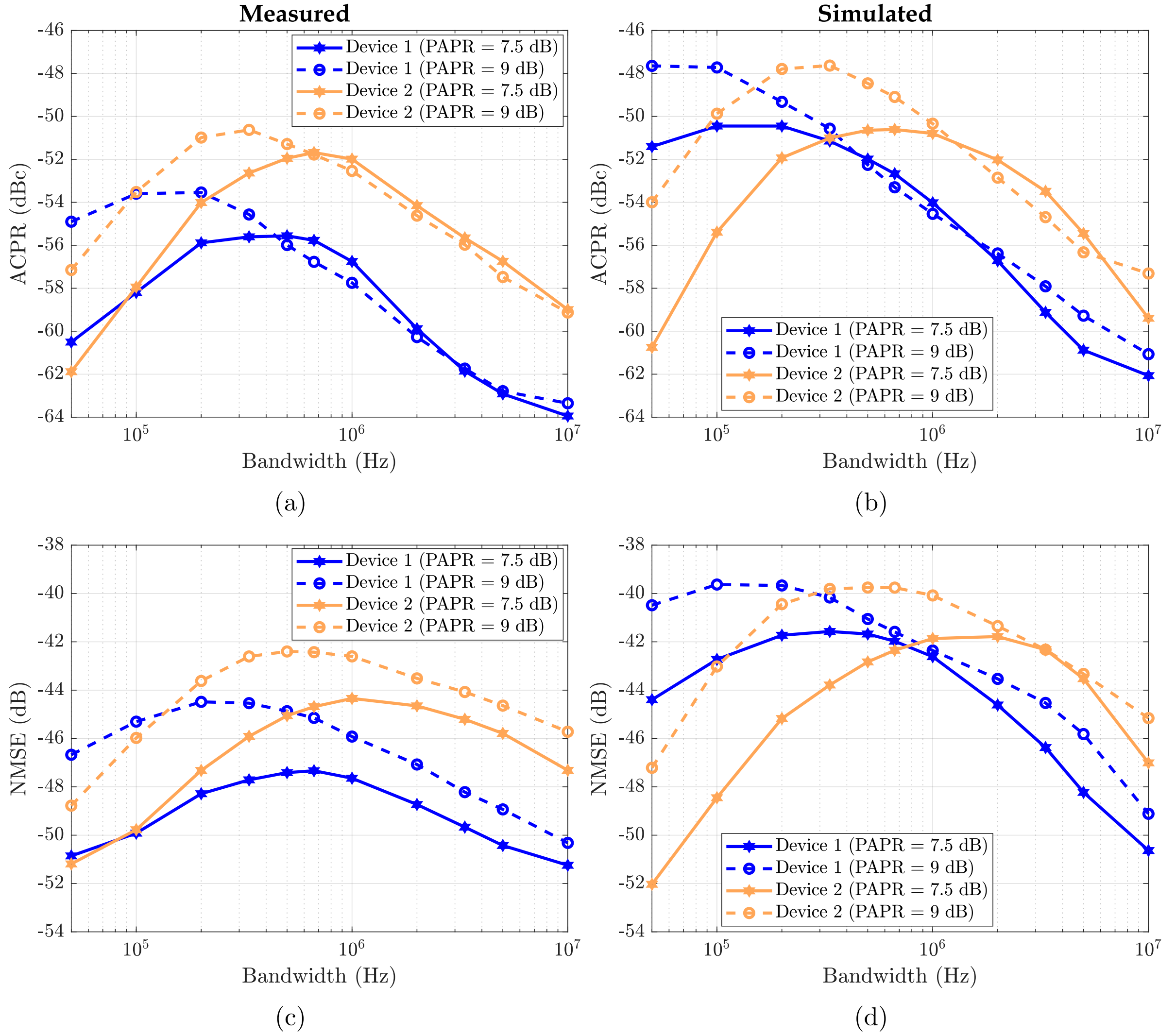

Figure 5.21: Measured (a) ACPR and (c) NMSE and simulated (b) ACPR and (d) NMSE levels after DPD versus signal bandwidth in both devices for LTE-type signals with two different PAPR levels.

When we decrease the bandwidth, the v_{trap} excursion throughout the signal becomes larger and the linearizability gets degraded. Once we reach the peak, even though the trapping state amplitude fluctuations continue to rise, they become increasingly more correlated with the envelope signal. For a low enough bandwidth, the accumulated charge changes at the same rate as the envelope signal, and so the device appears static. Because the trapping phenomena in device 2 is inherently faster, it reaches the worst case scenario at higher bandwidths than device 1.

Similarly, if we vary the mean PA temperature via signals with different PAPR, we can observe the expected peak deviation. A higher PAPR results in a lower average dissipated power, which means a lower average temperature. In this case, the emission time constant becomes larger and, consequently, the maximum degradation peak shifts to lower bandwidths.

It is interesting to note that, although the simulations indicate only a horizontal shift

of the ACPR and NMSE profiles between the two devices for the same PAPR level, which is to be expected because the static characteristics were assumed the same, in reality the small static differences between the two devices show that there are other factors at play that are not being accounted for. Nevertheless, the bell-shaped profile is consistent both in the simulations and measurements, as well as in both devices, which is in excellent agreement to the explanations and simulations presented in sections 5.1 and 5.2 of this Chapter.

Please note that in a real broadband signal, which may have much higher bandwidths than the ones tested in this paper, the presence of training sequences, slots, power variations and so on, leads to slow varying envelopes that could match the trapping time constants. As explained in this paper, the trapping phenomena works similarly to a peak detector. So, even for high bandwidth signals, if charge capture inducing peaks are sufficiently spread, then trapping dynamics will be excited.

Chapter 6

Conclusions and Future Work

This thesis presents the outcome of a four year PhD project, including a two year research partnership with Ampleon, whose goal was to establish a meaningful link between trapping effects and the linearizability of modern AlGaN/GaN HEMT-based PAs. The motivation rose from the current compromise between the excellent features of AlGaN/GaN HEMTs and the undesired trapping effects that, on the one hand, are vital to the proper device operation but, on the other hand, are the reason for long-term memory effects capable of bypassing standard DPD schemes. This work is also the first direct return from the investment taken by our group into a new field of research - semiconductor device physics and TCAD simulations - that started with this PhD.

Chapter 2 begins with an overview of the modern AlGaN/GaN HEMT and the reasons for its current architecture. Here, we realize the importance of buffer traps to reduce lateral current leakage down to reasonable levels. Naturally, there is now a myriad of possible alternative structures to mitigate this unwanted effect without relying on the standard Fe-doped (or C-doped) buffer layer and, in fact, this might be one of the most important research topics of the moment. Understanding what is the best approach to reduce short channel effects as the technology aggressively pursues smaller gate lengths is a question that is far from being answered, as many of these novel structures, like the N-polar GaN/AlGaN [101] or the "buffer-free" heterostructure [86, 88], are still relatively new.

Although not entirely related with the trapping effects issue, it should be noted that the choice of the substrate material appears to be an equally hot topic at the moment. We have three big bets at the moment: silicon, silicon carbide and diamond. Each with its own advantages, which makes them more suitable for some applications than others. Silicon has been receiving considerable attention lately, as it is still relatively new as a substrate, with margin to grow, and with opportunities in the telecommunications field that are yet to be explored.

In this sense, it might seem that a thesis entirely devoted to a specific device, like the passivated AlGaN/GaN HEMT with a Fe-doped buffer layer on top of a silicon carbide substrate, could be somewhat narrow in scope, particularly given the close ties between buffer traps, the way this device operates and the main reason for linearizability concern. One could be tempted to say that by moving to a different device, the conclusions taken throughout this thesis would no longer be relevant. However, there are several reasons for selecting the most mature technology in the market. For once, it develops slowly enough to ensure that the device characterization remains valid after a four year PhD project. On top of that, we had a

vast amount of work already done on this technology that facilitated the accomplishment of this ambitious goal. More importantly though, this device represents the state-of-the-art of commercial off-the-shelf GaN HEMTs for telecommunications where linearity is a key metric. However, even if the standard AlGaN/GaN HEMT would become obsolete next year, we would argue that this work still retains its value in the presented thought process required to link certain physical characteristics of a device to something as high level, as the linearity of a predistorted power amplifier.

Also in this Chapter 2, we provide an insight on how buffer traps work to prevent current leakage, through TCAD simulations, that will later help us better understand the foundations of the SRH-inspired equivalent circuit models for trapping effects. As far as we know, this in-depth explanation has never been published and it could serve as a good starting point for a future paper that attempts to lay down a unified and physically-supported model for predicting the trapping effects caused by buffer traps.

The dynamics of buffer traps are then described thoroughly on Chapter 3, starting with an explanation of the single trap energy level SRH model, followed by the best known adaptations of this model to the particular case of the HEMT. This knowledge helped understanding the specific flaws of each adaptation, namely the Kunihiro and Ohno model and the Rathmell and Parker model, and also contributed to the improvement of the latter. However, as we mentioned, a very important part of the puzzle is still missing, i.e. a physically-supported model that accurately represents the injection of electrons from the 2DEG into the buffer region. In this thesis, and in the original paper [123], this is being emulated by a purely behavioral expression.

Despite the apparent success of the SRH model, the consistent appearance of drain-lag transient profiles with either stretched or multiple inflection points featured in our measurements should make us re-consider the validity of the single trap energy level. Furthermore, there is also, in most devices, the presence of a substantial background carbon doping on the buffer layer, which on its own should already add some complexity to the overall trapping dynamics. It seems, therefore, that addressing buffer traps as a simple single energy level might degrade the accuracy of the trapping model. However, this issue, as far as we know, remains poorly explored. On top of all this, there are a couple of effects observed in some AlGaN/GaN HEMTs (like gate lag, hot electrons, kink effect, among others) that go beyond what is foreseen by the SRH model. These might be related to processes such as hopping or tunneling, that have been previously suggested [40, 94], and, consequently, require different physical models.

Essentially, there is still plenty of room to improve our current understanding of trapping effects and how to properly represent them in a compact model formulation.

Chapter 4 describes a novel double-pulse based method, where the core of the setup is an arbitrary waveform generator that allows us to generate any voltage waveform. Due to the limited output power of these instruments, a fast and high voltage amplifier (pulser) is required to pulse the device. The essential difference between this method and previous ones lies in the inherent flexibility of our setup to characterize the capture and emission transients in a wide temporal span under guaranteed isothermal conditions.

A key achievement from this experimental methodology was proving the existence of a stretched capture transient, providing the framework to contest the assumption behind the forcing function of the Rathmell and Parker model. From this, we proposed a more accurate interpretation of the capture dynamics, featuring a variable time constant, as already used in the Kunihiro and Ohno model, but without resorting to their first-order approxima-

tion of the SRH model. Furthermore, although not presented in this thesis, these findings contributed to a significant improvement of the pulse-to-pulse stability prediction when the PA is excited by pulsed radar signals. This work was initially submitted and presented at the 2018 International Workshop on Integrated Nonlinear Microwave and Millimetre-wave Circuits (INMMIC) [45] and later extended and published at the Microwave Theory and Techniques Journal [46].

Later on, also not shown in this thesis, the same biasing methodology was adapted to transient pulsed S-parameters. We were able to characterize, not only the trapping dynamics on i_{DS}, but also on the intrinsic capacitances of the HEMT for the entire I-V plane. This work was submitted and presented at the 2020 International Workshop on Integrated Nonlinear Microwave and Millimetre-wave Circuits (INMMIC) [47] and was awarded the 2nd place in the best student paper competition. Additionally, we came up with an explanation for the observed differences in the trapping time constants extracted from the device's low frequency output admittance, Y_{22}, and I-DLTS on GaN HEMTs [54], based on the SRH model. The trapping time constant, not being a physical identity, but rather a parameter of a model, can vary according to the conditions of extraction. This dependence is, in fact, clearly seen in Y_{22} and I-DLTS measurements, as they are made respectively under small-signal steady-state and large-signal transient conditions.

DLTS has been extensively used to characterize the electronic features of defects in semiconductors with activation energies up to ~ 1 eV [135]. However, if we were to implement trap centers in our TCAD template we would still need to specify both their concentration and spatial distribution. Finding experimental methodologies that also provide this information is essential for a complete trapping characterization.

These features can be probed in test structures like Schottky diodes or p-n junctions but it is much more difficult to do it on actual HEMTs, due to their very small capacitances. So, there has been attempts to grow diodes in the same growing conditions of the HEMT to characterize the traps by cross validation. Unfortunately, the distribution of the electric field tends to be different in these devices, which could corrupt the analysis [40]. In [143], they propose a measurement methodology to separate surface- from buffer-related trapping effects on a 4-terminal transistor (with the fourth terminal below the substrate). By playing with the applied biases, they can force the presence of an electric field with just a vertical component (which they assume only excites buffer traps) or a horizontal component (that only excites surface traps). A more recent work [144, 145] proposes an alternative methodology capable of quantifying the amount of trapped charge during a pulsed transient and also separate the influence of surface and buffer traps, directly on a conventional 3-terminal GaN HEMT. The assumption behind this method is that the current flowing into the drain and out of the source terminals are different when trapping takes place. This difference accounts [supposedly] for the electrons flowing into the source terminal that are then trapped in the buffer layer, preventing them from flowing out from the drain, causing $i_S > i_D$. This method should then allow the distinction between buffer and surface trap effects, since the latter should not cause a difference between the two currents. Moreover, the time integration of $i_S - i_D$ should provide a direct observation to both the amount of trapped charge in the buffer, as well as to the trapping time constants, unaffected by the nonlinearity of the drain current. Unfortunately, not only have we failed to replicate this method both on TCAD simulations and measurements, as we also found no physical support to corroborate the idea that $i_S \neq i_D$ because of trapped charge, since this would imply a device with a non-neutral state.

Therefore, finding well demonstrated and physically supported ways to probe the location

and concentration of traps directly on HEMTs is of the utmost importance for future progress in this field.

In Chapter 5 we studied the relationship between the detrapping time constant and the achievable linearizability of GaN HEMT-based PAs, showing that the worst-case scenario happens when the emission time constant is on the order of the time between consecutive envelope peaks above a certain amplitude threshold. This is the case for which we observed a more pronounced hysteresis on the gain and phase-shift characteristics, and so, a stronger impact of the memory effects. Moreover, we have also demonstrated how important the self-heating is to accurately predict the PA linearizability, given the strong temperature dependence of the emission time constant. To demonstrate these two points, we have used two PAs based on two GaN HEMT devices with the same structure and similar static RF performance, but with a dominant trapping signature characterized by apparently distinct activation energies and cross-sections. These particular devices showed similar emission time constants at room temperature but different ones when the PA is under nominal dissipated power operation, reinforcing the importance of a correct temperature estimation. The ACPR and NMSE profiles, obtained after DPD, as a function of the signal bandwidth, coincide with our predictions, with the worst-case scenario happening at different bandwidths, in accordance to the expected difference between the two devices. This work was published at the Microwave Theory and Techniques Journal [49]. Fig. 5.21 epitomizes both the main achievement of this work and what was left behind. On the one hand, the similarity between the measurements and simulations, specially after all the layers of consecutive approximations required, validated our perception of which should be the dominant effects on a macro level. On the other hand, there are certain differences between measurements and simulations that are still hard do explain. Perhaps the most noticeable one is when we compare the linearity level at the worst case scenario for both devices. Device 1 has clearly the highest linearizability of the two devices, even though their static characteristics are extremely alike. Another discrepancy, particularly visible on Device 1, is the different peak position for the simulated and measured profiles. This suggests that there are still some features of the device that are not being properly implemented in our models, and require further attention.

Despite the inaccuracies of our model, we still found a profound connection between the trapping dynamics and the linearizability of the PA. As a next step, it would be interesting to understand the impact of this knowledge to help shape future DPD schemes. But it would be also relevant to figure out, at a device level, what could be done to design more linearizable HEMTs.

Bibliography

[1] P. Lavrador, T. Cunha, P. Cabral, and J. Pedro, "The Linearity-Efficiency Compromise," *IEEE Microw. Mag.*, vol. 11, pp. 44–58, aug 2010.

[2] M. Series, "IMT Vision - Framework and overall objectives of the future development of IMT for 2020 and beyond," tech. rep., 2015.

[3] A. Katz, J. Wood, and D. Chokola, "The Evolution of PA Linearization: From Classic Feedforward and Feedback Through Analog and Digital Predistortion," *IEEE Microw. Mag.*, vol. 17, no. 2, pp. 32–40, 2016.

[4] P. Pascual Campo, V. Lampu, A. Meirhaeghe, J. Boutellier, L. Anttila, and M. Valkama, "Digital Predistortion for 5G Small Cell: GPU Implementation and RF Measurements," *J. Signal Process. Syst.*, vol. 92, no. 5, pp. 475–486, 2020.

[5] O. Arnold, F. Richter, G. Fettweis, and O. Blume, "Power consumption modeling of different base station types in heterogeneous cellular networks," *2010 Futur. Netw. Mob. Summit*, pp. 1–8, 2010.

[6] J. Lorincz, T. Garma, and G. Petrovic, "Measurements and Modelling of Base Station Power Consumption under Real Traffic Loads," *Sensors*, vol. 12, pp. 4281–4310, mar 2012.

[7] M. Deruyck, W. Joseph, and L. Martens, "Power consumption model for macrocell and microcell base stations," *Trans. Emerg. Telecommun. Technol.*, vol. 25, pp. 320–333, mar 2014.

[8] F. M. Barradas, *Modeling and Digital Predistortion of Wireless Radio Frequency Transmitters.* PhD thesis, Universidade de Aveiro, 2017.

[9] R. Quaglia and S. Cripps, "A Load Modulated Balanced Amplifier for Telecom Applications," *IEEE Trans. Microw. Theory Tech.*, vol. 66, pp. 1328–1338, mar 2018.

[10] V. Camarchia, M. Pirola, R. Quaglia, S. Jee, Y. Cho, and B. Kim, "The Doherty Power Amplifier: Review of Recent Solutions and Trends," *IEEE Trans. Microw. Theory Tech.*, vol. 63, pp. 559–571, feb 2015.

[11] T. Barton, "Not Just a Phase: Outphasing Power Amplifiers," *IEEE Microw. Mag.*, vol. 17, no. 2, pp. 18–31, 2016.

[12] P. Asbeck and Z. Popovic, "ET Comes of Age: Envelope Tracking for Higher-Efficiency Power Amplifiers," *IEEE Microw. Mag.*, vol. 17, pp. 16–25, mar 2016.

[13] Q. A. Pham, G. Montoro, D. López-Bueno, and P. L. Gilabert, "Dynamic Selection and Estimation of the Digital Predistorter Parameters for Power Amplifier Linearization," *IEEE Trans. Microw. Theory Tech.*, vol. 67, no. 10, pp. 3996–4004, 2019.

[14] M. Mengozzi, G. P. Gibiino, A. M. Angelotti, C. Florian, and A. Santarelli, "GaN power amplifier digital predistortion by multi-objective optimization for maximum RF output power," *Electron.*, vol. 10, no. 3, pp. 1–12, 2021.

[15] D. Morgan, Z. Ma, J. Kim, M. Zierdt, and J. Pastalan, "A Generalized Memory Polynomial Model for Digital Predistortion of RF Power Amplifiers," *IEEE Trans. Signal Process.*, vol. 54, pp. 3852–3860, oct 2006.

[16] W. Chen, G. Lv, X. Liu, D. Wang, and F. M. Ghannouchi, "Doherty PAs for 5G Massive MIMO: Energy-Efficient Integrated DPA MMICs for Sub-6-GHz and mm-Wave 5G Massive MIMO Systems," *IEEE Microw. Mag.*, vol. 21, no. 5, pp. 78–93, 2020.

[17] S. Chen and J. Zhao, "The requirements, challenges, and technologies for 5G of terrestrial mobile telecommunication," *IEEE Commun. Mag.*, vol. 52, no. 5, pp. 36–43, 2014.

[18] S. Rangan, T. S. Rappaport, and E. Erkip, "Millimeter-wave cellular wireless networks: Potentials and challenges," *Proc. IEEE*, vol. 102, no. 3, pp. 366–385, 2014.

[19] P. Tomé, *Characterization, Modeling and Compensation of Long-Term Memory Effects in GaN HEMT-Based Radio-Frequency Power Amplifiers.* PhD thesis, Universidade de Aveiro, 2020.

[20] C. Fager, T. Eriksson, F. Barradas, K. Hausmair, T. Cunha, and J. C. Pedro, "Linearity and Efficiency in 5G Transmitters: New Techniques for Analyzing Efficiency, Linearity, and Linearization in a 5G Active Antenna Transmitter Context," *IEEE Microw. Mag.*, vol. 20, pp. 35–49, may 2019.

[21] T. Das, "Designing wide instantaneous bandwidth Doherty PAs for cellular," *Microw. J.*, vol. 62, no. 5, pp. 168–178, 2019.

[22] A. Alt and J. Lees, "Improving efficiency, linearity and linearisability of an asymmetric doherty power amplifier by modulating the peaking Amplifier's supply voltage," in *2017 47th Eur. Microw. Conf.*, vol. 2017-Janua, pp. 464–467, IEEE, oct 2017.

[23] J. Pedro, P. Tome, T. Cunha, F. Barradas, L. Nunes, P. Cabral, and J. Gomes, "A Review of Memory Effects in AlGaN/GaN HEMT Based RF PAs," in *2021 IEEE MTT-S Int. Wirel. Symp.*, pp. 1–3, IEEE, may 2021.

[24] S. Boumaiza and F. Ghannouchi, "Thermal memory effects modeling and compensation in RF power amplifiers and predistortion linearizers," *IEEE Trans. Microw. Theory Tech.*, vol. 51, pp. 2427–2433, dec 2003.

[25] L. C. Nunes, D. R. Barros, P. M. Cabral, and J. C. Pedro, "Efficiency Degradation Analysis in Wideband Power Amplifiers," *IEEE Trans. Microw. Theory Tech.*, vol. 66, pp. 5640–5651, dec 2018.

[26] D. R. Barros, L. C. Nunes, P. M. Cabral, and J. C. Pedro, "Impact of the Input Baseband Terminations on the Efficiency of Wideband Power Amplifiers Under Concurrent Band Operation," *IEEE Trans. Microw. Theory Tech.*, vol. 67, pp. 5127–5138, dec 2019.

[27] V. Camarchia, R. Quaglia, A. Piacibello, D. P. Nguyen, H. Wang, and A.-V. Pham, "A Review of Technologies and Design Techniques of Millimeter-Wave Power Amplifiers," *IEEE Trans. Microw. Theory Tech.*, vol. 68, pp. 2957–2983, jul 2020.

[28] H. Li, K. Bathich, O. Bengtsson, and G. Boeck, "A Si LDMOS class AB power amplifier for UMTS LTE base stations," *Ger. Microw. Conf. Dig. Pap. GeMIC 2010*, vol. 8, no. c, pp. 272–275, 2010.

[29] D. W. Runton and B. Trabert, "History of GaN," *IEEE Microw. Mag.*, no. April 2013, pp. 82–93, 2013.

[30] R. Chu, "GaN power switches on the rise: Demonstrated benefits and unrealized potentials," 2020.

[31] R. Ma, K. H. Teo, S. Shinjo, K. Yamanaka, and P. M. Asbeck, "A GaN PA for 4G LTE-Advanced and 5G: Meeting the Telecommunication Needs of Various Vertical Sectors Including Automobiles, Robotics, Health Care, Factory Automation, Agriculture, Education, and More," *IEEE Microw. Mag.*, vol. 18, pp. 77–85, nov 2017.

[32] H. Wang, T.-Y. Huang, N. S. Mannem, J. Lee, E. Garay, D. Munzer, E. Liu, Y. Liu, B. Lin, M. Eleraky, S. Li, F. Wang, A. S. Ahmed, C. Snyder, S. Lee, H. T. Nguyen, and M. E. D. Smith, "Power Amplifiers Performance Survey 2000-Present."

[33] U. Mishra, P. Parikh, and Yi-Feng Wu, "AlGaN/GaN HEMTs-an overview of device operation and applications," *Proc. IEEE*, vol. 90, pp. 1022–1031, jun 2002.

[34] U. Mishra, Shen Likun, T. Kazior, and Yi-Feng Wu, "GaN-Based RF Power Devices and Amplifiers," *Proc. IEEE*, vol. 96, pp. 287–305, feb 2008.

[35] L. Dunleavy, C. Baylis, W. Curtice, and R. Connick, "Modeling GaN: Powerful but challenging," in *IEEE Microw. Mag.*, vol. 11, pp. 82–96, 2010.

[36] L. C. Nunes, P. M. Cabral, and J. C. Pedro, "AM/AM and AM/PM Distortion Generation Mechanisms in Si LDMOS and GaN HEMT Based RF Power Amplifiers," *IEEE Trans. Microw. Theory Tech.*, vol. 62, pp. 799–809, apr 2014.

[37] T. Mizutani, Y. Ohno, S. Kishimoto, and K. Maezawa, "A study on current collapse in AlGaN/GaN HEMTs induced by bias stress," *IEEE Trans. Electron Devices*, vol. 50, no. 10, pp. 2015–2020, 2003.

[38] D. Jin and J. A. Del Alamo, "Mechanisms responsible for dynamic ON-resistance in GaN high-voltage HEMTs," *Proc. Int. Symp. Power Semicond. Devices ICs*, no. June, pp. 333–336, 2012.

[39] P. McGovern, P. J. Tasker, J. Powell, K. P. Hilton, J. L. Glasper, R. S. Balmer, T. Martin, and M. J. Uren, "Experimental investigation of DC-RF dispersion in AlGaN/GaN HFET's using pulsed I-V and time-domain waveform measurements," *2005 Int. Conf. Compd. Semicond. Manuf. Technol.*, vol. 00, no. C, pp. 503–506, 2005.

[40] D. Bisi, M. Meneghini, C. De Santi, A. Chini, M. Dammann, P. Bruckner, M. Mikulla, G. Meneghesso, and E. Zanoni, "Deep-level characterization in GaN HEMTs-Part I: Advantages and limitations of drain current transient measurements," *IEEE Trans. Electron Devices*, vol. 60, no. 10, pp. 3166–3175, 2013.

[41] A. Prasad, M. Thorsell, H. Zirath, and C. Fager, "Accurate Modeling of GaN HEMT RF Behavior Using an Effective Trapping Potential," *IEEE Trans. Microw. Theory Tech.*, vol. 66, no. 2, pp. 845–857, 2018.

[42] F. M. Barradas, L. C. Nunes, T. R. Cunha, P. M. Lavrador, P. M. Cabral, and J. C. Pedro, "Compensation of Long-Term Memory Effects on GaN HEMT-Based Power Amplifiers," *IEEE Trans. Microw. Theory Tech.*, vol. 65, no. 9, pp. 3379–3388, 2017.

[43] P. M. Tome, F. M. Barradas, T. R. Cunha, and J. C. Pedro, "Hybrid Analog/Digital Linearization of GaN HEMT-Based Power Amplifiers," *IEEE Trans. Microw. Theory Tech.*, vol. 67, no. 1, pp. 288–294, 2019.

[44] P. M. Tome, F. M. Barradas, T. R. Cunha, and J. C. Pedro, "A Multiple-Time-Scale Analog Circuit for the Compensation of Long-Term Memory Effects in GaN HEMT-Based Power Amplifiers," *IEEE Trans. Microw. Theory Tech.*, vol. 68, no. 9, pp. 3709–3723, 2020.

[45] J. L. Gomes, L. C. Nunes, C. F. Gonçalves, and J. C. Pedro, "Deep-Level Traps' Capture Time Constant and its Impact on Nonlinear GaN HEMT Modeling," *Int. Work. Integr. Nonlinear Microw. Millimetre-Wave Circuits, INMMIC 2018 - Proc.*, no. 2, pp. 8–10, 2018.

[46] J. L. Gomes, L. C. Nunes, C. F. Goncalves, and J. C. Pedro, "An Accurate Characterization of Capture Time Constants in GaN HEMTs," *IEEE Trans. Microw. Theory Tech.*, vol. 67, pp. 2465–2474, jul 2019.

[47] J. L. Gomes, L. C. Nunes, and J. C. Pedro, "Transient Pulsed S-Parameters for Trapping Characterization," in *2020 Int. Work. Integr. Nonlinear Microw. Millimetre-Wave Circuits*, pp. 1–3, IEEE, jul 2020.

[48] P. M. Tome, F. M. Barradas, L. C. Nunes, J. L. Gomes, T. R. Cunha, and J. C. Pedro, "Characterization, Modeling, and Compensation of the Dynamic Self-Biasing Behavior of GaN HEMT-Based Power Amplifiers," *IEEE Trans. Microw. Theory Tech.*, vol. 69, pp. 529–540, jan 2021.

[49] J. L. Gomes, L. C. Nunes, F. M. Barradas, A. Cooman, A. E. F. de Jong, R. M. Heeres, and J. C. Pedro, "The Impact of Long-Term Memory Effects on the Linearizability of GaN HEMT-Based Power Amplifiers," *IEEE Trans. Microw. Theory Tech.*, vol. 70, pp. 1377–1390, feb 2022.

[50] J. L. Gomes, L. C. Nunes, F. M. Barradas, and J. C. Pedro, "A Qualitative Explanation of the AlGaN/GaN HEMT Nonlinear Intrinsic Capacitances," in *2022 Int. Work. Integr. Nonlinear Microw. Millimetre-Wave Circuits*, vol. 2, pp. 1–3, IEEE, apr 2022.

[51] J. L. Gomes, L. C. Nunes, and J. C. Pedro, "On the Drain-to-Source Capacitance of Microwave FETs in Triode Region," in *2022 IEEE/MTT-S Int. Microw. Symp.*, pp. 1–3, 2022.

[52] J. Pedro, J. Gomes, and L. Nunes, "Electro-Thermal and Trapping Characterization of AlGaN/GaN RF Power HEMTs," *2021 IEEE BiCMOS Compd. Semicond. Integr. Circuits Technol. Symp. BCICTS 2021*, no. 2, 2021.

[53] P. M. Tome, F. M. Barradas, L. C. Nunes, J. L. Gomes, T. R. Cunha, and J. C. Pedro, "A Transient Two-Tone RF Method for the Characterization of Electron Trapping Capture and Emission Dynamics in GaN HEMTs," in *2020 IEEE/MTT-S Int. Microw. Symp.*, no. June, pp. 428–431, IEEE, aug 2020.

[54] J. L. Gomes, L. C. Nunes, and J. C. Pedro, "Explaining the Different Time Constants Extracted from Low Frequency Y 22 and I_{DS}-DLTS on GaN HEMTs," in *2020 IEEE/MTT-S Int. Microw. Symp.*, vol. 2020-Augus, pp. 432–435, IEEE, aug 2020.

[55] R. Dingle, H. L. Störmer, A. C. Gossard, and W. Wiegmann, "Electron mobilities in modulation-doped semiconductor heterojunction superlattices," *Appl. Phys. Lett.*, vol. 33, pp. 665–667, oct 1978.

[56] T. Mimura, S. Hiyamizu, T. Fujii, and K. Nanbu, "A New Field-Effect Transistor with Selectively Doped GaAs/n-$Al_xGa_{1-x}As$ Heterojunctions," *Jpn. J. Appl. Phys.*, vol. 19, no. 5, pp. 225–227, 1980.

[57] T. Mimura, "The early history of the high electron mobility transistor (HEMT)," *IEEE Trans. Microw. Theory Tech.*, vol. 50, pp. 780–782, mar 2002.

[58] T. Mimura, "Development of High Electron Mobility Transistor," *Jpn. J. Appl. Phys.*, vol. 44, pp. 8263–8268, dec 2005.

[59] S. Nakamura, Y. Harada, and M. Seno, "Novel metalorganic chemical vapor deposition system for GaN growth," *Appl. Phys. Lett.*, vol. 58, pp. 2021–2023, may 1991.

[60] M. Asif Khan, A. Bhattarai, J. N. Kuznia, and D. T. Olson, "High electron mobility transistor based on a GaN/$Al_xGa_{1-x}N$ heterojunction," *Appl. Phys. Lett.*, vol. 63, pp. 1214–1215, aug 1993.

[61] O. Ambacher, J. Smart, J. R. Shealy, N. G. Weimann, K. Chu, M. Murphy, W. J. Schaff, L. F. Eastman, R. Dimitrov, L. Wittmer, M. Stutzmann, W. Rieger, and J. Hilsenbeck, "Two-dimensional electron gases induced by spontaneous and piezoelectric polarization charges in N- and Ga-face AlGaN/GaN heterostructures," *J. Appl. Phys.*, vol. 85, pp. 3222–3233, mar 1999.

[62] S. Adachi, "GaAs, AlAs, and $Al_xGa_{1-x}As$: Material parameters for use in research and device applications," *J. Appl. Phys.*, vol. 58, pp. R1–R29, aug 1985.

[63] O. Ambacher, B. Foutz, J. Smart, J. R. Shealy, N. G. Weimann, K. Chu, M. Murphy, A. J. Sierakowski, W. J. Schaff, L. F. Eastman, R. Dimitrov, A. Mitchell, and M. Stutzmann, "Two dimensional electron gases induced by spontaneous and piezoelectric polarization in undoped and doped AlGaN/GaN heterostructures," *J. Appl. Phys.*, vol. 87, pp. 334–344, jan 2000.

[64] J. Redwing, J. Flynn, M. Tischler, W. Mitchel, and A. Saxler, "MOVPE Growth of High Electron Mobility AlGaN/GaN Heterostructures," *MRS Proc.*, vol. 395, p. 201, feb 1995.

[65] L. Eastman, V. Tilak, J. Smart, B. Green, E. Chumbes, R. Dimitrov, Hyungtak Kim, O. Ambacher, N. Weimann, T. Prunty, M. Murphy, W. Schaff, and J. Shealy, "Undoped AlGaN/GaN HEMTs for microwave power amplification," *IEEE Trans. Electron Devices*, vol. 48, pp. 479–485, mar 2001.

[66] J. P. Ibbetson, P. T. Fini, K. D. Ness, S. P. DenBaars, J. S. Speck, and U. K. Mishra, "Polarization effects, surface states, and the source of electrons in AlGaN/GaN heterostructure field effect transistors," *Appl. Phys. Lett.*, vol. 77, pp. 250–252, jul 2000.

[67] J. He, W. Cheng, Q. Wang, K. Cheng, H. Yu, and Y. Chai, "Recent Advances in GaN-Based Power HEMT Devices," *Adv. Electron. Mater.*, vol. 7, p. 2001045, apr 2021.

[68] T. Palacios, C.-S. Suh, A. Chakraborty, S. Keller, S. DenBaars, and U. Mishra, "High-performance E-mode AlGaN/GaN HEMTs," *IEEE Electron Device Lett.*, vol. 27, pp. 428–430, jun 2006.

[69] B. Lu, O. I. Saadat, and T. Palacios, "High-Performance Integrated Dual-Gate AlGaN/GaN Enhancement-Mode Transistor," *IEEE Electron Device Lett.*, vol. 31, pp. 990–992, sep 2010.

[70] R. S. Pengelly, S. M. Wood, J. W. Milligan, S. T. Sheppard, and W. L. Pribble, "A Review of GaN on SiC High Electron-Mobility Power Transistors and MMICs," *IEEE Trans. Microw. Theory Tech.*, vol. 60, pp. 1764–1783, jun 2012.

[71] J. Pomeroy, M. Bernardoni, A. Sarua, A. Manoi, D. C. Dumka, D. M. Fanning, and M. Kuball, "Achieving the best thermal performance for GaN-on-diamond," *Tech. Dig. - IEEE Compd. Semicond. Integr. Circuit Symp. CSIC*, pp. 15–18, 2013.

[72] K. J. Chen, O. Haberlen, A. Lidow, C. L. Tsai, T. Ueda, Y. Uemoto, and Y. Wu, "GaN-on-Si Power Technology: Devices and Applications," *IEEE Trans. Electron Devices*, vol. 64, pp. 779–795, mar 2017.

[73] H. Amano, N. Sawaki, I. Akasaki, and Y. Toyoda, "Metalorganic vapor phase epitaxial growth of a high quality GaN film using an AlN buffer layer," *Appl. Phys. Lett.*, vol. 48, pp. 353–355, feb 1986.

[74] W. E. Hoke, A. Torabi, J. J. Mosca, R. B. Hallock, and T. D. Kennedy, "Rapid silicon outdiffusion from SiC substrates during molecular-beam epitaxial growth of AlGaN/GaN/AlN transistor structures," *J. Appl. Phys.*, vol. 98, p. 084510, oct 2005.

[75] J. T. Chen, J. W. Pomeroy, N. Rorsman, C. Xia, C. Virojanadara, U. Forsberg, M. Kuball, and E. Janzén, "Low thermal resistance of a GaN-on-SiC transistor structure with improved structural properties at the interface," *J. Cryst. Growth*, vol. 428, pp. 54–58, 2015.

[76] D. I. Babic, "Optimal AlGaN/GaN HEMT Buffer Layer Thickness in the Presence of an Embedded Thermal Boundary," *IEEE Trans. Electron Devices*, vol. 61, pp. 1047–1053, apr 2014.

[77] M. Uren, K. Nash, R. Balmer, T. Martin, E. Morvan, N. Caillas, S. Delage, D. Ducatteau, B. Grimbert, and J. De Jaeger, "Punch-through in short-channel AlGaN/GaN HFETs," *IEEE Trans. Electron Devices*, vol. 53, pp. 395–398, feb 2006.

[78] D. C. Tripathi, M. J. Uren, and D. Ritter, "Insight into Buffer Trap-Induced Current Saturation and Current Collapse in GaN RF Heterojunction Field-Effect Transistors," *IEEE Trans. Electron Devices*, vol. 67, pp. 5460–5465, dec 2020.

[79] D. S. Arteev, A. V. Sakharov, W. V. Lundin, E. E. Zavarin, D. A. Zakheim, A. F. Tsatsulnikov, M. I. Gindina, and P. N. Brunkov, "Influence of doping profile of GaN:Fe buffer layer on the properties of AlGaN/AlN/GaN heterostructures for high-electron mobility transistors," *J. Phys. Conf. Ser.*, vol. 1697, p. 012206, dec 2020.

[80] T. Palacios, A. Chakraborty, S. Heikman, S. Keller, S. DenBaars, and U. Mishra, "AlGaN/GaN high electron mobility transistors with InGaN back-barriers," *IEEE Electron Device Lett.*, vol. 27, pp. 13–15, jan 2006.

[81] D. S. Lee, X. Gao, S. Guo, and T. Palacios, "InAlN/GaN HEMTs With AlGaN Back Barriers," *IEEE Electron Device Lett.*, vol. 32, pp. 617–619, may 2011.

[82] F. Meng, J. Zhang, H. Zhou, J. Ma, J. Xue, L. Dang, L. Zhang, M. Lu, S. Ai, X. Li, and Y. Hao, "Transport characteristics of AlGaN/GaN/AlGaN double heterostructures with high electron mobility," *J. Appl. Phys.*, vol. 112, p. 023707, jul 2012.

[83] J.-G. Kim, C. Cho, E. Kim, J. S. Hwang, K.-H. Park, and J.-H. Lee, "High Breakdown Voltage and Low-Current Dispersion in AlGaN/GaN HEMTs With High-Quality AlN Buffer Layer," *IEEE Trans. Electron Devices*, vol. 1, pp. 1–5, 2021.

[84] J. Bergsten, *Buffer Related Dispersive Effects in Microwave GaN HEMTs.* PhD thesis, Chalmers University of Technology, 2018.

[85] W. Zhang, J. Xue, L. Zhang, T. Zhang, Z. Lin, J. Zhang, and Y. Hao, "Trap state analysis in AlGaN/GaN/AlGaN double heterostructure high electron mobility transistors at high temperatures," *Appl. Phys. Lett.*, vol. 110, p. 252102, jun 2017.

[86] D. Y. Chen, A. Malmros, M. Thorsell, H. Hjelmgren, O. Kordina, J. T. Chen, and N. Rorsman, "Microwave Performance of 'Buffer-Free' GaN-on-SiC High Electron Mobility Transistors," *IEEE Electron Device Lett.*, vol. 41, no. 6, pp. 828–831, 2020.

[87] J. Jorudas, A. Šimukovič, M. Dub, M. Sakowicz, P. Prystawko, S. Indrišiūnas, V. Kovalevskij, S. Rumyantsev, W. Knap, and I. Kašalynas, "AlGaN/GaN on SiC Devices without a GaN Buffer Layer: Electrical and Noise Characteristics," *Micromachines*, vol. 11, p. 1131, dec 2020.

[88] B. Hult, M. Thorsell, J. T. Chen, and N. Rorsman, "High Voltage and Low Leakage GaN-on-SiC MISHEMTs on a 'Buffer-Free' Heterostructure," *IEEE Electron Device Lett.*, vol. 43, no. 5, pp. 781–784, 2022.

[89] L. Shen, S. Heikman, B. Moran, R. Coffie, N.-Q. Zhang, D. Buttari, I. Smorchkova, S. Keller, S. DenBaars, and U. Mishra, "AlGaN/AlN/GaN high-power microwave HEMT," *IEEE Electron Device Lett.*, vol. 22, pp. 457–459, oct 2001.

[90] I. P. Smorchkova, L. Chen, T. Mates, L. Shen, S. Heikman, B. Moran, S. Keller, S. P. DenBaars, J. S. Speck, and U. K. Mishra, "AlN/GaN and (Al,Ga)N/AlN/GaN two-dimensional electron gas structures grown by plasma-assisted molecular-beam epitaxy," *J. Appl. Phys.*, vol. 90, pp. 5196–5201, nov 2001.

[91] D. S. Lee, X. Gao, S. Guo, D. Kopp, P. Fay, and T. Palacios, "300-GHz InAlN/GaN HEMTs With InGaN Back Barrier," *IEEE Electron Device Lett.*, vol. 32, pp. 1525–1527, nov 2011.

[92] A. Goswami, R. J. Trew, and G. L. Bilbro, "Modeling of the gate leakage current in AlGaN/GaN HFETs," *IEEE Trans. Electron Devices*, vol. 61, no. 4, pp. 1014–1021, 2014.

[93] A. Chini, F. Fantini, V. Di Lecce, M. Esposto, A. Stocco, N. Ronchi, F. Zanon, G. Meneghesso, and E. Zanoni, "Correlation between DC and rf degradation due to deep levels in AlGaN/GaN HEMTs," in *2009 IEEE Int. Electron Devices Meet.*, pp. 1–4, IEEE, dec 2009.

[94] S. A. Albahrani, L. Heuken, D. Schwantuschke, T. Gneiting, J. N. Burghartz, and S. Khandelwal, "Consistent Surface-Potential-Based Modeling of Drain and Gate Currents in AlGaN/GaN HEMTs," *IEEE Trans. Electron Devices*, vol. 67, pp. 455–462, feb 2020.

[95] E. T. Yu, X. Z. Dang, L. S. Yu, D. Qiao, P. M. Asbeck, S. S. Lau, G. J. Sullivan, K. S. Boutros, and J. M. Redwing, "Schottky barrier engineering in III-V nitrides via the piezoelectric effect," *Appl. Phys. Lett.*, vol. 73, pp. 1880–1882, sep 1998.

[96] G. Meneghesso, F. Rampazzo, P. Kordoš, G. Verzellesi, and E. Zanoni, "Current collapse and high-electric-field reliability of unpassivated GaN/AlGaN/GaN HEMTs," *IEEE Trans. Electron Devices*, vol. 53, no. 12, pp. 2932–2940, 2006.

[97] G. Koley, V. Tilak, L. F. Eastman, and M. G. Spencer, "Slow transients observed in AlGaN/GaN HFETs: Effects of SiNx passivation and UV illumination," *IEEE Trans. Electron Devices*, vol. 50, no. 4, pp. 886–893, 2003.

[98] Hyungtak Kim, R. Thompson, V. Tilak, T. Prunty, J. Shealy, and L. Eastman, "Effects of SiN passivation and high-electric field on AlGaN-GaN HFET degradation," *IEEE Electron Device Lett.*, vol. 24, pp. 421–423, jul 2003.

[99] S. Yang, Z. Tang, M. Hua, Z. Zhang, J. Wei, Y. Lu, and K. J. Chen, "Investigation of SiNx and AlN passivation for AlGaN/GaN high-electron-mobility transistors: Role of interface traps and polarization charges," *IEEE J. Electron Devices Soc.*, vol. 8, no. March, pp. 358–364, 2020.

[100] B. Green, K. Chu, E. Chumbes, J. Smart, J. Shealy, and L. Eastman, "The effect of surface passivation on the microwave characteristics of undoped AlGaN/GaN HEMTs," *IEEE Electron Device Lett.*, vol. 21, pp. 268–270, jun 2000.

[101] B. Romanczyk, X. Zheng, M. Guidry, H. Li, N. Hatui, C. Wurm, A. Krishna, E. Ahmadi, S. Keller, and U. K. Mishra, "W-Band Power Performance of SiN-Passivated N-Polar GaN Deep Recess HEMTs," *IEEE Electron Device Lett.*, vol. 41, pp. 349–352, mar 2020.

[102] A. Brannick, N. Zakhleniuk, B. Ridley, J. Shealy, W. Schaff, and L. Eastman, "Influence of Field Plate on the Transient Operation of the AlGaN/GaN HEMT," *IEEE Electron Device Lett.*, vol. 30, pp. 436–438, may 2009.

[103] S. Khandelwal, Y. S. Chauhan, T. A. Fjeldly, S. Ghosh, A. Pampori, D. Mahajan, R. Dangi, and S. A. Ahsan, "ASM GaN: Industry Standard Model for GaN RF and Power Devices - Part 1: DC, CV, and RF Model," *IEEE Trans. Electron Devices*, vol. 66, pp. 80–86, jan 2019.

[104] P. V. Raja, M. Bouslama, S. Sarkar, K. R. Pandurang, J.-C. Nallatamby, N. DasGupta, and A. DasGupta, "Deep-Level Traps in AlGaN/GaN- and AlInN/GaN-Based HEMTs With Different Buffer Doping Technologies," *IEEE Trans. Electron Devices*, vol. 67, pp. 2304–2310, jun 2020.

[105] Synopsys and Inc, *Sentaurus Device User Guide.* No. December, 2019.

[106] W. Shockley and W. T. Read, "Statistics of the Recombinations of Holes and Electrons," *Phys. Rev.*, vol. 87, pp. 835–842, sep 1952.

[107] Chih-Tang Sah, "The equivalent circuit model in solid-state electronics-Part I: The single energy level defect centers," *Proc. IEEE*, vol. 55, no. 5, pp. 654–671, 1967.

[108] Chih-Tang Sah, "The equivalent circuit model in solid-state electronics-Part II: The multiple energy level impurity centers," *Proc. IEEE*, vol. 55, no. 5, pp. 672–684, 1967.

[109] D. K. Schroder, *Semiconductor Material and Device Characterization.* Hoboken, NJ, USA: John Wiley and Sons, Inc., oct 2005.

[110] P. Würfel and U. Würfel, *Physics of solar cells.* 3 ed., 2016.

[111] W. Shockley, "Electrons and Holes in Semiconductors: With Applications to Transistor Electronics," 1950.

[112] S. Sze and K. K. Ng, *Physics of Semiconductor Devices.* Hoboken, NJ, USA: John Wiley and Sons, Inc., oct 2006.

[113] D. Wickramaratne, C. E. Dreyer, B. Monserrat, J.-X. Shen, J. L. Lyons, A. Alkauskas, and C. G. Van de Walle, "Defect identification based on first-principles calculations for deep level transient spectroscopy," *Appl. Phys. Lett.*, vol. 113, p. 192106, nov 2018.

[114] A. Alkauskas, M. D. McCluskey, and C. G. Van de Walle, "Tutorial: Defects in semiconductors-Combining experiment and theory," *J. Appl. Phys.*, vol. 119, p. 181101, may 2016.

[115] M. Cioni, N. Zagni, L. Selmi, G. Meneghesso, M. Meneghini, E. Zanoni, and A. Chini, "Electric Field and Self-Heating Effects on the Emission Time of Iron Traps in GaN HEMTs," *IEEE Trans. Electron Devices*, pp. 1–8, 2021.

[116] O. Jardel, F. De Groote, T. Reveyrand, J. C. Jacquet, C. Charbonniaud, J. P. Teyssier, D. Floriot, and R. Quéré, "An electrothermal model for AlGaN/GaN power HEMTs including trapping effects to improve large-signal simulation results on high VSWR," *IEEE Trans. Microw. Theory Tech.*, vol. 55, no. 12, pp. 2660–2669, 2007.

[117] J. Bergsten, M. Thorsell, D. Adolph, J.-T. Chen, O. Kordina, E. O. Sveinbjornsson, and N. Rorsman, "Electron Trapping in Extended Defects in Microwave AlGaN/GaN HEMTs With Carbon-Doped Buffers," *IEEE Trans. Electron Devices*, vol. 65, pp. 2446–2453, jun 2018.

[118] N. Modolo, C. De Santi, A. Minetto, L. Sayadi, G. Prechtl, G. Meneghesso, E. Zanoni, and M. Meneghini, “Trap-state mapping to model GaN transistors dynamic performance,” *Sci. Rep.*, vol. 12, p. 1755, dec 2022.

[119] N. K. Subramani, J. Couvidat, A. A. Hajjar, J. C. Nallatamby, and R. Quéré, “Low-Frequency Drain Noise Characterization and TCAD Physical Simulations of GaN HEMTs: Identification and Analysis of Physical Location of Traps,” *IEEE Electron Device Lett.*, vol. 39, no. 1, pp. 107–110, 2018.

[120] F. Hooge, “1/f noise sources,” *IEEE Trans. Electron Devices*, vol. 41, no. 11, pp. 1926–1935, 1994.

[121] J. Couvidat, N. K. Subramani, V. Gillet, S. Laurent, C. Charbonniaud, J. C. Nallatamby, M. Prigent, N. Deltimple, and R. Quéré, “Investigation of Fast and Slow Charge Trapping Mechanisms of GaN/A1GaN HEMTs through Pulsed I-V Measurements and the Associated New Trap Model,” *IEEE MTT-S Int. Microw. Symp. Dig.*, vol. 2018-June, pp. 720–723, 2018.

[122] K. Kunihiro and Y. Ohno, “A large-signal equivalent circuit model for substrate-induced drain-lag phenomena in HJFET’s,” *IEEE Trans. Electron Devices*, vol. 43, no. 9, pp. 1336–1342, 1996.

[123] J. G. Rathmell and A. E. Parker, “Circuit implementation of a theoretical model of trap centres in GaAs and GaN devices,” *Microelectron. Des. Technol. Packag. III*, vol. 6798, p. 67980R, 2007.

[124] A. Santarelli, R. Cignani, G. P. Gibiino, D. Niessen, P. A. Traverso, C. Florian, D. M. Schreurs, and F. Filicori, “A double-pulse technique for the dynamic I/V characterization of GaN FETs,” *IEEE Microw. Wirel. Components Lett.*, vol. 24, no. 2, pp. 132–134, 2014.

[125] G. P. Gibiino, A. Santarelli, and P. A. Traverso, “Pulsed techniques for the characterization of low-frequency dispersive effects in RF power FETs using a flexible measurement set-up,” *Measurement*, vol. 176, p. 109240, may 2021.

[126] A. R. Arehart, A. Sasikumar, G. D. Via, B. Winningham, B. Poling, E. Heller, and S. A. Ringel, “Spatially-discriminating trap characterization methods for HEMTs and their application to RF-stressed AlGaN/GaN HEMTs,” in *2010 Int. Electron Devices Meet.*, no. 4, pp. 20.1.1–20.1.4, IEEE, dec 2010.

[127] L. C. Nunes, J. M. Gomes, P. M. Cabral, and J. C. Pedro, “A new nonlinear model extraction methodology for GaN HEMTs subject to trapping effects,” in *2015 IEEE MTT-S Int. Microw. Symp. IMS 2015*, pp. 1–4, 2015.

[128] L. C. Nunes, J. L. Gomes, P. M. Cabral, and J. C. Pedro, “A Simple Method to Extract Trapping Time Constants of GaN HEMTs,” *IEEE MTT-S Int. Microw. Symp. Dig.*, vol. 2018-June, pp. 716–719, 2018.

[129] F. Fornetti, M. Beach, and J. G. Rathmell, “The application of GaN HEMTs to pulsed PAs and radar transmitters,” in *Eur. Microw. Week 2012 ”sp. Microwaves”, EuMW 2012, Conf. Proc. - 7th Eur. Microw. Integr. Circuits Conf. EuMIC 2012*, pp. 405–408, 2012.

[130] C. F. Gonçalves, L. C. Nunes, P. M. Cabral, and J. C. Pedro, "Pulsed I / V and S - parameters measurement system for isodynamic characterization of power GaN HEMT transistors," *Int. J. RF Microw. Comput. Eng.*, vol. 28, p. e21515, oct 2018.

[131] M. Bouslama, V. Gillet, C. Chang, J.-C. Nallatamby, R. Sommet, M. Prigent, R. Quere, and B. Lambert, "Dynamic Performance and Characterization of Traps Using Different Measurements Techniques for the New AlGaN/GaN HEMT of 0.15-μ m Ultrashort Gate Length," *IEEE Trans. Microw. Theory Tech.*, vol. 67, pp. 2475–2482, jul 2019.

[132] F. Microwaves, "AU4850 Pulsed IV / RF Characterization System."

[133] Maury Microwave Corporation, "AM 3200 PIV System," tech. rep., 2018.

[134] P. M. Cabral, J. C. Pedro, and N. B. Carvalho, "Nonlinear device model of microwave power GaN HEMTs for high power-amplifier design," *IEEE Trans. Microw. Theory Tech.*, vol. 52, no. 11, pp. 2585–2592, 2004.

[135] J. L. Lyons, D. Wickramaratne, and C. G. Van de Walle, "A first-principles understanding of point defects and impurities in GaN," *J. Appl. Phys.*, vol. 129, p. 111101, mar 2021.

[136] R. Trew, "SiC and GaN transistors - is there one winner for microwave power applications?," *Proc. IEEE*, vol. 90, pp. 1032–1047, jun 2002.

[137] W. Sun, J. L. Jimenez, and A. R. Arehart, "Impact of Traps on the Adjacent Channel Power Ratios of GaN HEMTs," *IEEE Electron Device Lett.*, vol. 41, no. 6, pp. 816–819, 2020.

[138] J. C. Pedro, L. C. Nunes, and P. M. Cabral, "Soft compression and the origins of nonlinear behavior of GaN HEMTs," *Eur. Microw. Week 2014 Connect. Futur. EuMW 2014 - Conf. Proceedings; EuMC 2014 44th Eur. Microw. Conf.*, pp. 1297–1300, 2014.

[139] M. Lee and L. Forbes, "A self-backgating GaAs MESFET model for low-frequency anomalies," *IEEE Trans. Electron Devices*, vol. 37, no. 10, pp. 2148–2157, 1990.

[140] P. Aaen, J. A. Plá, and J. Wood, *Modeling and Characterization of RF and Microwave Power FETs.* Cambridge: Cambridge University Press, 2007.

[141] T. Cappello, C. Florian, A. Santarelli, and Z. Popovic, "Linearization of a 500-W L-band GaN Doherty Power Amplifier by Dual-Pulse Trap Characterization," in *2019 IEEE MTT-S Int. Microw. Symp.*, vol. 2019-June, pp. 905–908, IEEE, jun 2019.

[142] Y. Guo, C. Yu, and A. Zhu, "Power Adaptive Digital Predistortion for Wideband RF Power Amplifiers With Dynamic Power Transmission," *IEEE Trans. Microw. Theory Tech.*, vol. 63, pp. 3595–3607, nov 2015.

[143] M. Meneghini, P. Vanmeerbeek, R. Silvestri, S. Dalcanale, A. Banerjee, D. Bisi, E. Zanoni, G. Meneghesso, and P. Moens, "Temperature-Dependent Dynamic Ron in GaN-Based MIS-HEMTs: Role of Surface Traps and Buffer Leakage," *IEEE Trans. Electron Devices*, vol. 62, pp. 782–787, mar 2015.

[144] S. J. Duffy, B. Benbakhti, W. Zhang, K. Kalna, K. Ahmeda, M. Boucherta, N. E. Bourzgui, H. Maher, and A. Soltani, “A Source and Drain Transient Currents Technique for Trap Characterisation in AIGaN/GaN HEMTs,” in *2018 13th Eur. Microw. Integr. Circuits Conf.*, pp. 214–217, IEEE, sep 2018.

[145] S. J. Duffy, B. Benbakhti, W. Zhang, K. Ahmeda, K. Kalna, M. Boucherta, M. Mattalah, H. O. Chahdi, N. E. Bourzgui, and A. Soltani, “A parametric technique for trap characterization in AlGaN/GaN HEMTs,” *IEEE Trans. Electron Devices*, vol. 67, no. 5, pp. 1924–1930, 2020.